



THE UNIVERSITY OF QUEENSLAND
A U S T R A L I A

Remote sensing of land use changes and impacts on river turbidity in a small-scale mining region

Celso Isidro

B.Sc., University of the Philippines

A thesis submitted for the degree of Master of Philosophy at

The University of Queensland in 2017

Sustainable Minerals Institute

Abstract

The effective management of artisanal and small-scale mining (ASM) on regional and national scales must be based on good understanding of land and water footprints from various land use and land covers. The diffuse, dynamic and often remote nature of ASM means that traditional ground-based surveys are likely to be impractical except for local scale studies. Remote sensing offers a low-cost option for surveying land use changes and water turbidity, and quantifying the impact of ASM on water quality. However, there are questions about the reliability of remote sensing products for these tasks, and there is a need for recommendations about suitable products, data resolutions and analysis techniques. A case study of the Addalam river basin in the Cagayan region, situated in Luzon forming a part of the Philippine archipelago, was used to address these research questions. The value of alternative satellite products was tested using independent sources of land use, suspended sediments and turbidity data from project partners OceanaGold (Philippines), International RiverFoundation, and local government agencies.

The unpredictable climate in wet tropical regions, and the spatial limitations of current satellite imageries are the challenges for remote detection of ASM. Pleiades and SPOT imageries were identified as potentially suitable and were tested. Historical spatial data on location and type of ASM mines were collected from the field, and were utilised as training data for classification through the OB-SVM classifier. The analysis resulted in overall accuracy between 87% and 89% for three different images; Pleiades-1A HiRI sensor for the 2013 and 2014 images, and SPOT-6 NAOMI sensor for the 2016 image. The main land use features, particularly the Didipio large-scale mine, were well identified by the OB-SVM classifier; however, the presence of small-scale mines was slightly under identified. The lack of consistency in their shape, and their small scale compared to the pixel sizes, meant they could not be reliably distinguished from other land clearance types. The biased-adjusted surface areas were acquired to determine the best possible estimates of the area variation in small-scale mines throughout the year. The image analysis indicated an increase in small-scale mining area from 91,000 m² or 0.2% in March 2013 to 121,000 m² or 0.3% in May 2014, and then a decrease to 39,000 m² or 0.1% in January 2016.

Various land use features in a mining region have different sediment yields, which have significant influence on the concentration of suspended solids in rivers. In-situ sampling can only describe the integrated impact of the upstream land uses. A model of total suspended solids (TSS) through the acquired surface reflectance from calibrated satellite images can be used to assess the fate and transport of sediments throughout the catchment of Didipio. The surface reflectance data from the

satellites were used to develop a regression model of the TSS concentration. A linear model was derived between the surface reflectance data from Pleiades-1A and the corresponding ground-based measurements of TSS concentration. The regression using the red channel reflectance gave R^2 values of 99% and 58%, respectively, for the two separate images of Pleiades-1A in 2013 and 2014. However, the regression model of the integrated dataset of surface reflectance and TSS from both images resulted to R^2 value of 20%, and an RMS error of 937 mgL^{-1} . The generated model represents sediments from different sources. It was noted that the increase in small-scale mines from 2013 to 2014 resulted to additional stripping of topsoil, which has lower surface reflectance when compared against fine particles with similar magnitude of TSS. The model was used to generate a map of continuous concentrations of TSS from the upstream to downstream of the catchment. However, the lack of images and simultaneous ground-based measurements of TSS concentrations that are higher than $3,580 \text{ mgL}^{-1}$ means that the model cannot be confidently applied over the full relevant range of TSS.

Overall, it is concluded that remote sensing shows promise in capturing the land and water quality footprints of ASM. However, the lack of cloud-free images in the case study and wet tropical regions in general is a significant problem in terms of capturing a sufficient number, and range of samples to develop the models. The integration of more images and simultaneous TSS samples, including higher concentrations, is recommended. On the other hand, further works on classification of land use features can be performed over the regions with less obstruction from cloud coverage (e.g. sites at lower ground elevation) and investigate the applicability of recently available moderate resolution satellite imageries (10 m or better) such as Sentinel-2 that can maintain the continuity of satellite images at no cost.

Declaration by author

This thesis is composed of my original work, and contains no material previously published or written by another person except where due reference has been made in the text. I have clearly stated the contribution by others to jointly-authored works that I have included in my thesis.

I have clearly stated the contribution of others to my thesis as a whole, including statistical assistance, survey design, data analysis, significant technical procedures, professional editorial advice, and any other original research work used or reported in my thesis. The content of my thesis is the result of work I have carried out since the commencement of my research higher degree candidature and does not include a substantial part of work that has been submitted to qualify for the award of any other degree or diploma in any university or other tertiary institution. I have clearly stated which parts of my thesis, if any, have been submitted to qualify for another award.

I acknowledge that an electronic copy of my thesis must be lodged with the University Library and, subject to the policy and procedures of The University of Queensland, the thesis be made available for research and study in accordance with the Copyright Act 1968 unless a period of embargo has been approved by the Dean of the Graduate School.

I acknowledge that copyright of all material contained in my thesis resides with the copyright holder(s) of that material. Where appropriate I have obtained copyright permission from the copyright holder to reproduce material in this thesis.

Publications during candidature

No publications included

Publications included in this thesis

Publication citation – incorporated as Chapter 4.

Contributor	Statement of contribution	
Celso Isidro	Designed the methodology workflow Contribution to remote sensing and statistical analyses Writing of the paper	70%
Prof. Neil McIntyre	Advising on analysis Reviewing drafts of the paper	10%
Dr. Alexander Lechner	Advising on analysis Reviewing drafts of the paper	10%
Mr. Ian Callow	Contribution to data access agreement	10%

Contributions by others to the thesis

No contributions by others.

Statement of parts of the thesis submitted to qualify for the award of another degree

None

Acknowledgments

I would like to acknowledge Prof. Neil McIntyre who supported my aspiration to study through the research programs in the Sustainable Minerals Institute (SMI). Through the program, I was exposed to the fields of remote sensing, geographic information systems and hydrology, which are of practical use in regional planning as well as in mine engineering. It was a great opportunity to have these fields added to my expertise, and to be able to test them in a case study in my country, the Philippines. Also, I would like to recognise the assistance of Mr. Ian Callow who managed my research agreements, and contributed to analyses of my field data; Dr. Alexander Lechner, who despite moving to other university, still made himself available through providing his technical capability towards the methodology of the research.

Moreover, this opportunity to study in an international university became achievable because of the Australia Awards Scholarship, which provided all forms of support to enable completion of this thesis manuscript in its best form. I also would like to thank OceanaGold Philippines Incorporated and International RiverFoundation (IRF) for being the hosts of the case study in Didipio. Without their assistance, it would not have been possible to collect water quality data, and conduct land use ground surveys in the region. Also, I would like to recognise the supplementary support (e.g. maps and spatial data of the Didipio catchment) provided by the Mines and Geosciences Bureau of Region 2, as well as the Philippine National Mapping and Resource Information Authority (NAMRIA); the DigitalGlobe Foundation for the provision of a 2010 WorldView-2 satellite image of the Didipio catchment, which became part of analysis and discussion of one of the thesis chapters.

I would like to thank my loving wife, Donamae Isidro, for her patience and support during my academic years at the University of Queensland; my parents, Calixto and Ofelia who did not stop communicating while I was away from my home country.

And finally, to God who gave me the guidance, and spiritual support to continue in pursuing this task as part of my purpose, to Him be the glory.

Keywords

Artisanal and small-scale mining, geographic-object-based image analysis, total suspended solids, turbidity, empirical modelling, wet tropical region, Philippines, Didipio catchment, hypsometric curve, support vector machine

Australian and New Zealand Standard Research Classifications (ANZSRC)

ANZSRC code: 091405, Mining Engineering, 10%

ANZSRC code: 040608, Surfacewater Hydrology, 30%

ANZSRC code: 090905, Photogrammetry and Remote Sensing, 60%

Fields of Research (FoR) Classification

FoR code: 0914, Resources Engineering and Extractive Metallurgy, 10%

FoR code: 0406, Physical Geography and Environmental Geoscience, 30%

FoR code: 0909, Geomatics Engineering, 60%

Table of Contents

Chapter 1 Introduction and Literature Review.....	15
1.1 Introduction	15
1.1.1 Artisanal and small-scale mining in the Philippines.....	15
1.2 Project Research's Questions, Hypothesis, Objectives and Output.....	17
1.2.1 Research Questions.....	17
1.2.2 Research Hypothesis.....	17
1.2.3 Research Objectives	18
1.2.4 Research Output	18
1.3 Literature Review	18
1.3.1 Overview of remote sensing and land use assessment	18
1.3.2 Resolution of sensors.....	23
1.3.3 Types of sensors	25
1.3.4 Different approaches to image analysis, and their corresponding application in delineating small-scale mining regions	27
1.3.5 The application of remote sensing to modelling water turbidity and total suspended solids ..	29
1.4 Knowledge gaps in previous studies	33
Chapter 2 Description of the Case Study Area.....	35
2.1 Regional location of the case study area.....	35
2.2 Access and Transportation.....	37
2.3 Geology	37
2.3.1 Regional Geology	37
2.3.2 Local Geology	37
2.4 Land use and land cover	38
2.5 Topography.....	38
2.6 Water catchment	39
2.7 Climate	40
2.7.1 National climate.....	40
2.7.2 Didipio local climate	41
2.8 Summary.....	41
Chapter 3 Characterisation of the catchment and surface water quality	43
3.1 Research approach.....	44
3.1.1 Acquisition of surface water quality data	44
3.1.2 Method of surface water quality sampling	46
3.1.3 Laboratory and in-situ analyses of surface water quality data.....	46
3.1.4 Measurement for flow rate	47
3.1.5 Rainfall and weather data	47
3.1.6 Application of a Digital Elevation Model (DEM)	48

3.1.7	Application of an optical image product	48
3.2	Results and discussion.....	49
3.2.1	Physical attributes of the rivers	49
3.2.2	Geometric characteristics of the sub-drainage basins.....	53
3.2.3	Temporal variations in TSS.....	59
3.3	Summary.....	62
Chapter 4	Applicability of satellite imagery to identify small-scale mining footprints in a wet tropical region.....	63
4.1	Research approach.....	65
4.1.1	Collection of ground truth data on the locations of small-scale mines.....	65
4.1.2	Selection of satellite images	71
4.1.3	Pre-processing stages of satellite image data.....	72
4.1.4	Classification method	73
4.1.5	Accuracy assessment	77
4.2	Results and discussion.....	78
4.2.1	Comparison of spectral signatures across land use classes.....	78
4.2.2	Accuracy assessment of classification for Pleiades-1A and SPOT-6 images.....	81
4.2.3	Coverage and spatial distribution of areas classed as SSM relative to other land use classes.	83
4.3	Summary.....	87
Chapter 5	Quantifying suspended solids in small rivers using satellite data	88
5.1	Research approach.....	90
5.1.1	Selection of monitoring stations	90
5.1.2	Selection of satellite products.....	91
5.1.3	Water quality data against the test pixels	92
5.1.4	Calibration of images.....	93
5.1.5	Variation in turbidity through time	93
5.1.6	Univariate analysis of surface reflectance and total suspended solids	94
5.2	Results and discussion.....	95
5.2.1	Collective effect of rainfall and ASM to increasing concentration of suspended sediments ..	95
5.2.2	Relationship between TSS and surface reflectance	98
5.3	Summary.....	108
Chapter 6	Conclusions and recommendations	110
6.1	Conclusions	110
6.1.1	Environmental importance of Didipio catchment.....	110
6.1.2	The applicability of remote sensing to identifying artisanal and small-scale mining land footprints in the context of wet tropical regions	110
6.1.3	The applicability of remote sensing to identifying variations in water quality in the context of wet tropical regions	111
6.2	Recommendations	111

List of References.....	113
Appendix A - Regional geology of Northern Luzon.....	125
Appendix B - Slope map of selected sub-drainage basins of Didipio catchment.....	126
Appendix C - Channel slopes	127
Appendix D - Photographs of artisanal and small-scale mining practices in Didipio catchment.....	129
Appendix E - Parameters for radiometric calibration.....	131
Appendix F- Parameters and attributes for segmentation.....	132
Appendix G- NDVI maps.....	133

List of Figures

Figure 1-1: Spectral regions of an electromagnetic radiation.....	21
Figure 1-2: Spectral signatures of land cover and other land features.....	22
Figure 1-3: Types of sensors based on source of illumination and use of spectral region	26
Figure 1-4: Sources of light for each spectral region	26
Figure 2-1: The Addalam River Sub-Basin on Luzon Island.....	36
Figure 2-2: Topographic map of Didipio case study area	39
Figure 2-3: The section of Didipio catchment with available water quality data.....	40
Figure 3-1: Location of river monitoring stations.....	45
Figure 3-2: Measurement of flow rates at each monitoring station located downstream of primary river tributaries.....	47
Figure 3-3: Calculation of the hypsometric curve using a Digital Elevation Model (DEM)	48
Figure 3-4: Four-year rainfall data of the Didipio catchment area with recorded water flow rates in 2013 and 2014.....	50
Figure 3-5: Box and whiskers plots of TSS.....	51
Figure 3-6: Graphs of TSS versus turbidity in each monitoring station.....	52
Figure 3-7: Linear relationship between TSS and turbidity in the Didipio catchment.....	53
Figure 3-8: Delineation of sub-drainage basins in the catchment area.....	55
Figure 3-9. Formation of a channel bar in Camgat-Surong River	56
Figure 3-10: Graph of hypsometric curves for each river	57
Figure 3-11: Existence of small-scale mines in 2010, prior the construction of open-pit mine	58
Figure 3-12: Plot of surface reflectance for the impacted river segments by activities of small-scale mines (A-D)	59
Figure 3-13: Changes in the upper Didipio River over time	60
Figure 3-14: Temporal variation of total suspended solids from 2013 to 2016	61
Figure 4-1: Major features of the Didipio catchment area in the Philippines.....	67
Figure 4-2: Active small-scale mining sites derived from field data from 2012 to 2015 categorized by mining method.	68
Figure 4-3: Different forms of mining in Didipio catchment. (a) Sediment pit; (b) Panning area; (c) Small-scale mines on hard rocks; (d) Large-scale open-pit mine.	68
Figure 4-4: Locations and types of active small-scale mine sites based on ground surveys, superimposed on remote-sensed images.....	70
Figure 4-5: Flowchart of image pre-processing and image analysis (classification and post-classification)..	76
Figure 4-6: Plots of spectral signatures of land use subclasses using mean values of reflectance across all training data.....	80
Figure 4-7: Output thematic maps and the corresponding land use class coverage distributions	86
Figure 5-1: Locations of selected monitoring stations.....	91
Figure 5-2: Locations of six test pixels for each monitoring station	93
Figure 5-3: Assigned stations for the analysis of river turbidity variation	94
Figure 5-4: Plot of hourly monitoring of river turbidity during the early phase of the wet season in the Didipio case study	97
Figure 5-5: Plot of surface reflectance from the 6 adjacent pixels of each monitoring station	99
Figure 5-6: Spectral signatures of water with suspended solids (a) 2013; (b) 2014.....	102
Figure 5-7: Spectral signatures corresponding to different measured TSS concentrations	104
Figure 5-8: Graphs of total suspended solids against band reflectance for 2013 Pleiades-1A images:	105
Figure 5-9: Calibrated thematic maps of surface reflectance with corresponding measurement level of TSS	107

List of Tables

Table 1-1: Philippine gold production from 2011 to 2012	16
Table 1-2: List of spectral regions that are commonly used in remote sensing.....	20
Table 1-3: Spectral channels of selected spectral regions	21
Table 1-4: List of model equations.....	33
Table 2-1: Districts that form the Addalam River Basin.....	36
Table 2-2: Philippine climate based on Coronas classification	41
Table 3-1: Database of surface water quality parameters from 2013 to 2016.....	45
Table 3-2: Statistics of TSS of the 6 principal rivers (2013-2016).....	51
Table 3-3: Relationship of TSS and turbidity for each river	53
Table 3-4: Descriptive statistics of the catchment slopes	54
Table 3-5: Descriptive statistics of the channel slopes	55
Table 3-6: Surface area of each sub-drainage basin	58
Table 4-1: Technical specifications of the three scenes (2013, 2014, 2016) and sensor characteristics.....	71
Table 4-2. Ground survey dates that coincided with the selected satellite images.....	74
Table 4-3: Descriptions of the land use classes and size of training data in each image.....	75
Table 4-4: Generated Confusion Matrix for each image data a) 2013 Pleiades-1A b) 2014 Pleiades-1A c) 2016 SPOT-6.....	82
Table 4-5: Classified areas and Bias-adjusted areas of each land use class	84
Table 5-1: Physical attributes and locations of the monitoring stations.....	90
Table 5-2: Technical specifications of selected satellite images	92
Table 5-3: Surface reflectance values for each set of six test pixels	100
Table 5-4: Mean surface reflectance for each corresponding value of total suspended solids/ Turbidity: 30 March 2013 Pleiades-1A image, 5 May 2014 Pleiades-1A image	101
Table 5-5: Linear equations generated for TSS and surface reflectance relationship in each band	103

List of Abbreviations

ASM	Artisanal and Small-scale Mining
DENR	Department of Environment and Natural Resources
AMD	Acid Mine Drainage
GEOBIA	Geographic-Object-based Image Analysis
GIS	Geographic Information System
NTU	Nephelometric turbidity Units
DAO-34	DENR Administrative Order No. 34
MGB	Mines and Geosciences Bureau
FTAA	Financial and Technical Assistance Agreement
PDMF	Partial Declaration of Mine Feasibility
TSS	Total Suspended Solids
DN	Digital Number
CRB	Cagayan River Basin
CAR	Cordillera Administration Region
ARB	Addalam River Basin
OB-SVM	Object-based Support Vector Machine
VI	Vegetation index
NDVI	Normalised Difference Vegetation Index
HI	Hypsometric Integral

Chapter 1 Introduction and Literature Review

1.1 Introduction

1.1.1 Artisanal and small-scale mining in the Philippines

The Philippines is an example of a nation where artisanal and small-scale mining (ASM) is a fast-growing form of land use. The country officially regulates ASM activities through the Republic Act No. 7076, Presidential Decree No. 1899 and Executive Order No. 79. In general, these laws outline the responsibilities between the Department of Environment and Natural Resources (DENR) and the small-scale miners/ processors, in reference to sustainable operations. In addition, these laws only authorise the development of small-scale mines within a declared ‘Minahang Bayan’ or ‘People’s Small-scale Mining Area’ by the DENR at an allowable annual production of 50,000 metric tonnes for each mineral claim. However, in spite of these regulations, the poverty in local communities can result in substandard and illegal small-scale mining operations, particularly in remote locations with no established access. In a 2001 report (Bugnosen, 2001), 75% of Philippine ASMs were identified as operating at subsistence level, with 15% being in the form of small individual or family businesses. Often, a large population associated with an ASM do not have the capacity to sustain appropriate capital and operating costs. In fact, the homes in such communities are commonly found to be integrated with their mining claims, to help reduce the cost of ore transportation, and additional land acquisition (for housing development).

The ASM Industry supports between 200,000 and 300,000 people in the Philippines (Human Rights Watch, 2015). Thirty-five out of the 81 provinces in the country are reported to contain small-scale mines. Although the impressions of the industry are predominantly negative, the component of the industry that operates legally has been a principal contributor to Philippines’ annual gold production. In 1992, the industry was able to legally account for 25% (29,138 kg) of the Philippine’s national gold production (United Nations, 1996). However, it is believed that this was an underestimate, due to the undeclared production. In 2009 and 2010, the industry sold 40,847 and 37,047 kg of gold, respectively, to the Philippine Central Bank (Fong-Sam, 2012). In the first six months of 2011, ASM’s contribution to national gold production was estimated to be 65% (Table 1-1). In general, the industry is regarded as providing between 30% to 40% of the country’s gold (Oxford Business Group, 2016).

Table 1-1: Philippine gold production from 2011 to 2012

Category of Producer	January-June 2011	
	Quantity (kg)	Value (PhP)
Large-scale Mines		
Primary producers	4,995	39,071,863,372
Secondary producers	2,903	5,445,771,389
Small-scale Mines	14,907	28,958,174,923
TOTAL	22,805	73,475,809,684

Adapted from www.mgb.gov.ph/Files/Statistics

Worldwide, approximately 100 million people are involved in small-scale mining, of which 30 million are directly employed in the industry in seventy countries (Hirons, 2014; Sousa et al., 2011). Notwithstanding the economic benefits to local communities, it is the mined-out areas that are usually left unrehabilitated. This can leave the barren soil loose, unusable and with the potential to generate unwanted river sediments and/or acid mine drainage (AMD). Activities at small-scale mines in Kalimantan, Indonesia were reported to be the source of dissolved organic carbons in the rivers (Telmer & Stapper, 2007). In Tapajos Garimpeira, Brazil, identified dredging zones have produced highly turbid water (Telmer & Stapper, 2007). ASM has been a principal contributor to deforestation in Upper Mazaruni of Guyana (Mengisteab et al., 2015). In the Philippines, 140 metric tonnes of mercury (Hg) were reported to have been partially discharged into the Agusan River by 53 small-scale mines in Mindanao (Appleton et al., 1999). Globally, there is a lack of operational standards for the ASM Industry. The application of operational standards aims to deliver good land use planning in areas of ASM that lead towards the optimised development of land resources and a complete understanding of the industry's potential water effluents. Good land use planning minimises the rapid expansion of mining areas, and it serves as a natural means of control of potentially increasing environmental impacts (Telmer & Stapper, 2007).

Recently, a concentration of illegally operating small-scale miners commenced operating within the Copper-Gold Project of OceanaGold in Region 2, Cagayan Valley, in the Philippines. This unregulated mining activity is considered to contribute to the turbidity problem of the associated Didipio catchment and therefore needs to be investigated. There is a need to evaluate the ASM industry's contribution towards sediment loading, relative to the contribution from other forms of land use and natural sources.

Remote sensing offers a flexible approach to delineating various forms of land use, and for identifying their corresponding impacts to the environment. This flexibility provides an opportunity to consider, via research, the potential for using remote sensing methods as a means of assessing land use changes

and river turbidity resulting from ASM activities. Despite improvements in remote sensing data resolutions, this approach is not without challenges in wet tropical regions and remote areas. These challenges include, excessive levels of cloud cover and higher rate of light absorption by the atmosphere. Addressing the challenges requires assessing the acquisition frequency of various satellite images for case study areas and having access to software that can perform the most appropriate algorithms.

In this research, the Didipio catchment was used for a case study to investigate the applicability of remote sensing and GIS to assessing the extent and location of ASM, and help to explain the changes in the sediment regimes of rivers. It is anticipated that this will provide a better understanding of the dynamics of ASM, in terms of temporal and spatial contexts. This should be able to assist in the systematic planning of land use in mining zones, particularly in wet tropical regions.

1.2 Project Research's Questions, Hypothesis, Objectives and Output

For this study, different spatial data of the Didipio catchment provided by Philippine government agencies, project partners and from the database of moderate and very-high resolution imageries acquired within the available funding of the research were utilised. The general objective of the research is to assess these spatial data on their applicability to obtain information on ASM development as well as to generate a model of its impact to the Didipio catchment.

1.2.1 Research Questions

- Is remote sensing capable of providing a rapid, inexpensive, accurate and precise assessment of ASM's land and water quality footprint in wet tropical regions?

1.2.2 Research Hypothesis

- The application of Geographic-object-based image analysis (GEOBIA) to very-high resolution images can detect small-scale mines, and quantify the impact of various land uses in the catchment to the decline in vegetated areas and water quality.
- Remote sensing can provide a predictive model for suspended solids in inland waters.

1.2.3 Research Objectives

- To derive an approach to the selection of appropriate remote sensing products that can provide a precise, qualitative and quantitative description of land use features and water turbidity
- To determine and validate a statistical relationship between remote sensing images and field data related to land use and water turbidity
- To perform a spatial analysis to determine whether the remotely sensed data, supplemented by available field data, can identify the spatial factors affecting turbidity
- To determine whether remotely sensed data can provide a geographic information system (GIS) database on the recent history (1990s, 2000s) of ASM activities
- To discuss the potential extensibility of the methods used for the case study region to other regions

1.2.4 Research Output

- Rigorous evaluation of remote sensing as source of information in identification of various land use and land covers as well as a technique to forecast TSS in Didipio catchment
- Formulation of recommendations related to the use of remote sensing products for tracking the development and water quality impacts of ASM across the Philippines and other similar wet tropical regions

1.3 Literature Review

1.3.1 Overview of remote sensing and land use assessment

Remotely sensed images have been applied extensively in many local and regional studies of the environment since the 1960s. During that period, remote sensing was initially acknowledged as a reference to denote a field of study (Barrett & Curtis, 1999). Remote sensing is a branch of science that takes advantage of Earth features' differences in spectral signatures, in order to generate

geospatial data from a distance in the form of a digital image (Navalgund, 2001). Formerly, remote sensing was associated with analog black and white aerial photographs. Between the 1960s and 1970s, the shift of the remote sensing platform from aircraft to satellites provided the opportunity to archive digitised images, which are embodied with numerical values in the form of pixels. These numerical values are the carriers of information that is useful for scientific analysis (Singh, 2016). Through the years, series of images have been captured and compiled in databases of time-series image data. Some of these databases are readily available for use to test several Earth observations. Moreover, these images are compatible for integration with numerical models (Barrett & Curtis, 1999). Incorporating the remote sensed data within a geographic information system (GIS) allows efficient combination with supplementary spatial information (Cihlar, 2000), which can improve the identification of environmental problems and provide consistent modelling of land use/cover patterns (Rao, 2000; Rawat & Kumar, 2015).

In environmental management, frequent changes in land use is an anthropogenic factor of concern. If the changes are excessive and uncontrolled, they can possibly reduce the area of land available for production of food and forest timber (Wu, 2008). Likewise, increased deforestation can result in further degradation of the soil, increased surface run-off that carries sediments and transport of pollutants (Lubowski et al., 2006; The USGS Water Science School, 2016). A comprehensive understanding of land use changes as a product of the interaction between human factors and natural phenomena is essential (Butt et al., 2015). Consequently, sound planning and decision-making needs to be done in reference to land use changes in order to ensure that the Earth's natural resources are utilised for their intended purposes.

1.3.1.1 Components of the electromagnetic spectrum

The electromagnetic spectrum is a set of waves, which are differentiated by wavelength and/or frequency (Khorram et al., 2012). The wavelength coverage of each spectral region is summarised in Table 1-2. Wavelength is typically expressed in terms of micrometres ($\sim 10^{-6}$ metres), millimetres ($\sim 10^{-3}$ metres) or metres (m) (Campbell & Wynne, 2011).

Table 1-2: List of spectral regions that are commonly used in remote sensing

Spectral regions	Wavelength (μm)	
	Minimum	Maximum
Gamma ray	0	0.00003
X-ray	0.00003	0.003
Ultraviolet	0.003	0.38
Visible spectrum	0.38	0.72
Infrared	0.72	1,000
Microwave	1,000	300,000
Radio wave	> 300,000	

Adapted from *Introduction to Remote Sensing* (p. 34), by J.B. Campbell and R. H. Wynne, 2011, New York: Guilford Press.

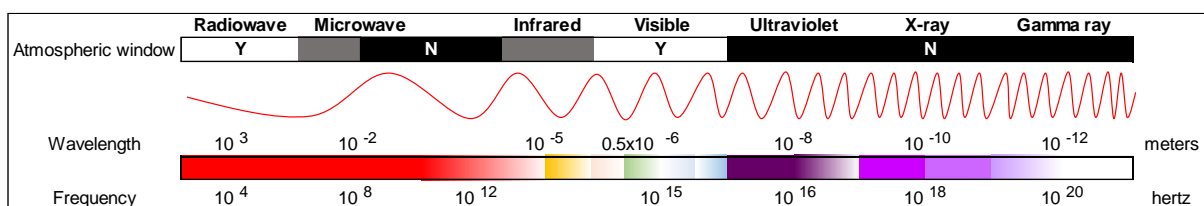
In remote sensing by optical satellite imagery, an image is comprised of several spectral channels or bands. These spectral channels are subsections of each spectral region as shown in Table 1-3. However, not all sensors are comprised of these spectral channels. Rather, every sensor contains selected spectral channels, which suit its sensing objective. These spectral channels are confined within narrow bandwidths (e.g. blue, green and red spectral channels), and are used to characterise Earth features based on the brightness intensity as received by the sensor for each spectral channel. Only three spectral bands can be used at a time to display an image either at its natural or false colour composites (Horning et al., 2010). There are various combinations of spectral bands, and the significance of each combination depends on the type of information sought about the object. The combination of blue, green and red spectral bands represents a true colour composite, which is visible to the naked eye. Other combinations, known as false colour composites, include the application of other channels of infrared light (Table 1-3), which is useful for activities such as health monitoring of vegetated areas (Khorram et al., 2012). In contrast, multiple spectral bands can be integrated into a multispectral image through the application of indices. Indices perform series of arithmetic equations over selected spectral channels with which, a ground object of interest has distinct spectral response to each of them. Indices are used to detect and isolate a ground object from the rest of land covers to perform both qualitative and quantitative analyses.

Table 1-3: Spectral channels of selected spectral regions

Spectral channels	Wavelength (μm)	
	Minimum	Maximum
Visible spectrum		
Violet	0.4	0.446
Blue	0.446	0.5
Green	0.5	0.578
Yellow	0.578	0.592
Orange	0.592	0.620
Red	0.620	0.7
Infrared light		
Reflected infrared (Near and mid-infrared)	0.7	3
Thermal infrared	3	100

Adapted from “Remote sensing basics and application,” by R.R. Navalgund, 2001, *Resonance*, 6(12), p. 51-60; *Fundamentals of Remote Sensing* (p.10-11), by Canada Centre for Remote Sensing, no date.

If a satellite is the choice of platform, only selected spectral regions can penetrate through the atmosphere and transmit signals to the satellite sensor. These spectral regions are known as the atmospheric window. Among these spectral regions, the visible spectrum, infrared and microwave are commonly being used in remote sensing of Earth features (Figure 1-1).

**Figure 1-1:** Spectral regions of an electromagnetic radiation

Adapted from Wikimedia Commons, NASA. (Created and simplified through Microsoft Excel 2013)

The limitation of satellite imaging is of particular importance in humid climates where water vapour, an effective absorber of radiation, is dominant (Campbell & Wynne, 2011). In addition, spectral regions at wavelengths shorter than 0.3 micrometre experience strong scattering from the upper atmosphere's molecular constituents, such as nitrogen and oxygen, during its travel from the earth's surface and back into the sensor (Navalgund, 2001). In contrast, longer wavelengths are highly scattered in the lower atmosphere where large particles such as fumes and haze are present. These scattering effects are known as Rayleigh and Mie scattering (Richards, 2013). Furthermore, nonselective scattering occurs in the presence of larger particles, such as dust and water droplets. These particles cause all light forms to scatter in equal quantities (Campbell & Wynne, 2011). These effects are removed through the application of an atmospheric correction algorithm, which is performed right after normalising the spectral values of the image scene.

1.3.1.2 Spectral signature

The degree of light absorbance, emission and reflectance of an object over a defined range of wavelengths forms its spectral signature (Khorram et al., 2012). Spectral signatures provide information on the intensity of Earth features, which are transformed into a digital image. There are established libraries of spectral signatures that represent general types of land cover (Figure 1-2) and are usually plotted using the percent reflectance unit. For advanced applications, combined with object delineation, spectral signatures can be used to determine an object's size, shape, physical and chemical properties from a distance (Parker & Wolff, 1965; Campbell & Wynne, 2011). However, caution needs to be taken, as a spectral signature normally changes seasonally. The visible spectrum is sensitive to changes in the intensity of an object, particularly in a vegetated area where its colour is determined by the amount of leaf pigments. In contrast, the infrared region is more responsive to moisture availability. Furthermore, moisture availability is equally as important as the land surface temperature (LST) when using the thermal region. On the other hand, the spatial distribution of properties of the Earth's surface also affects the spectral signature, as smaller objects that fit within a larger feature influence the intensity.

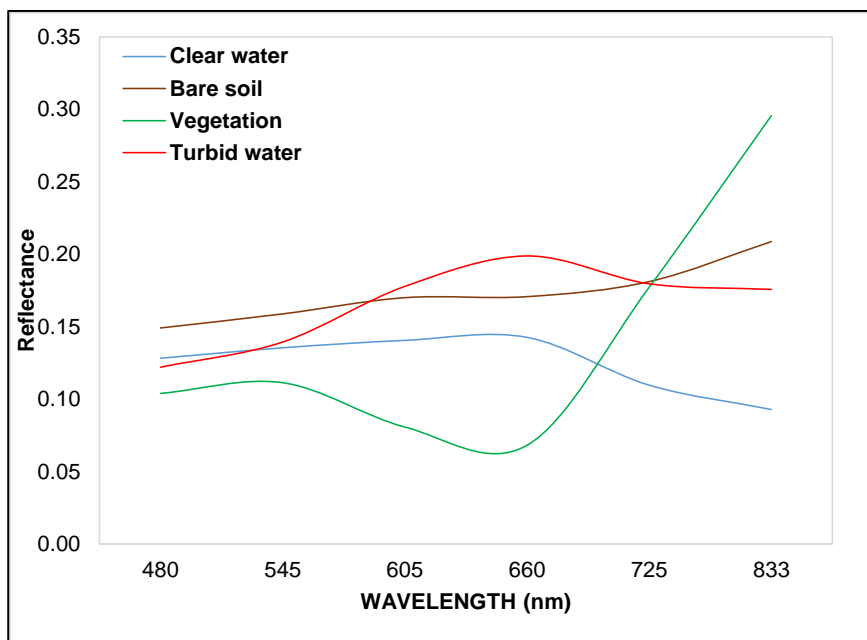


Figure 1-2: Spectral signatures of land cover and other land features

1.3.2 Resolution of sensors

1.3.2.1 Spectral resolution

Spectral resolution is the measure of a sensor's capability to elucidate the spectral signature of an object by means of available spectral channels (Navalgund, 2002). A crude plot of spectral signature is usually generated from multispectral images (e.g. four-band image), due to limited spectral channels. Whereas hyperspectral images, which are composed of more than 10 spectral channels with narrow band widths, can provide a finer representation of the spectral signature. Most of the available multispectral images have spectral channels with blue, green and red portions in the visible spectrum and the near-infrared. Those satellite imageries with higher spectral resolution can further divide the visible spectrum into blue, green, yellow, red and red edge and several bands of near and shortwave infrared.

1.3.2.2 Spatial resolution

A satellite image is delivered in the form of digital data. The image is captured within the viewable surface area of the sensor at a given altitude of the satellite known as the field of view (FOV) of a sensor (Richards, 2013; Canada, Fundamentals of Remote Sensing, no date). The FOV is composed of an array of pixels. A pixel is the smallest resolvable unit of an image with which, their side length corresponds to the spatial resolution (Chin, 2001; Hussain et al., 2013). The size of the pixel is the spatial resolution of a raw image. More pixels display images with higher spatial resolution. Higher spatial resolution introduces a greater volume of data, but they reduce the unambiguity of the boundaries of less significant ground features.

Each pixel contains the spatial attributes and texture of an Earth feature (Khorram et al., 2012). Several Earth features that rest within a pixel are averaged to represent the level of brightness. As such, an Earth feature smaller than a pixel is undetectable from adjacent objects, which is an issue related to the aggregation of signals. For satellite platforms, spatial resolution usually ranges from 0.50 m to 1,000 m. Aircraft can provide a spatial resolution finer than 0.50 m but at higher cost. At present, the drawback of satellite imaging is spatial resolution. Satellite images usually come in sets of multispectral bands (MS) and a panchromatic band (PAN), which are captured by two different sensors. The PAN band sensor is sensitive to radiation over a broader range of wavelengths (Kpalma et al., 2014). It extends from the visible spectrum to the shorter wavelength of the infrared spectrum, thereby providing a higher amount of energy (higher signal to noise ratio), which makes it possible

to have higher spatial resolution but with the absence of spectral details (e.g. image object's specific colours) (“Radiometric resolution”, 2016). As a result, a number of algorithms, known as panchromatic sharpening, are being developed to fuse multispectral bands with a panchromatic band, with the enhancement of the image spatial feature at minimum distortion of spectral information (Amro et al., 2011; Johnson, 2014; Zhang & Roy, 2016). This method is not applicable to image analysis that is reliant on absolute pixel values (Colditz et al., 2006).

1.3.2.3 Radiometric resolution

“Radiometric resolution” refers to the ability of a sensor to detect differences in brightness between pixels, and is expressed as a binary digit for each spectral band (Richards, 2013). It is the number of discrete brightness values that can be detected within a spectral band and is expressed as a unitless digital number (DN) (Al-Fares, 2013). As indicated in Eq. 1.3.1, the binary digit is used as an exponential factor to determine the size of DNs that can be assigned for each discrete brightness.

$$\text{Digital number (DN)} = 2^{\text{BD}} \quad (1.3.1)$$

Where:

BD Binary Digit

Every sensor has a relative radiometric resolution, which determines its range of DNs. For the practical comparison of different satellite products, the DNs need to be converted to a physical unit. DNs can initially be converted to spectral radiance (L_λ). The spectral radiance as a function of wavelength (watt m⁻² steradian μm^{-1}) is the amount of energy transmitted to the sensor per square metre on the ground, for one steradian, per unit of wavelength (Newcastle University, no date). The gain represents the gradient of spectral radiance for every value of DN, while the offset is the radiance coefficient when the DN is zero (Crippen, 2007). For more accurate radiometric calibrations, radiance is further converted to top-of-the-atmosphere (ToA) reflectance, which provides a definite brightness measurement of pixels directly below the sensor. The ToA reflectance is the ratio of transmitted radiance within the sensor's field of view and solar irradiance emitted by the normal sun to a reflecting ground surface (Price, 1987). It is a unitless absolute measurement, which ranges in value from 0 to 1, or sometimes expressed as a percentage (Campbell & Wynne, 2011).

1.3.2.4 Temporal resolution

Temporal resolution refers to the length of time before a satellite image data is available for another acquisition (Al-Fares, 2013). The acquisition frequency is described by the platform's revisit time, and usually takes a day or more for most satellites. The revisit time is equivalent to the time of a single revolution for a satellite to return to the same point. However, the earth's path length changes between revolutions. In this regard, the satellite's sensor that has a rotating mirror captures an image on the ground at an angle, in order to maintain closeness of capture to its intended acquisition time. This allows the sensor onboard to capture multiple images at various angles. In the case of a non-revolving satellite, the sensor uses an array of detectors that capture a row of images within its swath width as it moves forward. This mechanism of image acquisition is known as the push-broom technique (Richards, 2013).

1.3.3 Types of sensors

Sensor radiation comes from several sources. Those that depend on natural sources, such as sun or the Earth, are known as passive sensors. Satellite platforms include Landsat, GeoEye-1, IKONOS, Pleiades, Quickbird, RapidEye, SPOT and WorldView. In contrast, an active sensor emits its own radiation towards an Earth feature. Active sensors, specifically those that utilise the microwave region, have more penetration capability through thick clouds, dense forests and soil surface thus they can secure ground information at anytime during the day (Campbell & Wynne, 2011). Typical active sensors include light detection and ranging (Lidar), radio detection and ranging (Radar), altimeters and scatterometers (Navalgund, 2002).

Furthermore, sensors are also distinguished by their use of specific spectral regions to generate an image. Optical sensors use the visible spectrum and infrared to provide information such as geometry, radiometry (e.g. intensity of brightness), spectral features (e.g. color and hue) and texture (e.g. roughness or smoothness) (Chin, 2001). On the other hand, microwave sensors offer the ability to gather different sets of information, such as geometry, surface roughness, temperature and soil moisture (Telmer & Stapper, 2007). Radar imagery that uses microwave provides a crisp portray of drainage, topography and other ground structures (Campbell & Wynne, 2011). Figure 1-3 provides an illustration of a flowsheet of how these classifications of sensor overlap.

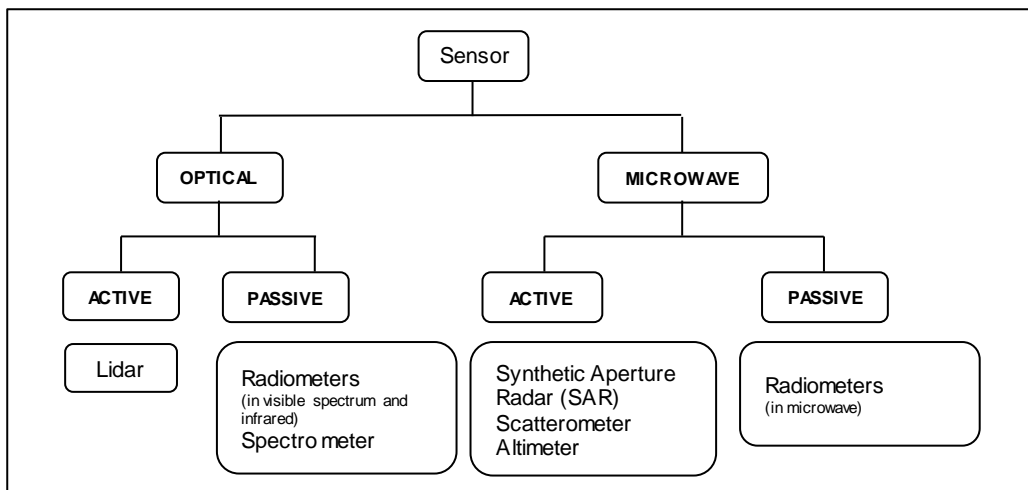


Figure 1-3: Types of sensors based on source of illumination and use of spectral region

Adapted from “Remote sensing sensors and platforms,” by R.R. Navalgund, 2002, *Resonance*, 7(1), p. 38. Adapted with permission.

In remote sensing, irradiance quantifies the strength of the emitter of energy, while radiance measures the energy that is transmitted back to the sensor (Richards, 2013). Both variables, as functions of wavelength, are expressed in terms of watts per steradian per square metre ($\text{W sr}^{-1} \text{ m}^{-2}$). Typical optical imageries operate from 0.4 to 2.29 μm , and irradiance detected by a sensor within this range completely originates from the sun. Its energy ranges from 0.1 μm and peaks at 0.5 μm with a temperature of $5,950 \times 10^3$ Kelvin (K). In contrast, the Earth’s irradiance peaks at 10 μm at about 300×10^3 K (Richards, 2013). Thermal images are produced at this range of wavelength (8-14 μm), which are useful for determining the temperature of land cover. Landsat-8 offers spectral bands within this range of wavelengths (Landsat Missions, no date).

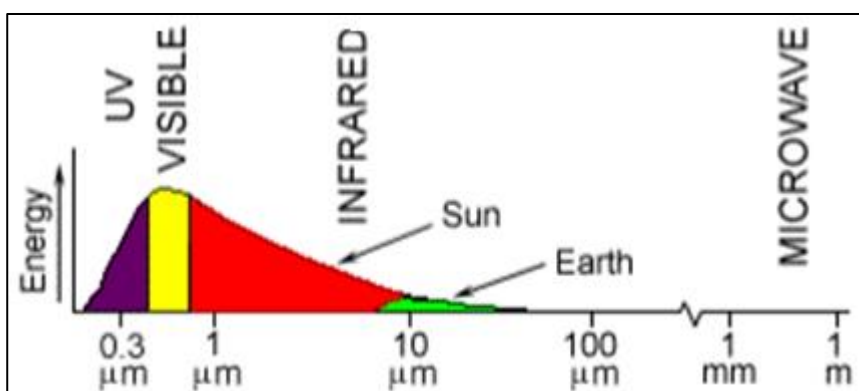


Figure 1-4: Sources of light for each spectral region

Adapted from *Fundamentals of Remote Sensing* (p.10-11), by Canada Centre for Remote Sensing, no date.

1.3.4 Different approaches to image analysis, and their corresponding application in delineating small-scale mining regions

1.3.4.1 Classification using the pixel-based approach

Pixel-based image analysis is a traditional approach that is solely dependent on the pixel spectral properties (Hussain et al., 2013). Prior to classification, pixels are clustered into polygons to represent different land use features in the image. Selected polygons represent the training data, and are used by a supervised classifier as the data source to determine certain statistical measurements such as the minimum and maximum values, mean and standard deviation. Known pixel-based classifiers include, maximum likelihood, principal component analysis (PCA), decision tree, support vector machine (SVM) and artificial neural network (ANN) (Hussain et al., 2013). Based on a previous study (Warner & Nerry, 2009), SVM is known for its excellent performance with complex distributions of land use features (Warner & Nerry, 2009). The SVM is the most contemporary classifier, which is non-parametric, and does not depend on statistical distribution of pixel values (Taati et al., 2014). Instead, it uses a learning algorithm that linearly fits high-dimension object features, and can be optimised to reduce regression error based on least square method (Han et al., 2007). The classifier is not excessively susceptible to Hughes phenomenon, which decreases the accuracy of classification if supplementary attributes are added (Hughes, 1968; Warner & Nerry, 2009). Moreover, it only requires training samples that completely represent each land use features that are composed of mixed pixels. As the classifier delivers an output with lower uncertainty (Oommen et al., 2008; Yousefi et al., 2015), the training data does not necessarily need to be large in size (Lin et al, 2015). It determines the optical boundaries among image classes with the inclusion of supplementary data in addition to spectral channels of the satellite image. To conclude, SVM can deliver higher classification accuracy compared with the other classifiers (Halder et al., 2011; Mountrakis et al., 2011; Yousefi et al., 2015). Previous researches as discussed below employed traditional approaches of classifying small-scale mines, which involved pattern recognition based on statistics of spectral values of pixels. On the other hand, the efficacy of SVM classifier in investigating small-scale mines was not yet tested. It was observed that there is an absence of structural homogeneity (e.g. complex and irregular landscape) in small-scale mines, which can be addressed by machine learning algorithms (e.g. SVM classifier).

In 2007, the dynamics of small-scale mining in Central Kalimantan, Indonesia were mapped using satellite products (Telmer & Stapper, 2007). The region is known for its gold deposits and traces of zircon. To recover the minerals, particularly the gold, small-scale miners employ several techniques, which include dredging (e.g. Kahayan River), construction of open-pit mines and the use of ball mills.

Several scenes from Landsat-5 and Landsat-7 (30 m spatial resolution) had been collected, and a supervised classifier (maximum likelihood classifier) was employed to separate eight identified land use features. Among these land uses, three forms of small-scale mines were designated namely; ponds within a pit, established sediment pits and stripped soils associated with a mix of mining, timber cutting and burning activities. During post-classification, the determined coverage of small-scale mining was found to be underestimated. Alluvium mining techniques such as river dredging were not detected during the image analysis. The misclassification of alluvial mining was due to two factors; coarse resolution of Landsat imagery and difficulty in delineating the boundary between the riverbanks and alluvial mining, which seasonally changes based on river depth.

A study on small-scale mining in the Brazilian Amazon was performed in 2015 (Lobo et al., 2016). In this research, Terraclass map, a publicly available map of Brazil, presents a delineation of its deforested areas in 2010. It was used as the basis for image analysis undertaken on a 2012 Linear Imaging Self Scanning Sensor-III (LISS-III) satellite image (composite image of red, near-infrared and green bands). During image analysis, all forms of potential mining areas within the Tapajos River Basin were combined within the same class. A manual classification was performed to include mines at smaller-scales as the estimation of this land use feature was underestimated in the Terraclass maps.

1.3.4.2 Geographic-Object-based segmentation

The Geographic-Object-based Image Analysis (GEOBIA) segmentation technique was formulated in the period between the late 1970s and 1980s (Haralick & Shapiro, 1985; Blaschke, 2010). However, its application in the period immediately after its formulation was deferred due to the limitations in spatial resolution of imageries and limitations of computing software (Platt & Rapoza, 2008). Conversely, more recently software has been designed for remote sensing, including programs such as eCognition, ENVI's Feature-extraction module and IMAGINE Objective, which are capable of executing GEOBIA (Hussain et al., 2013). The main feature is the ability to form homogenous regions called segments. A homogenous region or object is a group of pixels with similar spatial, spectral and textural properties (Myint et al., 2011). Unlike the pixel-based image analysis, each property in image segmentation considers multiple attributes (which are summarised in Appendix F). It is particularly suitable for classification at a scale where a pixel is smaller than the object of interest. The GEOBIA technique has several advantages over the pixel-based approach (Kalkan et al., 2013). Firstly, segments establish the optimum boundary of potentially known classes based on the preferred scale of the user. In addition, the algorithm which merges adjacent objects with associated attributes provides flexibility for the selection of components that should be part of a segment. Secondly,

segmentation forces all pixels to be separated by attributes, thereby eliminating the effect of shadows, high spatial frequency noise and geometric errors induced by sensors.

In a study on an area of the Republic of Congo, a ten-metre spatial resolution was assumed as the detection limit for illegal mining areas for gold, cassiterite (tin ore) and coltan (tantalum ore). The selected high resolution imagery (e.g. IKONOS) and very high resolution imageries (e.g. GeoEye-1, RapidEye) were integrated with the Geographic Object-based Image Analysis (GEOBIA), provided by eCognition8 software. Using textural properties such as entropy, which is defined as the randomness of neighboring pixel values within a segment, the area of interest (AOI) was delineated (Luethje et al., 2014).

Furthermore, object-based classification based on a set of rules using eCognition was recently used in small-scale mines in the region of Upper Mazaruni, Guyana (Mengisteab et al., 2015). The classification of mining sites had user's and producer's accuracy of 100% and 67%, respectively. However, the identification of scattered sediment pits, which were described to have high level of mining activity, generated comparable producer's accuracy with large-scale hard rock mines, but a lower user's accuracy of 57% using a Landsat-5 image in 2010 and 57% using a RapidEye-1 image in 2011.

1.3.5 The application of remote sensing to modelling water turbidity and total suspended solids

The quality of water bodies is determined by the components of their physical, chemical and biological properties (Liu et al., 2003). They are explained in terms of certain attributes known as parameters or quality indicators, which are measured at the discharge outlet of natural water bodies (Benedini & Tsakiris, 2013). Among these parameters, stream sediments serve as visual indicators of water quality and are measured as total suspended solids (TSS) (mg L^{-1}) and turbidity (Nephelometric turbidity Units: NTU) (Ritchie et al., 1987). These indicators are also used to determine the trophic condition of aquatic ecosystems (Zhang et al., 2003).

The principal factors affecting TSS and turbidity include catchment lithology, anthropogenic activities and atmospheric and climatic condition (Shrestha & Kazama, 2007). In a hydrological catchment, their impacts are quantified based on the quality of the water discharged. Streamflow or discharge (m^3/s) is the principal agent of stream sediment transport, the rate of which is influenced

by rainfall (mm/day) and vegetation cover (Robert et al., 2016) as well as by channel slope and sediment yield of the sub-catchment.

1.3.5.1 Monitoring of catchments by remote sensing

1.3.5.2 Empirical and analytic models

For studies that determine the health of water bodies, indicators such as suspended solids and turbidity have been regularly utilised. For instance, water turbidity has been used as the surrogate to determine the amount of light available at a depth for benthic habitats, whereas total suspended solids is recommended for quality monitoring of coastal waters (Dorji et al., 2016). In-situ measurement is a preferable measurement approach, but does not provide a synoptic view of the spatial and temporal variation in suspended solids/turbidity and their potential associations with land use changes (Ritchie et al., 1987). To achieve this, remote sensing technology, particularly the application of high spatial resolution satellite imageries, is potentially suitable in obtaining spectral information both in coastal and inland waters.

There are three approaches that are involved in the modelling of turbidity using remotely-sensed reflectance data, the approaches being empirical models, analytic models and semi-analytic models (Table 1-4). Based on Dorji et al. (2016), the empirical models use either linear or exponential equations to relate in-situ measurements of total suspended solids to surface reflectance. Secondly, the analytic type of model applies radiative transfer theory, which utilises the field data of inherent optical properties (IOP) and apparent optical properties (AOP) of water and atmospheric conditions. It is important to include coefficients of light absorption, attenuation and scattering, during the transfer of radiation. Finally, the semi-analytic model uses the analytic model to define the relationship between total suspended solids and reflectance as far as possible using available optical property measurements, and it uses the empirical approach to estimate the parameters of the relationship.

The estimation of total suspended solids concentration is associated with a remotely-sensed image to calibrated surface reflectance. Through the application of regression models, the reflectance from each spectral band that corresponds to a point sampling station is determined. The correlation of determination (R^2) and root mean-square error (RMSE) of the water attribute for each spectral band is computed to determine the accuracy of the dataset (Syahreza et al., 2012).

These modelling approaches are frequently applied to coastal waters and large lakes, where the total suspended solids concentration is less than 50 mgL^{-1} (Ritchie et al., 1987). On the other hand, several researchers have tested their applicability to small lakes, reservoir and rivers. Firstly, the research performed by Syahreza et al., 2012 used satellites images of Kelantan River in Malaysia. This images were secured through the Advanced Land Observing Satellite (ALOS) using the Advanced Visible and Near Infrared Radiometer type-2 (AVNIR-2) sensor. These images were calibrated into surface reflectance, and a linear relationship between surface reflectance and in-situ turbidity measurements was established. It was found out that spectral band 2 (green~520-600 nm) and band 3 (red~610-690 nm) of this sensor can explain the behaviour of river turbidity with an R^2 value of 95.4% and RMSE of 2.26 NTU. Secondly, siltation of Tapajos River in Brazil due to small-scale mining was investigated utilising the Landsat-5 Thematic Mapper (TM) sensor during high water level and the Linear Imaging Self-Scanning System III (LISS-III) sensor integrated with the Indian Remote Sensing Satellite (IRSS), during low water level season (Lobo et al., 2016). Thirty-nine water samples were collected at various measurement levels of TSS, and with correpsonding reflectance data. A power curve was derived between TSS and red band (~620-690 nm) of these sensors resulting to an R^2 value of 94% and RMSE of 1.39 mgL^{-1} . Lastly, through the application of Landsat-5 Multispectral Scanner (MSS) sensor, inland waters such as the Moon lake near Mississippi River in Coahoma County were observed to be highly responsive to spectral band 4 (near infrared 2~ 800-1,100 nm) whereas suspended solids measurement levels can be characterised using band 2 (red~600-700 nm) and band 3, respectively (near infrared 1~700-800 nm) (Ritchie et al., 1987).

1.3.5.3 Derivative products of a Digital Elevation Model (DEM)

A Digital Elevation Model (DEM), particularly those with higher vertical resolution is useful for derivative works on topography (e.g. contour mapping) and hydrological modelling (Oh & Lee, 2011). An Interferometric Synthetic Aperture Radar (IFSAR) DEM, with an adequate vertical resolution of 5 m, can be used as supplementary data for the SVM classifier to provide information on ground surface depressions present in small-scale mines. Furthermore, the DEM can be used to generate a hypsometric curve of each sub-basin of Didipio catchment (Verstraeten & Poesen, 2001), and to develop maps of variables that affect sediment yields, such as slope, catchment area and hydrology. The hypsometric curve and/or hypsometric integral provides information on the age of a drainage basin. The hypsometric curve represents the surface area above or below a given ground elevation while hypsometric integral is the area below the hypsometric curve or can be computed by an equation (Pike and Wilson, 1971; Perez-Pena et al., 2009) (Table 1-4). Principally, they are being utilised in the study of landscape geometry, which is known as the field of geomorphometry (Mark,

1975). They assist on identifying the dominant lithological movements in the drainage basin that determine its present configuration (Strahler, 1952; Perez-Pena et al., 2009). Also, they can be used to evaluate the potential of a catchment to yield sediments, and identify the dominant topographic factor based on its age that causes such amount of sediments. For this study, hypsometric curve was used to appraise the configuration of each sub-basin that comprises of the rivers that were monitored. Their configuration was associated with topographic factors that contribute to increasing suspended solids over the assigned monitoring stations.

1.3.5.4 Vegetation Indices

Vegetation Indices (VI) in general are used in remote sensing to delineate areas with vibrant vegetation cover against barren land and water bodies. It also provides spatial information to assess degradation of lands (Yengoh et al., 2016). To evaluate the growth density of vegetation, two or more spectral bands are merged to take advantage of the vegetation's varying responses to these bands (Table 1-4). Vegetation indices reduce the effect of image geometry, properties of the canopy, the influence of soil reflectance and atmospheric molecular composition (Huang et al., 2008; Dorigo et al., 2007; Oldeland et al., 2010). Various VIs use different ranges of numerical values. Normalised Difference Vegetation Index (NDVI), the selected VI for this research, is expressed as dimensionless numerical values that range from -1 to 1. The presence of green leaves leads to high positive values relative to bare soil. In contrast, snow, water and the interference of clouds yield negative index values.

Table 1-4: List of model equations

Model	Equations and variables
Analytic approach	<p>Total absorption:</p> $a(\lambda) = a_w(\lambda) + M_{ph} * a_{ph}(\lambda) + M_{CDOM} * a_{CDOM}(\lambda)$ $b(\lambda) = b_{bw}(\lambda) + M_{bp} * b_{bp}(\lambda)$ <p>$a_i(\lambda)$ = mass-specific absorption spectrum (w = water, ph = phytoplankton, CDOM = dissolved organic matter) $b_i(\lambda)$ = mass-specific absorption spectrum (bw = water, bp = particles) M_i = concentration</p> <p>Backscattering albedo:</p> $u(\lambda) = \frac{b_b(\lambda)}{a(\lambda) + b_b(\lambda)}$ <p>Sub-surface reflectance:</p> $r_{rs} = 0.0949u(\lambda) + 0.0794u(\lambda)^2$ <p>r_{rs} = Subsurface reflectance</p>
Empirical approach (linear regression)	$D_{TSS} = A_0 + \sum_{n=1}^{\infty} A_n (R_1) + A_2(R_2) + A_i(R_i) + \epsilon$ <p>A_0 = y-intercept (constant) A_i = slope coefficient for the ith explanatory variable ϵ = remaining unexplained noise in the data (error) $R_{1,2,i}$ = reflectance of the object (e.g blue band, red band, green band) D_{TSS} = Predicted value of total suspended solids</p>
Vegetation Index (VI)	<p>Normalised Difference Vegetation Index (NDVI):</p> $\frac{(NIR - Red)}{(NIR + Red)}$ <p>NIR = Near-infrared band Red = Red band</p>
Hypsometric Integral (HI)	$\frac{(H_{mean} - H_{min})}{(H_{max} - H_{min})}$ <p>H_{mean} = Mean elevation of the catchment H_{min} = Minimum elevation of the catchment H_{max} = Maximum elevation of the catchment</p>

Adapted from “Hyperspectral Sensing of Turbid Water Quality Monitoring in Freshwater Rivers: Empirical Relationship between Reflectance and Turbidity and Total Solids,” by Jiunn-Lin Wu et al., 2014, *Sensors*, 14, p. 22675.

“Factors controlling sediment yield from small intensively cultivated catchments in a temperate humid climate,” by G. Verstraeten and J. Poesen, 2001, *Geomorphology*, 40(1-2), p. 128.

Retrieved May 5, 2017, from <https://oceancolor.gsfc.nasa.gov/atbd/giop/>

1.4 Knowledge gaps in previous studies

In this research, the diffuse and usually remote nature of small-scale mines suggests that traditional ground-surveys are likely to be impractical. Ground-surveys may provide temporal information on ASM development at a limited scale. Moreover, such surveys do not facilitate a straightforward

interpretation on the spatial dimension of an object of interest (e.g. total suspended solids) with its relationship on the observable trend that is captured through time (George, 1997). The approach also consumes more time (Dekker et al., 2001; Wu et al., 2014); therefore, there is a need for an alternative monitoring method that is cost-efficient (Wu et al., 2014), provides an unbiased view (Giri, 2012), and can be done on a repetitive basis at a regional scale (Schmugge et al., 2002).

Furthermore, remote sensing can provide an extensive examination of land use development, and its impact to the environment. It has a number of techniques and algorithms, which are readily available to be tested. However, due to circumstantial existence of artisanal and small-scale mining particularly in wet tropical regions, the remote sensing application for this task still requires recommendations on suitable image products and image specifications. In addition, there is limited research in mapping small-scale mines, and investigating their corresponding impacts to river quality through a selected hydrological model (Telmer & Stapper, 2007). Also, there is a need to examine various remote sensing techniques that can provide spatial explanation on ASM impact to river quality.

Chapter 2 Description of the Case Study Area

The case study area is described in this chapter. It includes descriptions of its geography, geology, existing land use, topography, hydrological catchment and regional climate. These details were acquired from a technical report prepared for OceanaGold (Philippines) Incorporated in 2010 and an Ecological Assessment Report in 2013. Additional information was extracted from spatial data provided by the Mines and Geosciences Bureau (MGB), Region 2 and the Philippine National Mapping and Resource Information Authority (NAMRIA).

2.1 Regional location of the case study area

The Philippines is geographically located in Southeast Asia, near the equator. The country is completely surrounded by huge bodies of water such as the South China Sea in the west, Philippine Sea in the east and Celebes Sea in the south. It is an archipelago that is comprised of 7,107 islands, and it has an overall land area of 300,000 km² (Philippines National Demographic and Health Survey 2008, 2009). These islands can be grouped into three greater landforms, namely, Luzon, Visayas and Mindanao. Luzon is the largest among the three, with 47% of the total land area.

The Cagayan River Basin (CRB) is situated in the northeast of Luzon Island. The CRB has a drainage area of 27,700 km², and is known to be the largest river basin in the Philippines (Principe, 2012). Its surface area extends over the Cordillera Administration Region (CAR) and portion of Central Luzon (Principe, 2012). The CRB has an elliptical shape with a major north-south axis (Department of Environment and Natural Resources, 2011). In addition, the CRB is divided into 15 smaller basins. The case study area is in the Addalam River Basin (ARB). This basin has a surface area of 1,047 km², which includes the provinces of Isabela, Nueva Vizcaya and Quirino, which are further divided into ten municipalities (Table 2-1).

Table 2-1: Districts that form the Addalam River Basin

Provinces	Municipalities	Area km ²
Isabela	San Agustin	7
	Jones	32
Nueva Vizcaya	Bambang	12
	Dupax Del Norte	43
	Kasibu	245
Quirino	Aglipay	175
	Cabarroguis	135
	Diffun	19
	Maddela	53
	Nagtipunan	324

Adapted from Georeferenced Administrative Map of the Addalam Sub-River Basin, by Mines and Geosciences Bureau (MGB), Region 2 Cagayan Valley.

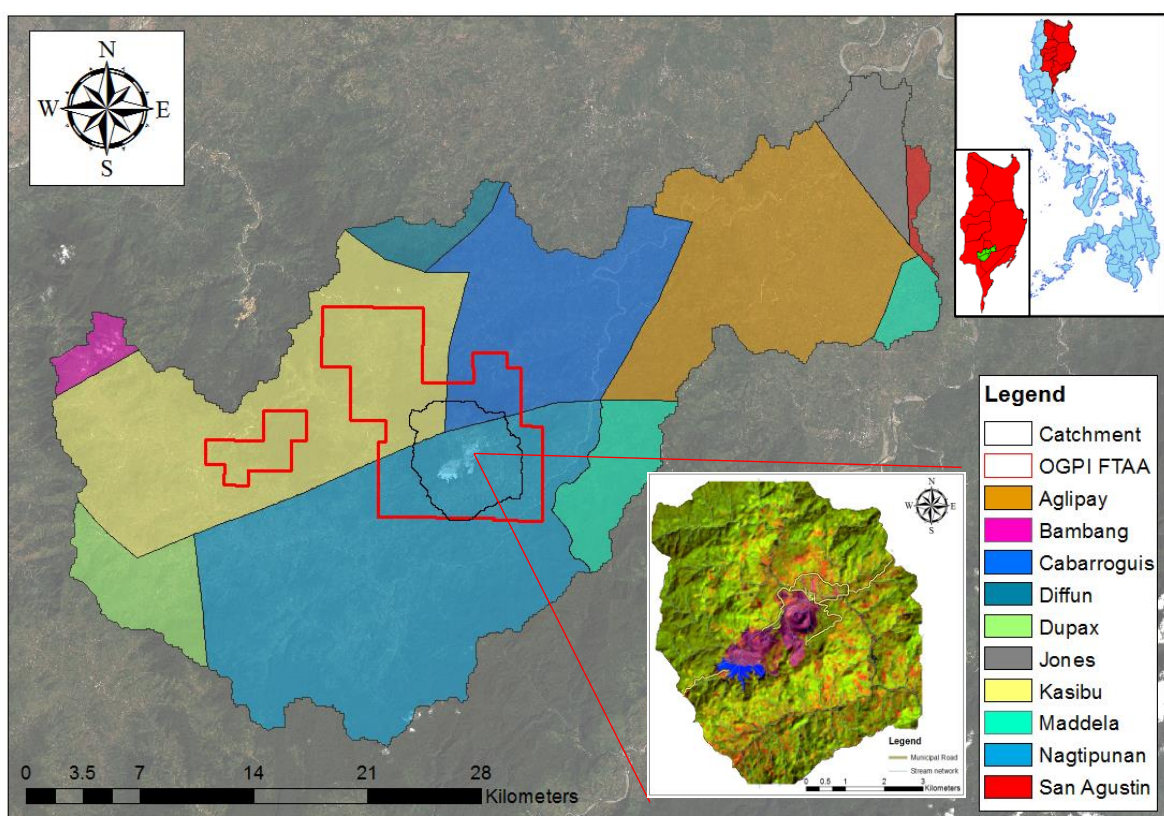


Figure 2-1: The Addalam River Sub-Basin on Luzon Island

Note. A derivative work from Georeferenced Administrative Map of the Addalam Sub-River Basin, by Mines and Geosciences Bureau (MGB), Region 2 Cagayan Valley. The Landsat-8 image was downloaded from USGS (<http://earthexplorer.usgs.gov/>)

At the centre of the Addalam River Basin, the Didipio project of OceanaGold (Philippines) Incorporated mines gold and copper within an area (130 km²) of mineralised land. The mineralised land area is governed by a Financial and Technical Assistance Agreement with the Government of the Philippines, and was granted an Environmental Compliance Certificate (ECC) by the Department

of Environment and Natural Resources (DENR) as part of its Partial Declaration of Mine Feasibility (PDMF) (Figure 2-1). The FTA, an agreement provided to a contractor duly operated by both foreign and Filipino-owned corporations, grants the mineral rights to explore, develop and utilise metallic resources within the applied area.

2.2 Access and Transportation

The case study area is accessible by two different roads. Through Quirino province, a 22-km paved road provides access from Cabarroguis (located in the northeast) to the site, and it is suitable for off-road vehicles, buses and large trucks. The site is also accessible via the Wangal road, which intersects the Maharlika Highway at Nueva Vizcaya. The Wangal road is unsealed and rough, and mainly suitable for off-road vehicles and small trucks only.

2.3 Geology

2.3.1 Regional Geology

Sediments and volcanics are the predominant rock formation in the Cagayan River Basin. Based on the geologic time scale, they were formed between the late Tertiary (Pliocene epoch) and early Quaternary (Pleistocene age) periods (McIntyre et al., 2010). The surrounding marine and terrestrial sediments are older, which were formed in the mid Tertiary period (Oligocene to Miocene epoch). The lower portion of the Didipio project area extends over the area of rock formation, while the upper northeastern area comprises mostly by marine sediments and volcanics formed during the late Mesozoic era (Appendix A).

2.3.2 Local Geology

The local geology of the Didipio project area is composed of both volcanic and sedimentary rocks that are intruded by porphyries from intermediate to felsic composition (McIntyre et al., 2010). The Didipio Gold-Copper deposit is entirely composed of alkali gold-copper porphyry body, which is made of igneous complex; therefore, there is less traces of sulfides that is a possible source of AMD during exposure of rocks to weathering. It has the Dinkidi Stock that embodies the Didipio Gold-Copper deposit. It has a roughly elliptical shape with a major axis that extends up to 450 m and a minor axis of 150 m wide. The deposit has a pipe-like geometry with a depth from 800 to 1000 m below the land surface. The porphyry intrusive body is associated with K-feldspar alteration that is

composed of small porphyritic monzonite rocks that intrude into dark diorite. The quartz-free portion is associated with gold and has a general grade between 2 and 8 grams per tonne (g/t).

2.4 Land use and land cover

The catchment of the Didipio mine area is mainly dominated by flora. Tropical lowland evergreen rainforest can be found at elevations up to 529 m above sea level (MASL) (AECOM Philippines Incorporated, 2013). This forest is known to be the dominant specie in the area (Whitmore, 1984 as cited in AECOM Philippines Incorporated, 2013). However, the natural vegetation is being replaced by anthropogenic forms of land use, including small-scale logging and '*kaingin*' farming. At elevation from 700 to 1300 MASL, the prevailing vegetative cover is tropical lower montane rainforest. In Didipio catchment, this form of rainforest is mainly found in the area to the upper northwest of the open pit mine. In this area, the forest canopies are lower than the lowland rainforest. Grassland and fern thickets are normally present in areas cleared of forest cover. Most of the time, seasonal burning during the dry season is prevalent throughout this region. Traditional farming, including rice and *kaingin* are mainly practiced in areas immediately adjacent to the rivers. Brush land or open land, which comprises assorted plant species such as grasses and shrubs, is the product of revegetation after these areas were previously stripped of forest cover. Open lands are found scattered around the perennial crops.

2.5 Topography

In general, a mountainous landscape can be observed in Didipio. The steepest section of the catchment can be found at the northwest adjacent to Surong River and southeast of the open-pit mine (Figure 2-2). The case study area lies over an altitude between 750 and 990 m above sea level. The open-pit mine can be found at 700 m, while the small-scale hydraulic and underground mines are concentrated above 780 m. On the other hand, majority of the local community is located at north over an elevation of 690 m. Perennial crops exist alongside with open lands between the elevation of 620 and 720 m.

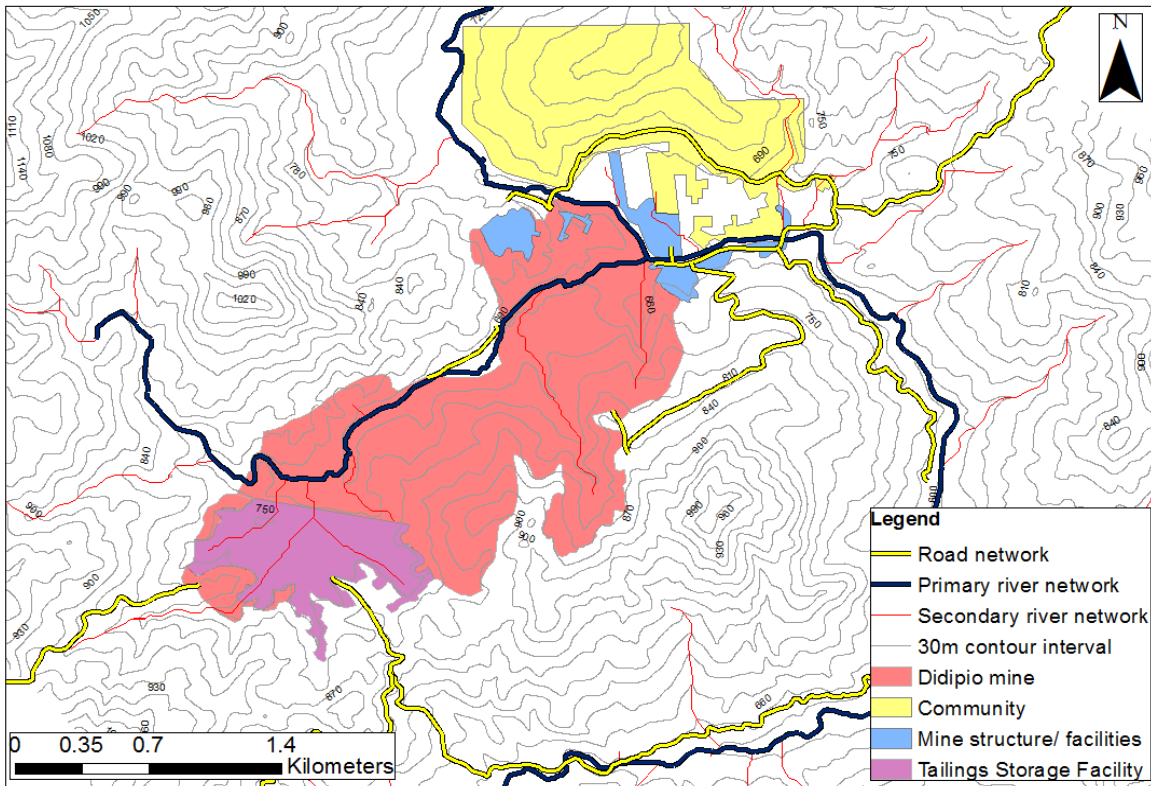


Figure 2-2: Topographic map of Didipio case study area

Note. A derivative work from the IFSAR DEM provided by the Philippine National Mapping and Resource Information Authority (NAMRIA).

2.6 Water catchment

In general, Didipio is a catchment composed of shallow rivers. Based on the records, the deepest river bottom is only 50 cm from the surface water level. The Dinauyan River is the main river that extends into the area of the open pit mine (Figure 2-3). It has a recorded maximum annual water flow of 27 Mm³/year. Another river in the catchment area is the Surong River, which forms a confluence with the Camgat River. Its maximum annual water flow is 36 Mm³/year (McIntyre et al., 2010). These rivers converge downstream at the Didipio River. Didipio River, in turn, joins with Alimit River. This catchment network is categorised as a Class D River based on the DENR Administrative Order No. 34 or the Philippine water quality guidelines. In addition to providing irrigation and drinking water for livestock, this catchment network is also primarily used as an industrial water supply. In general, these rivers have trace and heavy metals within the standard limit, except for elevated levels of suspended solids and mercury particularly in Didipio River (AECOM Philippines Incorporated, 2013).

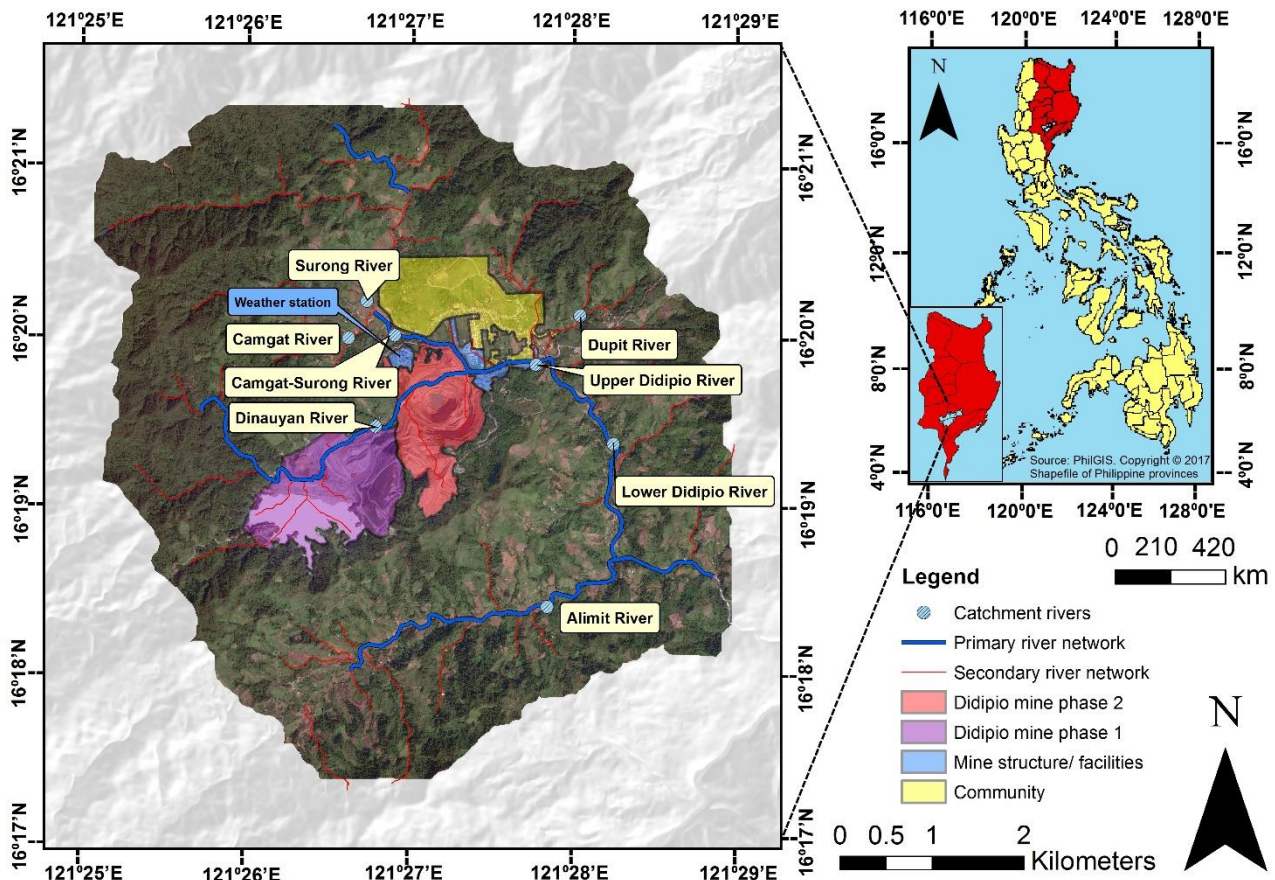


Figure 2-3: The section of Didipio catchment with available water quality data
SPOT: © AIRBUS DS (2016)

2.7 Climate

2.7.1 National climate

According to Philippine Institute for Development Studies (2005), the climate of the Philippines is characterised as being both maritime and tropical. Although the country has abundant rainfall, the temperature remains relatively high throughout the year. Humidity ranges from 71 to 85% throughout the year, reflecting the predominantly low altitude of the land and surrounding bodies of water. The mean annual rainfall ranges from 965 to 4,064 mm. In general, the country experiences two major seasons. Warm moist air predominates between May and September, being largely the result of southwest monsoons ('*Habagat*'), whereas cold and dry air is brought by the northwest monsoons ('*Amihan*') between October and March. The months from November to February are often affected by cold fronts, which bring additional rain.

Overall, within the Philippines, there are differences in climate among the regions based on rainfall distribution. According to Coronas classification, the climate of the Philippines is classified into four types (Table 2-2).

Table 2-2: Philippine climate based on Coronas classification

TYPE	DESCRIPTION
I	Dry season between November and April Wet season between May and October, being dominated by rain from June to September
II	There is no recorded dry season in the regions that experience type II. Minimum rainfall is experienced between March and May, while the rest of the year is dominated by heavy rain and thunderstorms
III	Dry season for three months only, either between December and February or March to May. The rest of the year experiences moderate rainfall
IV	There is no dry season while rainfall is evenly distributed throughout the year

Adapted from “Basics on Philippine Climatology,” by Philippine Institute for Development Studies, 2005, *Economic Issue of the Day*, V(2), p.2.

2.7.2 Didipio local climate

Didipio is located at the lower portion of the Cagayan Valley. It experiences the Type III tropical climate. Normally, southwest monsoons visit the region between June and September, while northeast monsoons are experienced from October to January. The months from February to May are a period of transition between the southwest and northeast monsoons. Didipio experiences the heaviest rainfall between September and November (McIntyre et al., 2010). March is the driest month. The average annual rainfall is 3,047 mm. The mean annual temperature and humidity of the mine site are 22.8°C and 82%, respectively. The site also experiences one or two typhoons annually.

2.8 Summary

The location of Didipio catchment was presented to be abundant in several natural resources and mineral deposits. In addition, alternative livelihoods are dominant at a scale that can independently support the local community within the region. The absence of potential source of sulfides is an advantage in the region; therefore, monitoring of river effluents can be focused on sediment generation of various land use features.

Several rivers in the catchment namely Camgat, Dinauyan, Didipio and Surong were among the principal source of water. It was documented that these rivers have acceptable level of trace and heavy

metals, but have observable concentration of suspended solids attributed to small-scale mines based on the ecological assessment of the catchment in 2013.

Moreover, there are no available data on the potential sediment yield of specific land use features in the catchment. However, the database of water quality parameters collected by OceanaGold within four years can show high level of river turbidity and total suspended solids, which are evidently cannot be observed in cultivated areas and open lands. That level of turbidity can be recognised as product of loose sediments that come from stripped topsoil. In addition, the sediment characteristics can be verified through its calibrated surface reflectance from satellite image products. The surface reflectance has direct relationship with increasing concentration of suspended solids at a given particle size. However, it responses inversely with decreasing particle size of suspended sediments (Bhargava & Mariam, 1991). It will be noticeable that turbid rivers that come from mining activities can generate surface reflectance slightly higher than those obtained at same measurement level, but from other land use (e.g. eroded topsoil particles from cultivated areas).

The succeeding chapters characterise each of the rivers and sub-drainage basin that have available water quality data, which were used to generate a regression model of the catchment. Moreover, ground truth data on the possible locations of small-scale mines were used as patterns to recognise their equivalent attributes using satellite image products, which were used to develop a training data for satellite image analysis.

Chapter 3 Characterisation of the catchment and surface water quality

This chapter examines the physical attributes of surface water in the Didipio catchment, and geomorphological characteristics and other spatial factors that can influence the sediment yield of each sub-drainage basin.

In 2013, OceanaGold established the acquisition of water samples from eight monitoring stations distributed in the principal stream networks. These stream networks, aside from natural forests and grassland, are mainly surrounded by open lands, cultivated areas, residential houses, the open-pit mine and diffused concentrations of small-scale mines. Graphical methods, such as box and whiskers plots and line graphs can be utilised to illustrate the four-year (2013-2016) database of physical water quality parameters for each river. Furthermore, statistical methods such as multivariate analysis of variance (MANOVA) can be effective for analysis of environmental data (Vega et al., 1998; Eneji et al., 2012). This Chapter applies these methods to examine trends of total suspended solids (TSS) and turbidity in the catchment, and their relation with the available hydrological data.

Before describing the approach, it is useful to introduce the two main water quality parameters that will be analysed.

- **Total suspended solids (TSS)**

Suspended solids are identified as water pollutants, and are measured in a mass per volume basis known as total suspended solids (mgL^{-1}). The variation in TSS over time highly depends on water flowrate and soil texture. In summer, rivers have limited water flow thus allowing suspended solids as large as sand to settle throughout the water column (Fondriest, 2016). Settled solids further block water flow and limit solar radiation for microorganisms (Davis & McCuen, 2005). In contrast, TSS measurement increases in the presence of storm water runoff (Sosiak, 2001). Moreover, soil texture determines the retention time of suspended solids. Soil texture defines the sand, silt and clay compositions of various forms of soil (Yong et al., 2012). Minerals are deposited in the subsoil layer where silt and clay are extremely abundant. If the subsoil layer is exposed, silt and clay from river banks are easily eroded by running water due to their smaller particle sizes (silt: 0.002 to 0.06 mm; clay: <0.002 mm) compared with sand and gravel (sand: 0.06 to 2 mm; gravel: >2 mm) (Tindall & Kunkel, 2009; Yong et al., 2012). On the other hand, silt and clay have longer retention time during suspension on water. Once settled on river bottom, they are compacted

into aggregates, and are resuspended only during storm water runoff (Russian Global Lab Project, 2008).

- **Turbidity**

Turbidity is a measure of how suspended particles influence the clarity of water, and it is often measured in Nephelometric Turbidity Units (NTU) (Stone et al., 2016). It is also used as indicator of TSS and degree of erosion (Davis & McCuen, 2005). Increase in turbidity can increase water temperature as it absorbs more radiance from the sun and a warmer water tends to hold lesser amount of dissolved oxygen (DO) (Davis & McCuen, 2005; Fondriest, 2016).

3.1 Research approach

3.1.1 Acquisition of surface water quality data

In 2013, OceanaGold commenced collecting water samples from river tributaries that have been heavily impacted by turbidity. Originally, eight monitoring stations were assigned for five rivers. Out of the eight stations, six (station codes DP-DOWN, SWS-12, SWS-13, SWS-14, SWS-15, SWS-17) were located near small-scale mines, one (code DP-UP) was next to open-pit mine, and another (code SWS-16) was in the Surong River (Figure 3-1).

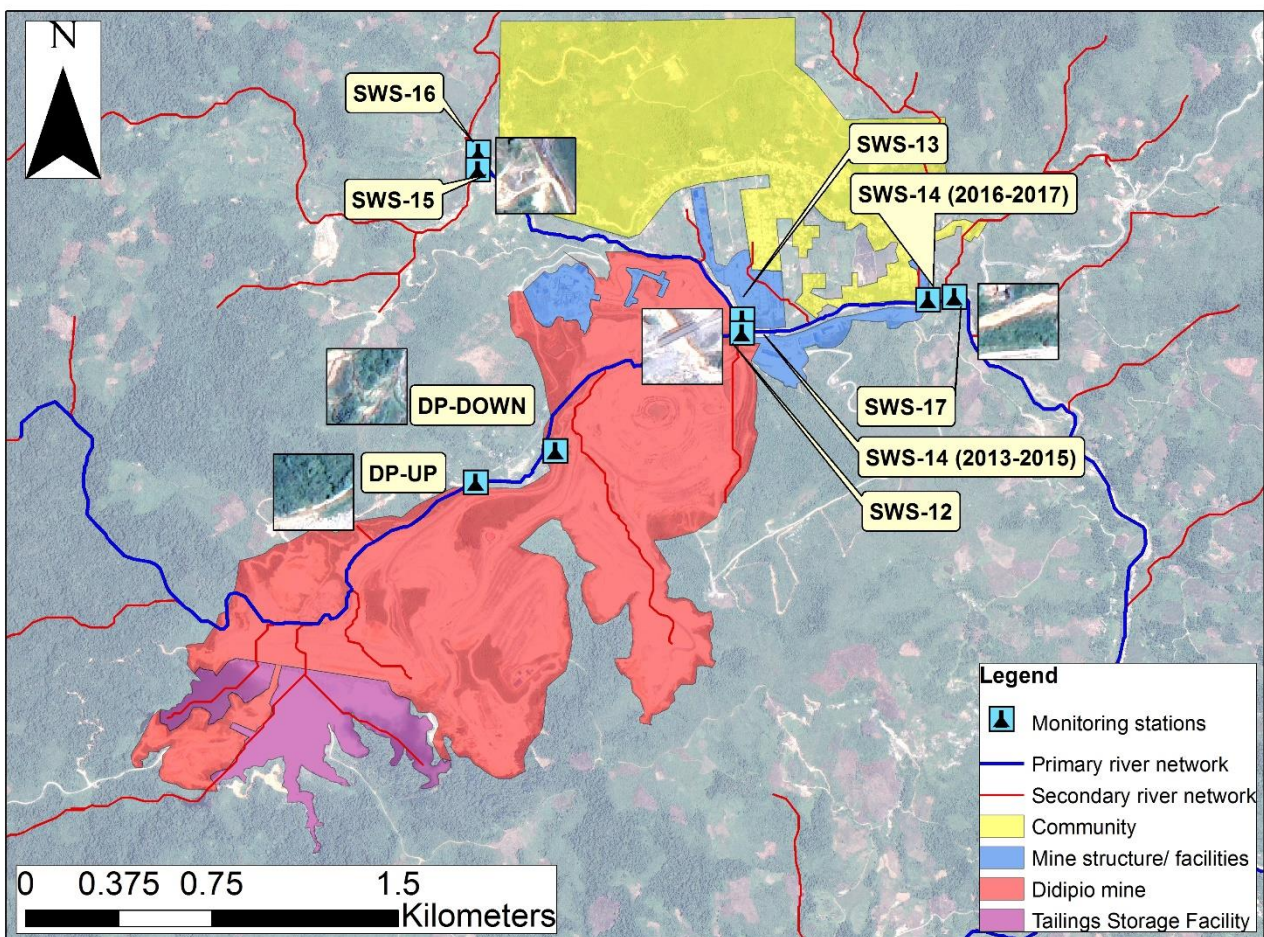


Figure 3-1: Location of river monitoring stations

Note. Adapted from OceanaGold Didipio Project, Environment Department database
Pleiades: © CNES (2013), Distribution Airbus DS / Spot Image

The database of total suspended solids and turbidity from 2013 to 2016 was used as the reference for this research (Table 3-1). Some stations, such as SWS-15 and SWS-16, were less frequently sampled due to access security issues.

Table 3-1: Database of surface water quality parameters from 2013 to 2016

Monitoring station	Northing	Easting	Location of station	Frequency of sampling (days in a year)			
				2013	2014	2015	2016
DP-UP	333,933	1,805,408	Dumulag Property Downstream	334	365	345	365
DP-Down	334,270	1,805,607	Dumulag Property Upstream	305	365	343	365
SWS-15	333,998	1,806,696	Camgat River Upstream	0	16	46	28
SWS-16	333,999	1,806,767	Surong River Upstream	0	19	47	28
SWS-12	335,038	1,806,039	Dinauyan Downstream	302	365	344	365
SWS-13	335,041	1,806,099	Camgat-Surong River Downstream	302	350	344	365
SWS-14 (2013-2015)	335,072	1,806,049	Didipio River Downstream	300	365	0	0
SWS-14 (2016-2017)	335,811	1,806,173	Didipio River Downstream	0	0	344	365
SWS-17	335,953	1,806,177	Didipio River Downstream	0	31	31	364

Note. Adapted from OceanaGold Didipio Project, Environment Department database

3.1.2 Method of surface water quality sampling

The river sampling was performed by OceanaGold's Department of Environment. A standard procedure was formulated to protect samples against any form of contamination. An amber bottle with a volume capacity of at least 300 ml was used as the sample container. The amber bottle, aside from being inexpensive, protects the sample's constituents against UV rays of the sun, and produces no chemicals that might react with the sample. Furthermore, the sampler used sterilised gloves during sample collection. The sampler submerged the amber bottle in the opposite direction to the river current, and collected the water discharge at 2.5 cm below the water surface. The sample collection was made daily for six monitoring stations located downstream and once a week for the two upstream monitoring stations in the Camgat and Surong Rivers.

3.1.3 Laboratory and in-situ analyses of surface water quality data

Two techniques were performed by OceanaGold to test turbidity and TSS, separately. Firstly, the test for TSS was carried out in a laboratory. Soil grains were filtered, dehydrated and weighed for each of the water sample. Prior to actual measurement, a filter paper was preheated in an oven for an hour at 103 °C to remove the moisture. The residual moisture was further removed by transferring the filter paper into a dessicator until its weight stabilised. A graduated cylinder and Bucher flask were prepared and cleansed with 100 ml distilled water. The test for TSS was performed by pouring 100 ml of the water sample into the graduated cylinder and then filtered through the flask, which is connected to a vacuum pump. The vacuum pump assisted in isolating the water from the soil grains. The filter paper together with wet soil grains were heated until the moisture was completely removed. The TSS was measured by subtracting the filter's dry weight from the weight of dry soil grains and then divided by the volume of the source water sample.

On the other hand, a multi-parameter probe (Horiba U-5000 Model) was used to determine in-situ turbidity and other water quality parameters like dissolved oxygen, electrical conductivity and pH. For probe calibration, a 400 mgL^{-1} of formazin or kaolin standard solution was poured in a clean container followed by immersing the probe sensor to standardise turbidity reading at zero NTU (Horiba, Ltd., 2009). The probe or tester was submerged into the river. The step was repeatedly done three times and for each trial, the sampling probe was cleansed with deionised water to remove any contaminants that might influence the reading. For each parameter, the three measurements were averaged for the final reporting of values. Out of these parameters, only the turbidity data will be presented in the thesis.

3.1.4 Measurement for flow rate

In 2013 and 2014, the flow rate measurements at stations SWS-12, SWS-13 and SWS-14 were obtained with frequency similar to water sample acquisition (Table 3-1). During the test, the cross-section of river being examined was imaginarily divided into series of segments of maximum size of 1 m x 1 m. For each segment, the sampler measured the river depth by dipping a measuring pole into the river to determine if the water level is within or below 30 cm deep. The flow rate is measured by submerging an impeller-type flow meter (Current Meter Counter Model CMC20A) into the river for twenty seconds in the opposite direction of the river current.

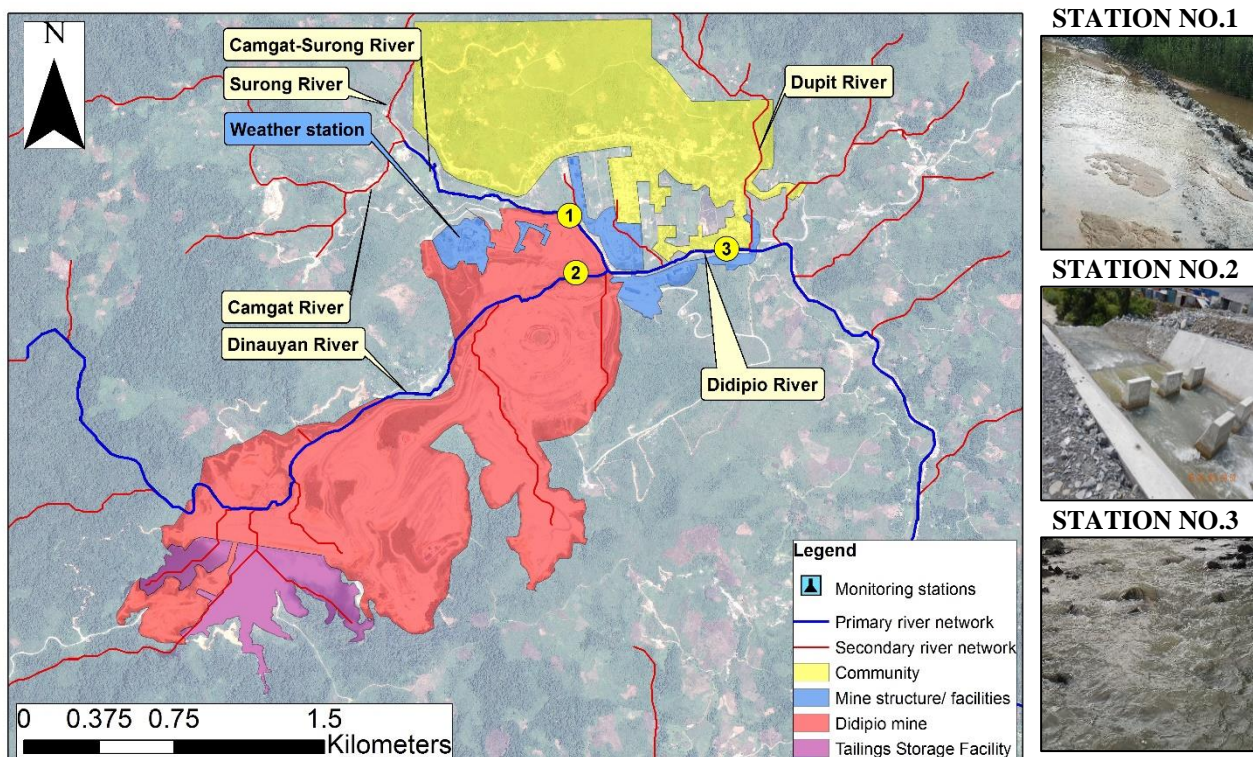


Figure 3-2: Measurement of flow rates at each monitoring station located downstream of primary river tributaries

(a) Station 1: Camgat-Surong River; (b) Station 2: Dinauyan River; (c) Station 3: Didipio River
Pleiades: © CNES (2013), Distribution Airbus DS / Spot Image

3.1.5 Rainfall and weather data

Daily rainfall data were secured by OceanaGold using an automated weather station (Davis Vantage Pro2 model). The weather station is placed on top of a mine structure at the highest ground elevation of Didipio mine (Figure 3-2). In addition to rainfall data, environmental temperature, atmospheric pressure, percentage humidity, wind speed and direction, were also measured.

3.1.6 Application of a Digital Elevation Model (DEM)

A five-metre spatial resolution Digital Elevation Model (DEM) provided by the National Mapping and Resource Information Authority (NAMRIA) in the Philippines, was used to determine the mean slope (geometric characteristics) of sub-drainage basins and their respective spatial distribution through the spatial analyst tool of ArcGIS®. The DEM is a derivative product of an Interferometric Synthetic Aperture Radar (IFSAR) image. Furthermore, the hypsometric curve of each sub-drainage basin was generated from the DEM. According to an article (Perez-Pena et al., 2009), the hypsometric curve is the plot of relative proportion of the area against its given altitude in a basin. The principle of hypsometric curve was used to determine the dominant lithological movement present in each sub-drainage that induces sediment production contributing to high suspended sediments. It was used in the study to assist in selecting the topographic factors that are significant predictors of suspended solids. The hypsometric curve as shown in Figure 3-3 presents the probable age of a basin through a graph. Its age explains the dominant lithological process that determines its configuration. A young sub-drainage basin, which has an index higher than 0.50 (e.g. area below the curve), is governed by diffusive hillslope processes. On the other hand, an old sub-drainage basin is regulated by alluvial processes where most of the soil and rocks have already been transported downstream.

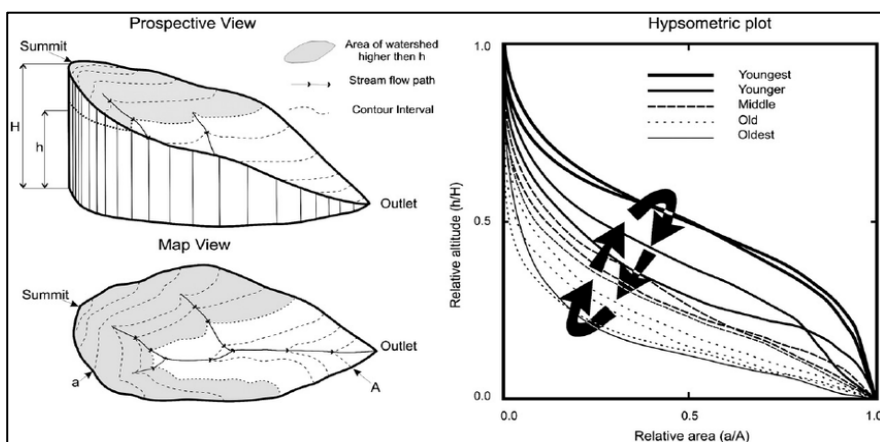


Figure 3-3: Calculation of the hypsometric curve using a Digital Elevation Model (DEM)

Adapted from “TecDEM: A MATLAB based toolbox for tectonic geomorphology, Part 2: Surface dynamics and basin analysis”, by F. Shahzad and R. Gloaguen, 2011, *Computers & Geosciences*, 37(2), p. 266. Adapted with permission.

3.1.7 Application of an optical image product

In this research, a WorldView-2 scene of Didipio catchment, which was captured in 18 September 2010 was used to illustrate the initial environmental condition of Didipio catchment seven years ago. The multispectral image and panchromatic band of the said image was orthorectified. Thirty ground control points (GCP) based on a reference map, were used during the application of the Rational

Polynomial Coefficients (RPCs). Each image scene has unique RPCs, which provide a mathematical model that associates the GCPs with a two-dimensional map (Al-Fares, 2013). On the other hand, ground elevations for each GCP were acquired through a 30-metre Shuttle Radar Topography Mission (SRTM) DEM. In addition to this procedure, tie points in reference to an orthorectified satellite image were added as x and y control points in correcting the WorldView-2. The resulting root-mean-square errors (RMSEs) for the multispectral and panchromatic images were 33 m and 4.5 m, respectively. The orthorectification process was followed by geo-referencing, where the WorldView-2 image was projected to a Universal Transverse Mercator (UTM) at Zone 51 North.

3.2 Results and discussion

3.2.1 Physical attributes of the rivers

3.2.1.1 Comparison of flow rates among the rivers

Using the flow rate data collected between 2013 and 2014 for the Camgat, Dinauyan and Didipio rivers, the relationship between flow rate and TSS was analysed. Figure 3-4 shows how the mean flow rates fluctuated both in the dry and wet seasons. The catchment still receives an enormous amount of rainfall, as much as 300 mm, during dry season. The lowest recorded monthly rainfall was 42 mm in March 2015 while the highest in the four-year period from 2013 to 2016 was 976 mm in October 2015.

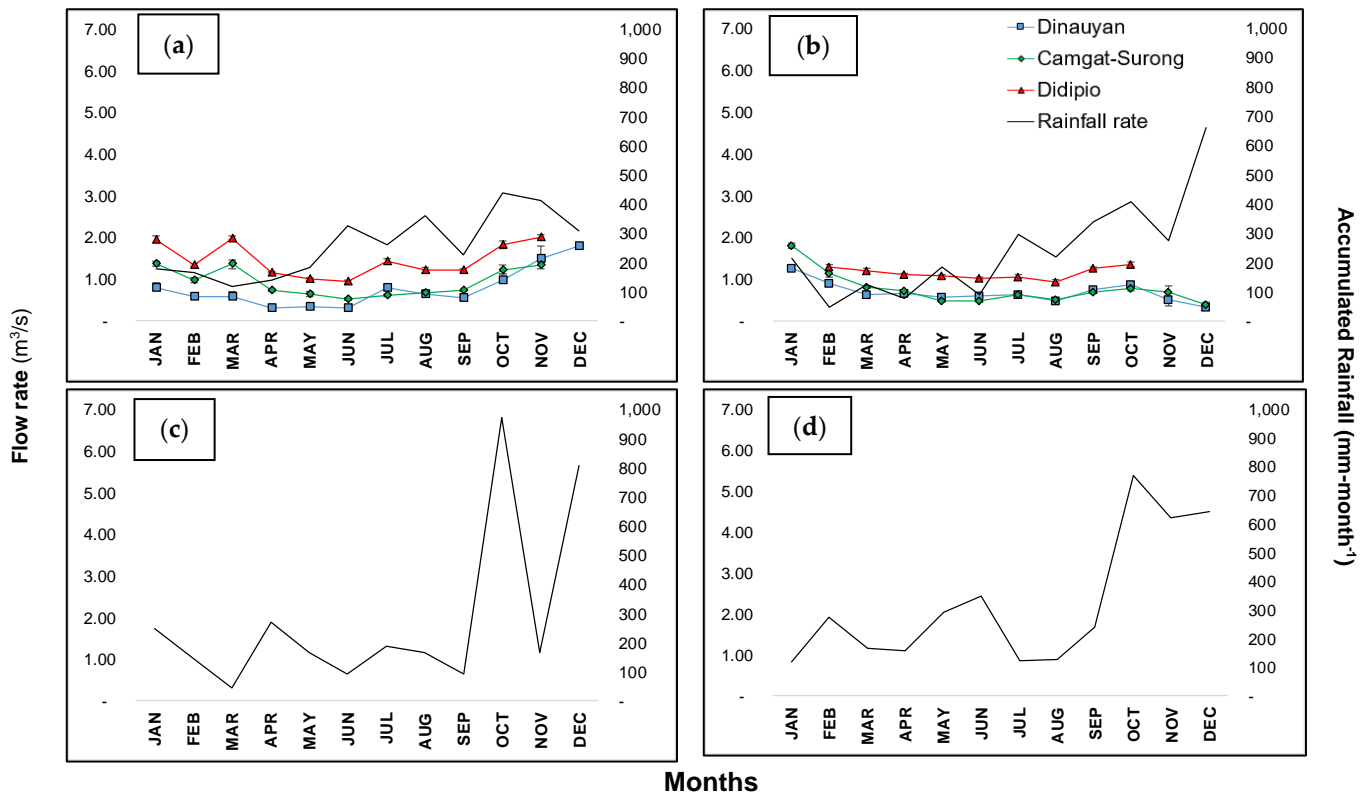


Figure 3-4: Four-year rainfall data of the Didipio catchment area with recorded water flow rates in 2013 and 2014

(a) 2013; (b) 2014; (c) 2015; (d) 2016

The Didipio catchment has an erratic weather pattern, which was confirmed by the four-year rainfall data, although it has a relatively high monthly rainfall in the period between October and December (Figure 3-4). Based on the results of this case study, neither flow rate nor rainfall were significant contributors to TSS, based on the low coefficient of determination (R^2) and high p-value.

3.2.1.2 Statistical characteristics of each river

The statistics of the four-year data of total suspended solids (2013-2016) that had been provided by OceanaGold were used to illustrate each river (Table 3-2). In general, the entire catchment exhibits highly turbid water, and TSS can rise as high as $32,000 \text{ mgL}^{-1}$. The Dinauyan, Dupit and Surong rivers are among the rivers that display consistent median readings of TSS (Figure 3-5). Likewise, these rivers have the lowest mean TSS values. However, the Dinauyan River is associated with a considerable number of extreme TSS readings. It also has the highest TSS reading, which was recorded in 2014. Furthermore, the Camgat River has been regularly generating elevated TSS measurements since 2014, the year when water quality data for this river first became available. Its mean TSS of $4,251 \text{ mgL}^{-1}$ is far greater when compared with the other rivers. In addition, the Camgat River has a wide range of non-outlier TSS readings at the lower 75% percentile of its database (Figure

3-5). These variable TSS readings indicate erosion of the river banks or soil in areas that are hydrologically connected to the river, potentially due to intensive land use. The Camgat-Surong and Didipio rivers also displayed elevated mean TSS values, but more consistent median readings of TSS.

Table 3-2: Statistics of TSS of the 6 principal rivers (2013-2016)

River	Stations	Min	Max	Mean	Std. Error
		mgL^{-1}	mgL^{-1}	mgL^{-1}	mgL^{-1}
Dinauyan	DP-UP, DP-DOWN, SWS-12	0	32,060	239	15
Camgat-Surong	SWS-13	0	17,370	1,098	33
Didipio	SWS-14	7	11,357	736	23
Surong	SWS-16	0	4,555	97	49
Camgat	SWS-15	20	23,366	4,251	578
Dupit	SWS-17	0	10,417	392	33

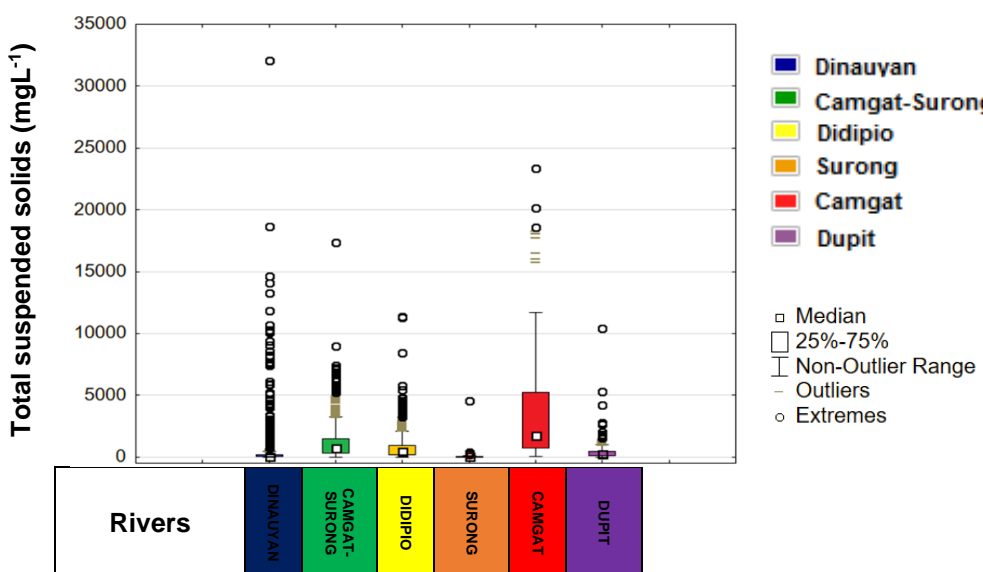


Figure 3-5: Box and whiskers plots of TSS

3.2.1.3 Relationship between TSS and turbidity

The Horiba U-5000 multi-parameter probe has a turbidity upper detection limit of 999 NTU. This constrained the derivation of a statistical relationship between TSS and turbidity. In addition, potential outliers were omitted from the dataset. For this dataset, TSS and turbidity values ranged from 0-1,339 mgL^{-1} and 0-997 NTU.

The plots of TSS versus turbidity present a linear relationship (Figure 3-6). With the exception of DP-UP, SWS-12 and SWS-16, the least-squares linear regression (forced to pass through the origin) gives a near 1:1 gradient. In general, the linear relationships have a coefficient of determination (R^2) of above 50% (Table 3-3). Clearer water that flows to the DP-UP, SWS-12 and SWS-16 stations leads

to a lower slope coefficient (m) (Table 3-3), in other words, TSS values at these stations increase relatively little for every unit increase in turbidity. This illustrates how turbidity reading at lower values of TSS can be affected by the particle size distribution. Sand-size particles, which settle on river bottom are more dominant over these rivers compared with the silt and clays that are produced from small-scale mines. On the other hand, the presence of soil particles in various sizes (sand, silt and clay) produces inconsistent scattering of light, which affects turbidity reading (Rugner et al., 2013). This presents why the impact of rainfall to increasing flow rate is not completely captured in the database of TSS and turbidity.

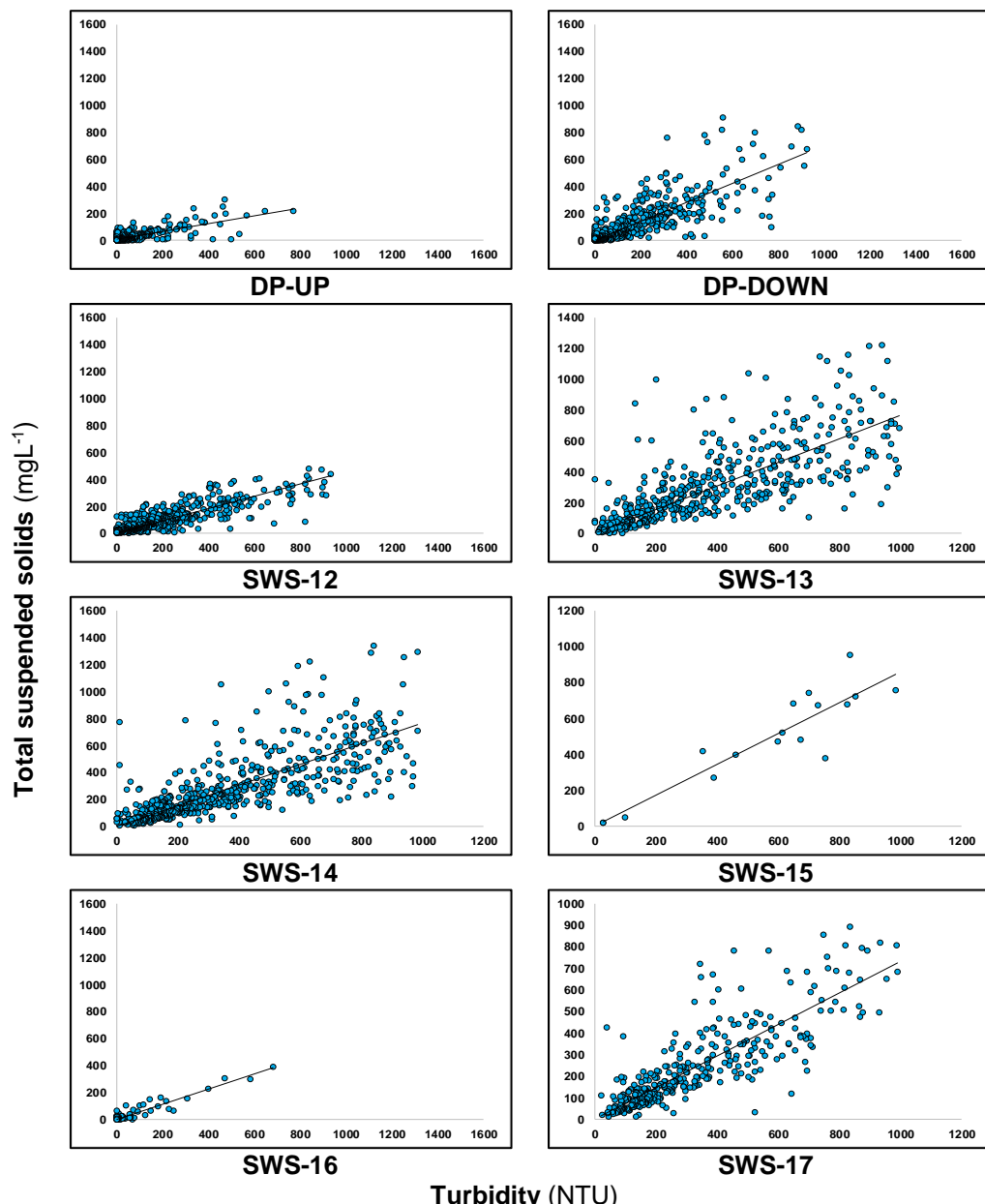


Figure 3-6: Graphs of TSS versus turbidity in each monitoring station

Table 3-3: Relationship of TSS and turbidity for each river

Stations	Sample size	Equation	Coefficient of determination (R^2)
			n
DP-UP	662	$y = 0.2896x + 7.4998$	59
DP-DOWN	638	$y = 0.7041x$	65
SWS-12	757	$y = 0.4556x$	70
SWS-13	485	$y = 0.7673x$	52
SWS-14	610	$y = 0.7691x$	58
SWS-15	17	$y = 0.8611x$	83
SWS-16	64	$y = 0.5636x$	88
SWS-17	348	$y = 0.7314x$	69

Overall, 3,582 samples were compiled to establish a general equation for the catchment. The TSS versus turbidity plot is best defined by an equation with slope (m) coefficient of 0.71 mgL^{-1} - NTU^{-1} at an R^2 of 68%.

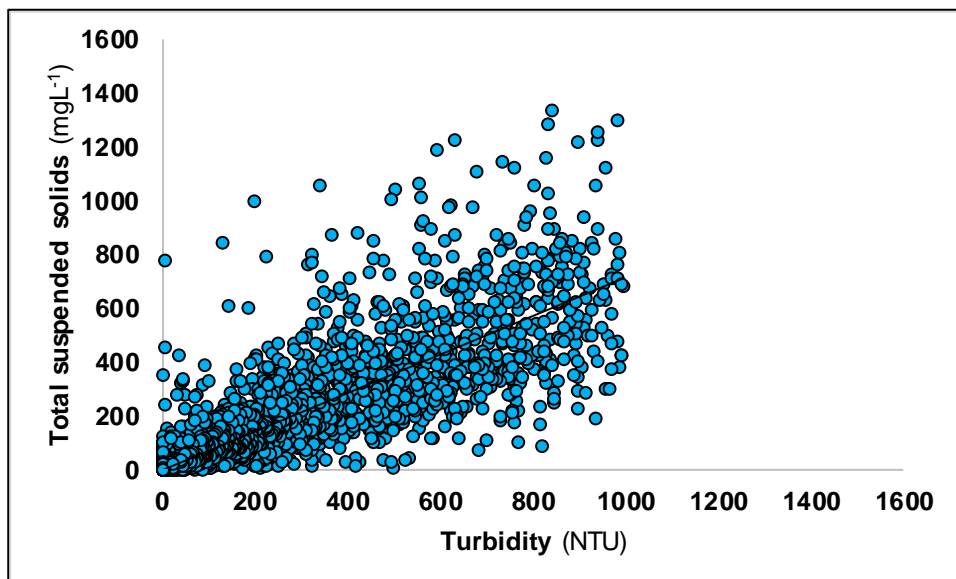


Figure 3-7: Linear relationship between TSS and turbidity in the Didipio catchment

3.2.2 Geometric characteristics of the sub-drainage basins

3.2.2.1 Topography of the rivers

The sediment yield of a catchment is primarily regulated by a number of factors related to deposition and erosion (Verstraeten & Poesen, 2001). Soil erosion is induced by climate, level of vegetation cover and topography. Sediment deposition is influenced by catchment morphology, drainage network and type of land use (Tamene et al., 2006; Verstraeten & Poesen, 2001). Based on the average slope of each of the sub-drainage basins, the Camgat, with a mean altitude of 897 m has the steepest basin. It has a mean slope of 21.62 degrees (Table 3-4). The Surong basin, also with a high mean

altitude of 889 m, has a mean slope of 18.72^0 . At the middle level of the catchment, the Camgat-Surong and Dinauyan basins have a mean altitude of 763 m. In general, the Camgat-Surong basin has a gentle topography since it is surrounded by paved areas, including a local community to the north, and an open-pit mine to the south. On the other hand, the mean slopes of the Didipio and Dupit basins are moderate at 16.50^0 and 16.25^0 , respectively. Rivers with high readings of TSS and turbidity (e.g. Camgat, Camgat-Surong, Didipio and Dupit) were mostly surrounded by gold panning activities along the riverbanks. Figure 3-13 presents how gold panning altered the configuration of Didipio River since 2010. Secondary forms of land use above an altitude of 789 m altitude in the north (e.g. cultivated areas) have a minimal impact. Among the sub-drainage basins, the Camgat, Surong and Dupit basins have the least variation in slope, as reflected from the computed standard deviations.

Table 3-4: Descriptive statistics of the catchment slopes

Basin	Slope (degrees)			
	Min	Max	Mean	Standard deviation (σ)
Camgat	7.95	52.07	21.62	7.95
Surong	6.60	55.64	18.72	7.81
Camgat-Surong	1.84	57.89	12.94	8.28
Dinauyan	6.92	57.89	17.54	9.27
Didipio	1.12	50.24	16.50	8.91
Dupit	6.30	46.36	16.25	6.92

From a spatial perspective, the slope map shows that the steepest regions of the river basins are mostly forested areas (Appendix B). In the remotely sensed image, they are found the highest elevations in the Camgat and Surong basins, to the north and south of the upstream part of the Dinauyan River and northeast of the Didipio basin. In contrast, gentlest sloping land can be observed along the open-pit mine and cultivated areas surrounding the downstream part of the Surong River. The identified locations of small-scale mines in the Camgat and Camgat-Surong basins have slopes ranging from 30^0 to 40^0 . Figure 3-8 presents the concentrations of the small-scale mines relative to the sub-drainage basins.

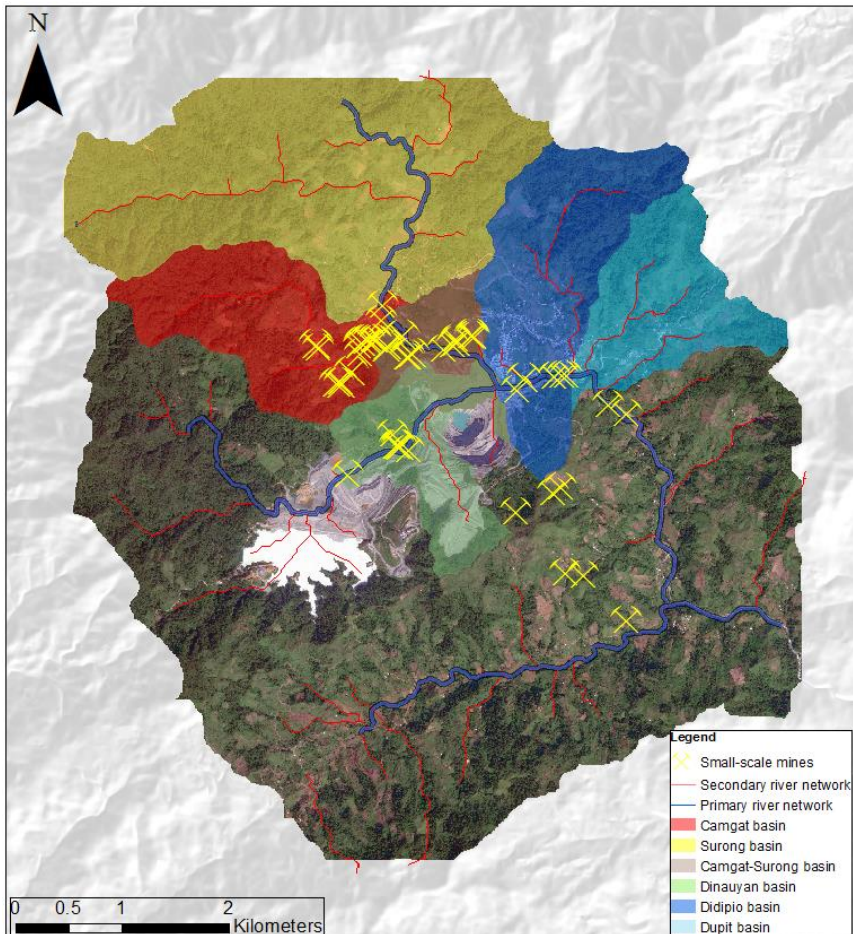


Figure 3-8: Delineation of sub-drainage basins in the catchment area
SPOT: © AIRBUS DS (2016)

In addition, the channel slopes were also measured (Appendix C). Within the catchment, Camgat is the steepest at 7.56° . It is followed by the Surong and Dupit channels with mean slopes of 7.14° and 6.90° , respectively, while Camgat-Surong, Dinauyan and Didipio channels have moderate mean slopes. From the computed statistics, the Camgat, Surong and Dupit channels have relatively higher standard deviations. These values determine the variability of the slopes along the channels, and can indicate the presence of rocky formations of the river beds on the upstream of these channels. Based on the slope graph (Appendix B), the segments of the Camgat and Surong channels at 750 m and 1,000 m, respectively, have more regular slopes. At these river segments, alluvial deposition is highly possible.

Table 3-5: Descriptive statistics of the channel slopes

Channel	Slope (degrees)			
	Min	Max	Mean	Standard deviation (σ)
Camgat	0.87	22.11	7.56	4.14
Surong	0.78	26.60	7.14	4.44
Camgat-Surong	0.62	22.87	4.86	3.13
Dinauyan	0.50	8.78	3.74	1.68
Didipio	1.00	9.30	4.17	2.00
Dupit	1.03	20.89	6.90	4.46

The gold mining near the Camgat River can also produce channel bars to downstream (e.g. Camgat-Surong River). These channel bars can be composed of dense sand-size soil particles that are deposited by the flow of water over time. During the period when the flow rate is high, part of the channel bar is washed out, contributing to the increasing water turbidity readings thus affecting the volume consistency of river discharge (Smith, 1989; Yuill et al., 2015; Wang et al., 2016). In 2014, a channel bar was formed in between the Camgat-Surong River as shown in Figure 3-9.



Figure 3-9. Formation of a channel bar in Camgat-Surong River

2010 Satellite Image courtesy of the [DigitalGlobe Foundation](#); Pleiades: © CNES (2013, 2014), Distribution Airbus DS / Spot Image; SPOT: © AIRBUS DS (2016)

3.2.2.2 Dominant lithological movement in each sub-drainage basin

Hypsometric curves were derived for each sub-drainage basin. Based on Figure 3-10, Didipio and Dinauyan are the older basin, as indicated by their concave curves. At these rivers, it can be said that the alluvial processes are more dominant, while associated rocks appear to be more rounded and less significant in scale. In addition, the presence of a valley bottom is noticeable for these rivers. Valley bottoms can catch sediments and prevent high river turbidity. However, this may not be the case for the Didipio River, which serves as receiver of water from upstream channels. Its threshold capacity to carry sediments at a regular flow rate may not be enough to accept additional sediments.

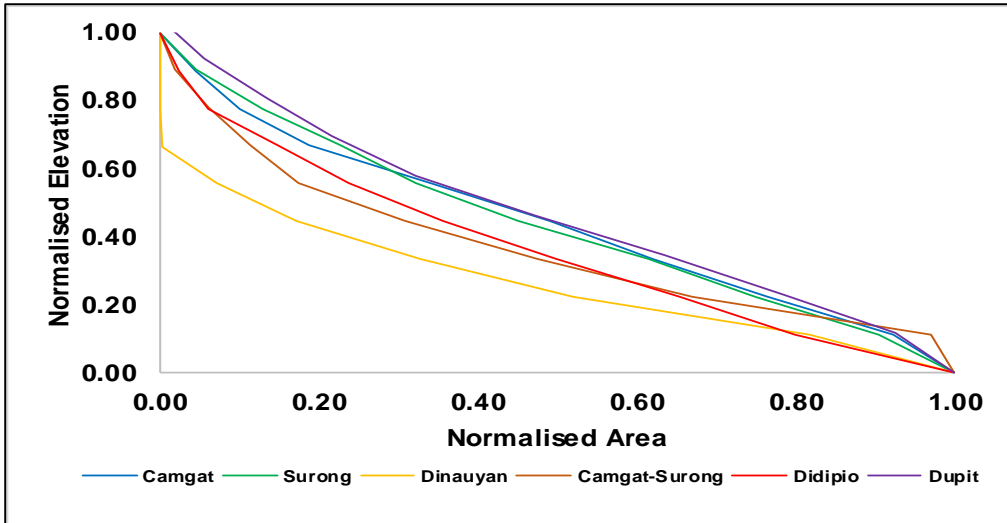


Figure 3-10: Graph of hypsometric curves for each river

Furthermore, the Camgat-Surong basin is currently in a state of equilibrium, based on the pattern of its plot (s-curve) (Figure 3-11). In contrast, the Camgat, Surong and Dupit basins are not yet heavily impacted by alluvial processes (convex curves). Steeper topography can be observed at these basins where water hardly penetrate the ground; therefore, increasing the potential runoffs toward the rivers. Moreover, sediment movement in these basins can be initiated by their slope.

3.2.2.3 Potential contribution of land use and topography to increasing suspended solids

The Camgat, Dupit and Surong sub-drainage basins, although having comparable topography, illustrated the potential role of land use in delivering sediments to rivers. The Dupit and Surong rivers are principally used for irrigation system, whereas the Camgat River is associated with a major concentration of small-scale mines that use both rudimentary methods and mechanical equipment. The two rivers have been associated with differences in water quality, the Camgat River being highly turbid whilst Surong River has consistently provided clear water. It can be said that these three sub-drainage basins can receive equivalent level of impact from a single type of land use. The Camgat River being turbid compared with Dupit and Surong illustrates how ASM greater contributes to increasing concentration of suspended sediments over steep topography. Moreover, Surong and Didipio are the biggest sub-drainage basins in the catchment (Table 3-6). Yet, their water qualities are better than that of the Camgat basin. It can be concluded that land use principally determines the turbidity variation in Didipio catchment. Whereas the geometry of sub-drainage basins augments the land use impact to increasing turbidity.

Table 3-6: Surface area of each sub-drainage basin

Sub-drainage basin	Area (km ²)
Camgat	2.52
Surong	7.03
Dinauyan	1.71
Camgat-Surong	1.03
Didipio	3.07
Dupit	2.01

3.2.2.4 Environmental baselining of the catchments

The WorldView-2 image of Didipio catchment reveals that the location of current Didipio mine was a concentration of small-scale mines. Through manual delineation, an estimated 66,676 m² was associated with small-scale mining in 2010 (Figure 3-11).

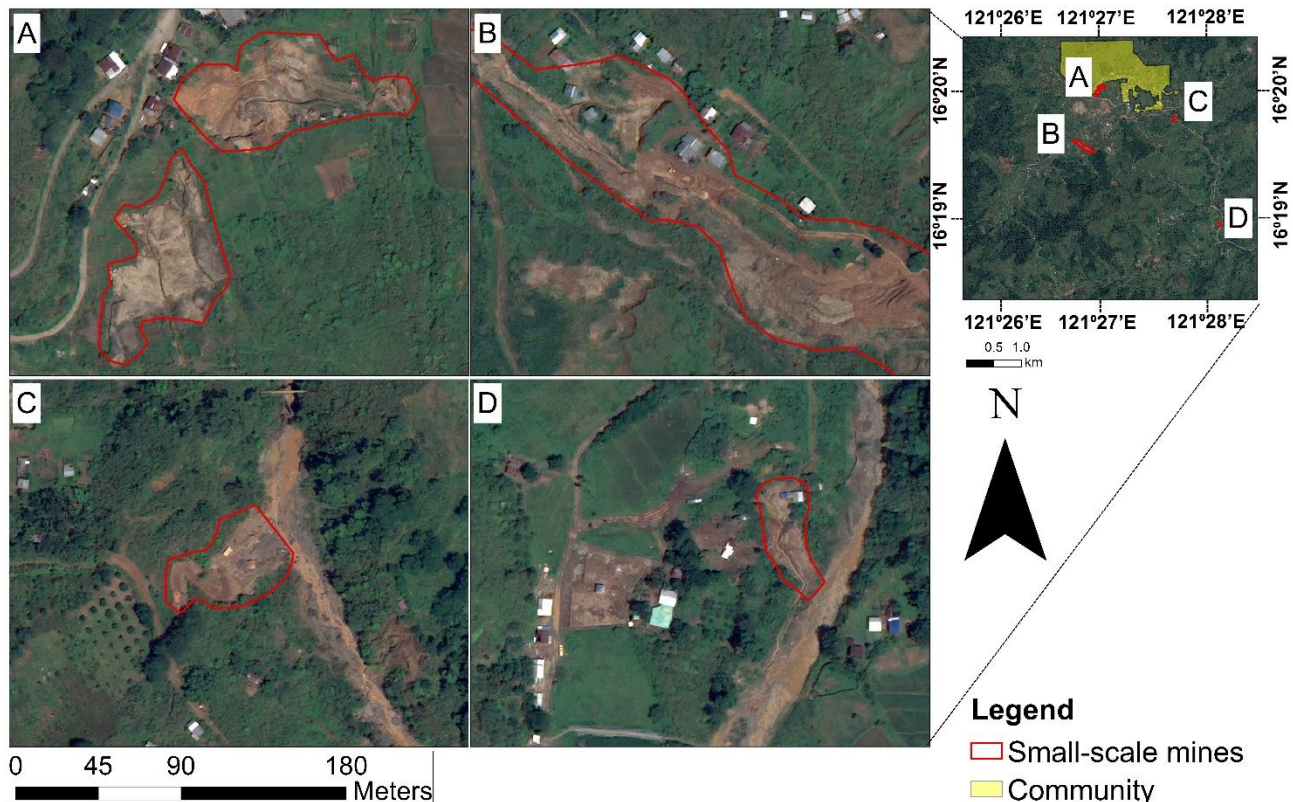


Figure 3-11: Existence of small-scale mines in 2010, prior the construction of open-pit mine
 (a) Hydraulic mines south of the local community; (b) Potential hydraulic mines over the current location of Didipio mine; (c) Gold panning site at lower Didipio River; (d) Panning site near the lower Didipio River, which forms confluence with Alimit River
 2010 Satellite Image courtesy of the [DigitalGlobe Foundation](#)

In 2010, the small-scale mines were already impacting on the small creeks of Buya and Magastino that are linked to Dinauyan River. Spectral signatures of creeks and rivers adjacent to these mines were acquired. The results present the spectral signature of highly turbid water (Figure 3-12).

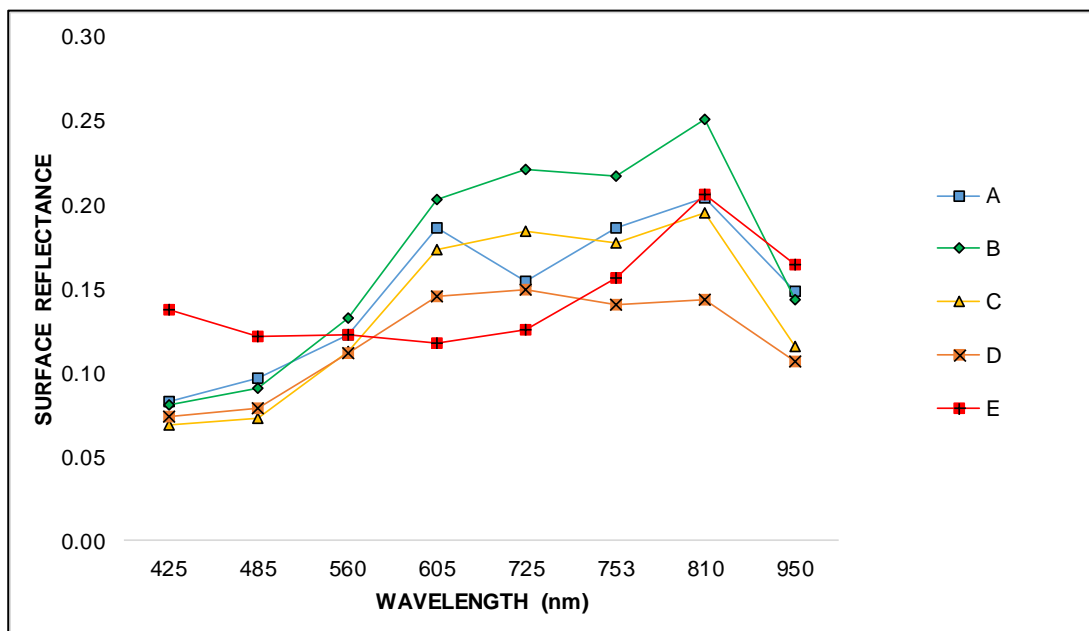


Figure 3-12: Plot of surface reflectance for the impacted river segments by activities of small-scale mines (A-D)

(a) Plot A-D for highly turbid water; (b) Plot E corresponds to a clear water

3.2.3 Temporal variations in TSS

Figure 3-14 presents the temporal changes in TSS measurements of each monitoring station from 2013 to 2016. The yearly coverage of each plot depends on the availability of TSS data, and their yearly mean TSS was used to characterise the dynamics of small-scale mining throughout the years. Between 2013 and 2014, DP-UP and SWS-14 were the stations associated with the greatest improvements. There is a noticeable decrease in measured mean TSS by an amount of 191 and 187 mgL⁻¹, respectively. The annual mean TSS decrease for the remaining stations, except for SWS-15 due to absence of data, ranged from 100 to 156 mgL⁻¹. This improvement in the TSS measurement is an indication of the diminishing scale of activities from small-scale mines. Between 2014 and 2015, DP-DOWN, SWS-13 and SWS-14 had the greatest positive development with annual mean TSS decreases of 290, 269 and 397 mgL⁻¹, respectively. It is possible that as Didipio mine expands its scope, the miners who performed gold panning near the Dinauyan and upper Didipio rivers had been dispersed, and moved to alternative sites where their activities are less observable by authorities. Gold panning had been evident in the upper Didipio, and was replaced by a small-scale mine in 2014 (Figure 3-13). Meanwhile, the Surong catchment experienced a similar case, with a decrease of 235

mgL^{-1} in measured annual TSS, suggesting small-scale mining within the residential areas. However, its confluence with the Camgat River was clearly active, with SWS-15 and SWS-17 almost maintaining their previous values, although the data at SWS-17 was only sampled during the month of January and cannot be used as an indication of the general trend.

At the end of 2016, the Dinauyan River had a normalised annual mean TSS at 100 mgL^{-1} . Almost the same amount was observed within the extent of DP-DOWN to SWS-12. The Surong River had improved at 35 mgL^{-1} , SWS-13 and SWS-14 had a reduction of 250 and 300 mgL^{-1} , respectively. On the other hand, SWS-15 was still producing more sediments, with an annual mean TSS increase of 1870 mgL^{-1} . From 2013 to 2016, the greatest reduction of TSS were observed in SWS-14 followed by SWS-13 and DP-UP. The decrease in overall mean TSS readings were 798 , 707 and 519 mgL^{-1} , respectively.



Figure 3-13: Changes in the upper Didipio River over time

2010 Satellite Image courtesy of the [DigitalGlobe Foundation](#); Pleiades: © CNES (2013, 2014), Distribution Airbus DS / SPOT Image; SPOT: © AIRBUS DS (2016)

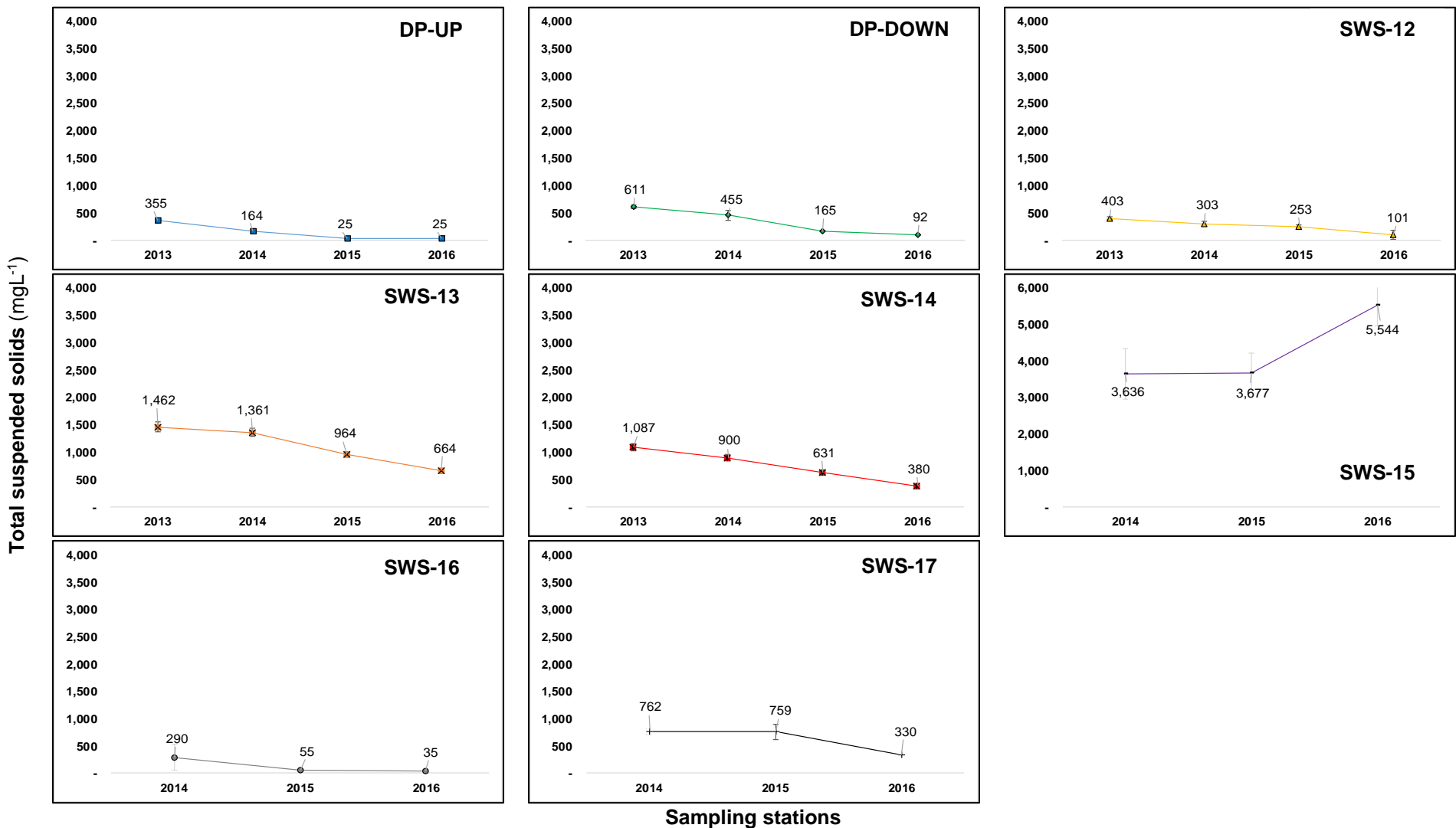


Figure 3-14: Temporal variation of total suspended solids from 2013 to 2016

3.3 Summary

In this chapter, the principal rivers in the Didipio catchment were illustrated in the context of their TSS and turbidity data collected from eight monitoring stations over four years, 2013-2016. Among the rivers, the Camgat River was contaminated with suspended solids which were generated from active small-scale mines. The degree of the industry's impact was explained by two important parameters: (i) the wide range of median values for TSS at higher measurement levels; and (ii) numerous outliers and extreme readings. In contrast, the Dinauyan, Dupit and Surong rivers were observed as having relatively low TSS medians and ranges.

Furthermore, the relationship between TSS and turbidity was explored. Based on results of regression analysis, a linear relationship exists between the two parameters although with a large error variance (Figure 3-6 and Figure 3-7). Also, it can be observed that the derived linear relationships are depended on the river: rivers with lower turbidity had lower slope coefficients in the equation.

On the other hand, the potential role of land use in delivering sediments to rivers was validated through the application of hypsometric curve. The hypsometric curve of each sub-drainage basin presents that land use type impacts to turbidity variation is more significant over the influence of spatial factors such as steep basin slopes and undeveloped topography. On the other hand, the hillslope, channel slope and other spatial factors intensify the contribution of land use to increasing suspended sediments in the rivers through gravity and surface runoff that increase the transport rate of sediments.

The temporal variation in TSS was also evaluated in the period between 2013 and 2016. In general, there was a decline in TSS in the Didipio catchment. Whereas a significant increase in the level of TSS in 2016 was observed in the Camgat River.

Chapter 4 Applicability of satellite imagery to identify small-scale mining footprints in a wet tropical region

Small-scale mines¹ can be major contributors to local economies and livelihoods (Labonne, 2002; Hilson, 2005), but in many cases, this comes with significant environmental impacts due to unsuitable locations, rudimentary mining methods and lack of effective regulations (Cordy et al., 2011; McIntyre et al., 2016). The diffuse and remote locations of the mine sites, and their relatively short and unpredictable life span, impede the systematic documentation of small-scale mine development and footprints (Telmer & Stapper, 2007). This is challenging for accurately surveying land use, accurate attribution of impacts and targeting of regulatory resources, hence regulating the development and operations of these mines is a considerable challenge.

The difficulty of effectively monitoring small-scale mining using traditional surveys calls for supplementary approaches based on remote sensing. The application of remote sensing from satellites, in conjunction with supervised techniques for classifying land use and land cover, is attractive for several well-established reasons. Remote sensing provides the opportunity to observe changes in land use and land cover over inaccessible regions. By combining images from different passes of one or more satellites, the evolution of land use and land cover can be modelled. For example, Landsat now provides 45 years of historical records from 1972 (Goward et al., 2001). Continual improvements in spatial, spectral, radiometric and temporal resolutions are permitting greater levels of information about the type, timing and extent of changes to be obtained. While moderate-resolution (10-100 m pixel size) satellite imageries can be accessed at no cost (e.g. Landsat), the availability of commercially provided high resolution (0.5-10 m pixel size) images is increasing and costs are decreasing.

Small-scale mining, however, introduces some challenges in applying remote sensing and associated land use classification techniques. The surface footprints for the smaller mines may only be tens of meters, and less for underground mines or mines in early stages of development, reducing the applicability of Landsat and other freely accessible products with moderate spatial resolutions. Another challenge is that the visible footprint of the mines - mainly vegetation and top-soil clearance –is similar to many other land cover and land use changes such as clearance for agriculture or forestry

¹ A small-scale mine is defined as a mine that operates using rudimentary mining and milling methods (minimal mechanisation and minimal or absence of structure that controls mine and mill spillages) at the level of individuals, families or cooperatives, and temporarily makes a specific mining claim or in other cases may be illegal. (Hentschel, Hruschka, & Priester, 2002; Sousa et al., 2011)

and is thus likely to have similar spectral responses. Moreover, mining areas can be confused with recently burned forest (Luethje et al., 2014). Finally, small-scale mining is a dynamic land use, and mines can be established and abandoned within a period of months; therefore, they may be difficult to capture with, bi-annual or annual images for example. These challenges are especially problematic in wet tropical regions, where cloud cover is likely to prevent the use of a large proportion of available images, and regular rainfall-driven land-slides may confound the identification of mines.

A key challenge for remote sensing of mining land cover is that several forms of land use have similar spectral signatures (Myint et al., 2011). Using pixel-based land cover classification approaches based on differences in spectral signatures can therefore result in misclassifications. This can be exacerbated if the distributions of reflectance for each class are not normally distributed (Huang et al., 2002). The limitations of pixel-based classification approaches have given rise to development of object-based segmentation techniques (Blaschke, 2010), which are collectively known as Geographic-object-based image analysis (GEOBIA) (Blaschke, 2010; Tzotsos & Argialas, 2008). Using GEOBIA, pixels with homogenous properties are merged to produce multiple segments (objects), where pixels are grouped based on, not only its spectral properties, but also the spatial and textural characteristics of the pixel segment to which it belongs (Tzotsos & Argialas, 2008).

A recent advancement in GEOBIA classification methods has been the application of Support Vector Machines (SVM) to image objects instead of pixels using a technique known as object-based support vector machine (OB-SVM) (Duro et al., 2012). Recent examples in the literature show that SVMs used with both pixels (Tzotsos & Argialas, 2008) and image objects (Duro et al., 2012; Lin et al., 2015) can outperform other classification algorithms (e.g., Decision Tree, Maximum Likelihood, Nearest Neighbor and Neural Networks). The SVM classifier is not based directly on differences between the statistical distribution of attributes of separate classes (Lin et al., 2015; Vapnik, 1998) but instead it uses non-parametric machine learning algorithms that determine the optimal boundaries among classes (Huang et al., 2002). The SVM classifier is noteworthy for its ability to separate complex classes with limited training data (Mountrakis et al., 2011). In addition, the overall accuracy of an OB-SVM can be improved by including other spatial data such as Digital Elevation Model (DEM) and Vegetation Indices (VI) (Duro et al., 2012).

The Support Vector Machine (SVM), is a set of machine learning algorithms that can be used for classifying remotely sensed data. Recent examples in the literature show that pixel-based (Tzotsos & Argialas, 2008) and GEOBIA (Duro et al., 2012; Lin et al., 2015) SVM can outperform other classification algorithms (e.g. Decision Tree, Maximum Likelihood, Nearest Neighbor and Neural

Networks). A binary SVM classifier as discussed by Lin et al. (2015) is not based directly on differences between the statistical distribution of attributes of two separate classes. Instead, it uses a hyperplane in virtual space, which determines the optimal boundary between two classes. On the other hand, the allotted allowance for misclassification of each class is called the optimal margin. It determines the support vector or the aggregation of class features to be used for training the sample data. In the application of an object-based (OB) SVM, the use of a kernel determines the optimal shape of a hyperplane thus controls the degree of misclassification or classification error. Known kernels being used are polynomial and radial basis functions (RBF) kernels, which perform well for classes that are nonlinearly separable (Huang et al., 2002). The kernel transforms each class into forms that make them linearly associated.

A binary SVM classifier can only provide a single hyperplane that separates two classes; therefore, an object-based SVM is an integration of binary SVM classifiers (Lin et al., 2015). For instance, if there are n identified classes in the image, there are $n(n-1)/2$ binary classifiers available for every pair of classes. The overall accuracy of an OB-SVM can be improved by increasing the input variables or raster data such as Digital Elevation Model (DEM) and Vegetation Indices (VI) maps in addition to spectral bands of the satellite image (Duro et al., 2012).

This research explores the applicability of remote sensing for capturing land use change dynamics in wet tropical regions subject to transient small-scale mining. The aims are to: 1) assess the required specifications (resolutions and spectral bands) of remotely-sensed images; 2) evaluate the data processing techniques that maximise the value of the images in terms of information extraction; and 3) for the case study area, to quantify and map land use change over recent years.

4.1 Research approach

4.1.1 Collection of ground truth data on the locations of small-scale mines

The Didipio catchment in Cagayan region is situated in the northeast of the Philippines. The anthropogenic land use features in this area include open land (deforested area), cultivated areas, small-scale gold mining and large-scale gold mining. Prior to this study, there was no publicly available documentation of land use in this region. Mining has become a principal land use since 2013, when operations started at the large-scale Didipio mine. This is composed of the open-pit mine and other mining structures such as haulage roads, stockpile areas and motor pool open wash bays with an estimated (January 2016) surface area of 2.23 km^2 (Figure 4-1). The mine expanded from

phase 1 to phase 2 during the period from 2012 to 2013. The area has seven principal rivers of interest here. The anthropogenic use of the Alimit, lower Didipio, Dupit and Surong rivers is primarily to support agriculture, whereas the Camgat, Camgat-Surong, Dinauyan and upper Didipio rivers are available for general community purposes, but are also the focus of small-scale mining activity.

On the other hand, availability of cloud-free satellite data is generally only possible in the dry season between January and April, although a high percentage of cloud cover persists for most of that period. Landsat-8 Operational Land Imager (OLI), a satellite with a 16-day acquisition frequency, was tested for cloud-free image availability of the catchment from 2013 to 2016. Over the four years, only five to eight of its images were suitable for image analysis, while only two full images of delineated Didipio catchment were unobstructed from atmospheric effects. The remainder of the images are contaminated either by clouds, haze or shadows.

Since 2012, the large-scale mine operator has kept a database of small-scale mine locations, based on ground surveys. Each site is labelled as an active or inactive mine. An inactive mine includes operational mines where there happened to be no activity on the day of survey, as well as seemingly abandoned mines. Supplementary information, such as the mining technique and/or presence of processing equipment and earth-moving vehicles has also been recorded. The surveys have been conducted every quarter of the year. This database was supplemented by ground surveys by the authors in November 2015 and February 2016. Figure 4-3 shows the evolution of the location and type of small-scale mines; and photographs for sample sites and corresponding descriptions are presented in Appendix D.

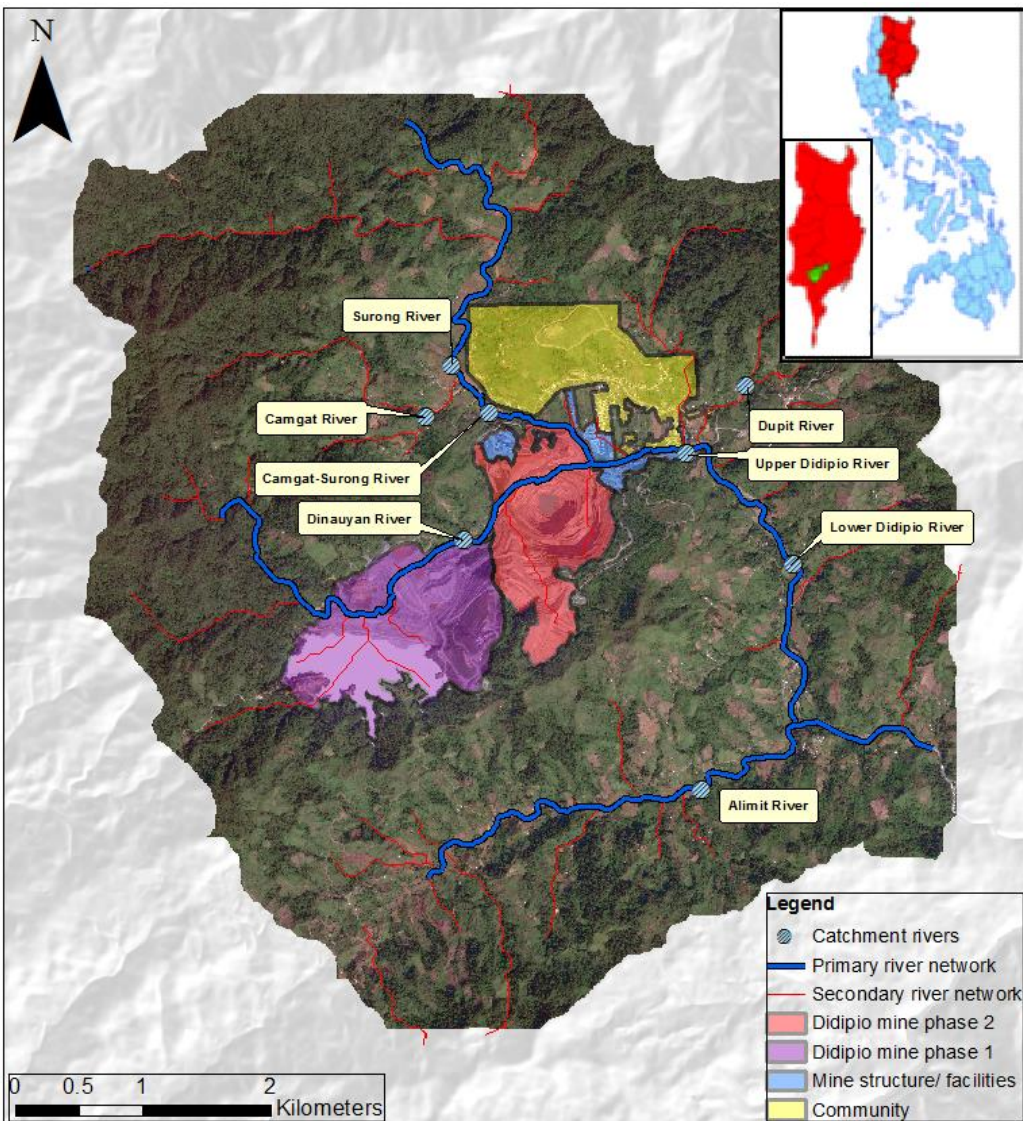


Figure 4-1: Major features of the Didipio catchment area in the Philippines

SPOT: © AIRBUS DS (2016)

In March 2012, the majority of small-scale mining sites were near the rivers. During this period, excavating and panning the river sediments was the principal mining method (Figure 4-2). Out of the 43 panning sites, 26 and 8 were located in upper and lower Didipio River, respectively, while 9 were situated in smaller tributary creeks of the Dinauyan River (Figure 4-1). In addition, small-scale underground mining began to develop, with tunnels operating perpendicular to these creeks, which became part of the Didipio mine phase 1 during the same year.

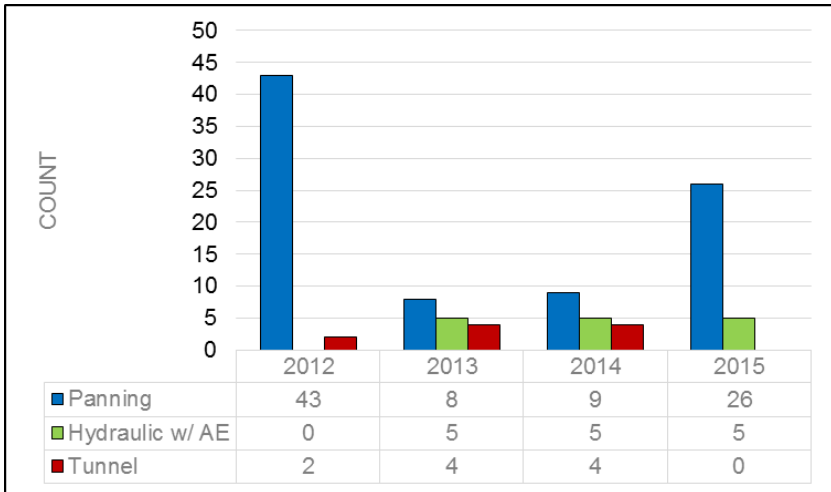


Figure 4-2: Active small-scale mining sites derived from field data from 2012 to 2015 categorized by mining method.

In 2013, hydraulic mining with assistance of hydraulic excavators were introduced in order to increase production yield. These mining practices became dominant in sites operating near the Dinauyan River and near the junction of the Camgat and Surong rivers. The development of small-scale underground mines remained common through 2013, with 4 newly constructed tunnels beside the lower Didipio River. All of the surveyed small-scale mines in terms of land clearance were between 50 and 100 m width; and between 400 m² and 14,000 m² surface area. Those mines located on exposed rocks (left of lower Didipio River) had properties similar to the open-pit mine, whereas the mines near the rivers had a diverse appearance of sediments and topsoil (Figure 4-3).

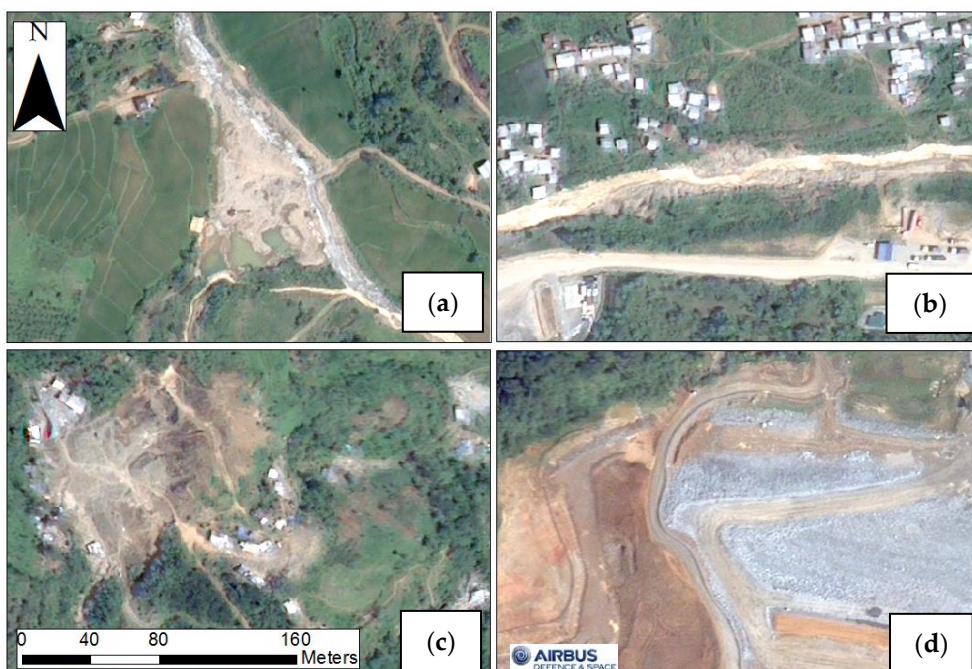


Figure 4-3: Different forms of mining in Didipio catchment. (a) Sediment pit; (b) Panning area; (c) Small-scale mines on hard rocks; (d) Large-scale open-pit mine.
Pleiades: © CNES (2013), Distribution Airbus DS / Spot Image

By 2014, the majority of the small-scale mines had moved from their initial locations to higher elevations. Along the Camgat River, newly established mines of larger scale (but still within the definition of small-scale mines) were observed. Meanwhile, the development of new underground mines slowed. In 2015, most of the mine tunnels had been abandoned, but small-scale mines on the surface, particularly near the Camgat River, were still operating (Figure 4-4).

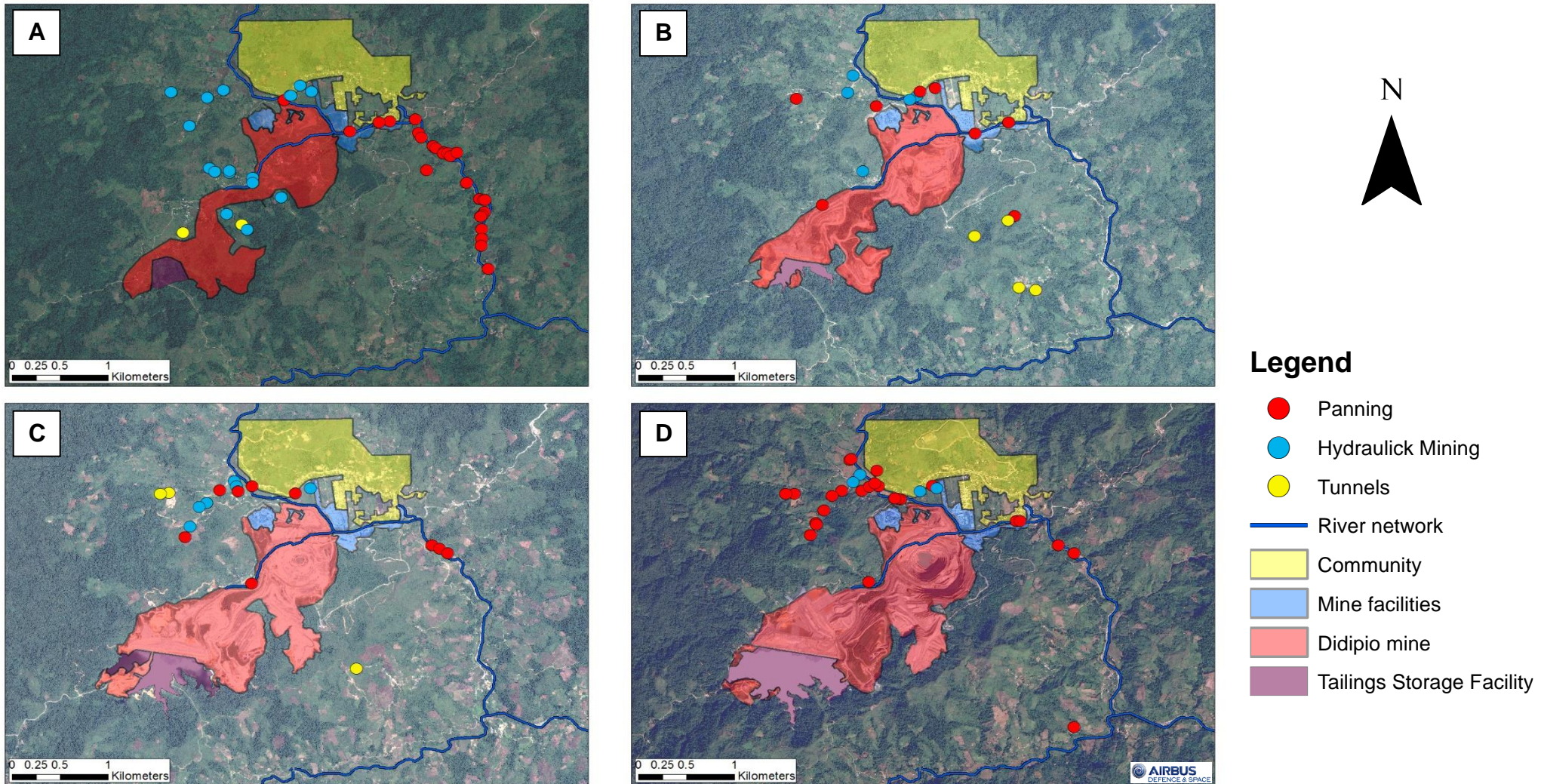


Figure 4-4: Locations and types of active small-scale mine sites based on ground surveys, superimposed on remote-sensed images
 From upper left to lower right: (a) 2010 WorldView-2 image (2010 data used due to lack of alternative cloud-free image in 2012); (b) 2013 Pleiades-1A image; (c) 2014 Pleiades-1A image; (d) 2016 SPOT-6
 2010 Satellite Image courtesy of the [DigitalGlobe Foundation](#); Pleiades: © CNES (2013, 2014), Distribution Airbus DS / Spot Image; SPOT: © AIRBUS DS (2016)

4.1.2 Selection of satellite images

The size of small-scale mines was the primary consideration in selecting the source satellites with visible footprints as low as 50 m in width. Landsat 8 was discounted due to its low spatial resolution (~30 x 30 m pixel size). The availability of satellite images was also a limitation due to cloud cover. Two satellite data sources were selected, which addressed both these limitations; SPOT-6 and Pleiades-1A, with pixel sizes of 2 m and 6 m, respectively (Table 4-1).

Table 4-1: Technical specifications of the three scenes (2013, 2014, 2016) and sensor characteristics

Scene				Sensor					
Satellite and sensor	Acquisition	Sensor angle	Cloud cover	Band	Designation	Wavelength		Spatial resolution	
	Date	degrees	(%)			(μm)		(m)	
Pleiades-1A High-Resolution Imager (HiRI)	20 Mar. 2013	23.74	1.2	1	Blue	0.43	-	0.55	2
	5 May 2014	4.89	1	2	Green	0.50	-	0.62	2
				3	Red	0.59	-	0.71	2
				4	Near-Infrared	0.74	-	0.94	2
				5	Panchromatic	0.47	-	0.83	0.5
SPOT-6 New AstroSat Optical Modular Instrument (NAOMI)	6 Jan. 2016	11.93	2	1	Blue	0.46	-	0.53	6
				2	Green	0.53	-	0.59	6
				3	Red	0.63	-	0.70	6
				4	Near-Infrared	0.76	-	0.89	6
				5	Panchromatic	0.46	-	0.75	1.5

The Pleiades and SPOT images originate from pairs of identical satellites (SPOT-6 and 7; and Pleiades-1A and 1B), which revolve in the same orbital plane (Postelniak, 2014), making it possible to secure coherent images with identical spatial extents every one to two days, increasing the probability of obtaining cloud-free images. In addition, both sources provide three spectral channels in the visible spectrum, a single channel of near-infrared and a panchromatic band. For the Didipio catchment, two images with near-zero cloud cover were captured from Pleiades-1A on 20th March 2013 and 5th May 2014, while one image with near-zero cloud cover was captured from SPOT-6 on 6th January 2016 (Table 4-1). Out of all the SPOT and Pleiades images from January 2012 to January 2016 with acceptable deviations from nadir, these images were the only ones identified with less than 1.5% cloud cover.

4.1.3 Pre-processing stages of satellite image data

4.1.3.1 Radiometric calibration of sensors

Radiometric calibration of the images was performed to: 1) normalise brightness values; and 2) calibrate digital data into Top-of-the-Atmosphere (ToA) reflectance. The calibration was conducted in two steps. Initially, the original geometrically corrected images provided by the supplier were calibrated to spectral radiance (L_λ) using a linear equation (Eq. 4.1.1) (Astrium, 2012; Astrium, 2013; Chander et al., 2009) and gain and bias values obtained from the supplementary metadata for each acquisition (Appendix E). The output of Eq. 4.1.1 for each image was used in Eq. 4.1.2 to derive the ToA reflectance (Astrium, 2012; Astrium, 2013). The band-specific exoatmospheric irradiance at a given sun elevation angle (θ_{SE}) and earth-sun distance (ESUN) during the acquisition of each image were also provided from the metadata (Appendix E). The earth-sun distances were manually calculated using Eq. 4.1.3 (Gebreslasie et al., 2010). The Julian date in Eq. 4.1.3 corresponds to number of days between Universal time on 1 January 4713 BC and when the satellite image was captured (Astronomical Applications Department of the U.S. Naval Observatory, 2016).

$$L_\lambda = \frac{Q_{cal}}{GAIN} + BIAS \quad (4.1.1)$$

$$P_\lambda = \frac{\pi \cdot L_\lambda \cdot d^2}{ESUN \cdot \cos(\theta_{SZ})} \quad (4.1.2)$$

$$d = 1 - 0.01672 \cos[0.9856(JD - 4)] \quad (4.1.3)$$

$$\theta_{SZ} = 90^\circ - \theta_{SE} \quad (4.1.4)$$

Where L_λ = spectral radiance; Q_{cal} = Digital number; P_λ = ToA reflectance; ESUN = Solar irradiance; d = Earth-Sun distance; JD = Julian date; θ_{SZ} = Sun zenith angle; θ_{SE} = Sun elevation angle

4.1.3.2 Atmospheric correction

Afterwards, atmospheric correction was applied to the calibrated satellite images from the previous step to reduce the effects of atmospheric absorption and scattering (Gebreslasie et al., 2010). Atmospheric correction was applied using the Quick Atmospheric Correction (QUAC) algorithm provided in the ENVI software (Zinnert et al., 2016; Moses et al., 2012; Vibhute et al., 2016). QUAC is an approximate, in-scene atmospheric approach that normalises images based on the statistical properties of object spectra found within an image (Adler-Golden et al., 2007). The QUAC algorithm can be applied when there are at least 10 diverse objects in the image (Bernstein et al., 2012). The average reflectance of each object is used as baseline reference. Prior to correction, objects with high reflectance values such as clouds were manually masked, and highly structured regions in the image

(e.g. forest areas) were selectively masked by the algorithm. This was followed by linear transformation of spectral signatures by the QUAC algorithm through plotting their reflectance against a set of reference objects from the software's spectral library. The resulting outputs from the application of the atmospheric correction were surface reflectance values as opposed to the ToA reflectance values produced in the previous step.

4.1.3.3 Enhancement of spatial resolution through image fusion and supplementary pre-processing techniques

To increase the spatial resolution, image fusion with a pan-sharpening algorithm was applied to reduce the pixel size of the original multispectral images with the panchromatic band (0.50 m for Pleiades-1A and 1.5 m for SPOT-6). The nearest-neighbor diffuse (NND) algorithm was used for this task. Unlike other pan-sharpening algorithms, this method processes spectral bands separately. NND operates on a per pixel basis, thus providing more accurate spectral information, which can improve land cover classification (Sun et al., 2014). Furthermore, mosaicing technique was applied to sections of the 2014 Pleiades-1A image with clouds over fixed land covers (e.g. forest). This section of the reference image had been cut, and the reference image was merged with the cloud-free equivalent of this section from the 2103 Pleiades-1A image. For the concluding steps, a bilinear resampling technique was used for all the images. The spatial resolution of Pleiades-1A images was reduced to 1 m to remove pixel noise and to quicken the classification process. In contrast, the pansharpened SPOT-6 image (1.5 m) was also resampled to 1 m. To smoothen the intensity contrast of image object boundaries, a 3 x 3 pixels median kernel was applied for all the satellite images. The final products were satellite images with 1 m spatial resolution.

4.1.4 Classification method

For the image classification, a two-step process was used. Firstly, training areas for classification were identified using the four spectral channels of the SPOT-6 and Pleiades-1A images as input file. The example-based feature extraction workflow by ENVI was used, and segmentation parameters were optimised for each image (Appendix F). The scale of segmentation was configured using the edge algorithm. This algorithm locates the outermost edge between image objects, which corresponds to adjacent pixels with the highest intensity contrast (Xiaoying, 2009). The minor image objects were combined through the application of the full lambda schedule algorithm, which merges objects based on similarity of their spatial and spectral properties (Robinson et al., 2002). Before the execution of GEOBIA, a kernel size of 19 by 19 pixels was configured to calculate the values of textural attributes

of the segments. Since the pixel size of the final image is 1 m, the kernel resembles a 19 x 19 m box or equivalent to 361 m². This kernel size is sufficient to capture the textural difference (e.g. footprints) of small-scale mines from other land clearances. Subsequently, the GEOBIA was followed by manual selection of segments to represent alternative forms of each land use in the training data in Table 4-3. The table also displays the number of training segments. In general, 8% and 10% of the catchment area were appointed as training data for Pleiades-1A and SPOT-6, respectively. Moreover, the resulting segments for the SPOT-6 image, although segmentation parameters were configured almost similar to all images, have greater sizes compared with the segments of Pleiades-1A. This is due to difference in spatial resolution between these two satellite sensors. For the SPOT-6 image, this resulted to lower number of segments, but covers a larger area of the catchment (10%). On the other hand, there are several forms of tree canopies present in the catchment, and small segments were generated for forest class thus a large training data was assigned for such class. In addition, a general expansion on various forms of land clearance (e.g. open land, large-scale mine) as well as the Tailings Storage Facility was observed in the 2014 image; therefore, more segments were selected to represent them in the training data. For the small-scale mine (SSM) class, the ground surveys that best coincided with the image acquisition dates were used to develop its training data. The ground surveys in February 2013 and April 2014 for the Pleiades-1A images; and the ground survey from December 2015 for the SPOT-6 image were used as references. The training and assessment data included the active mines.

Table 4-2. Ground survey dates that coincided with the selected satellite images

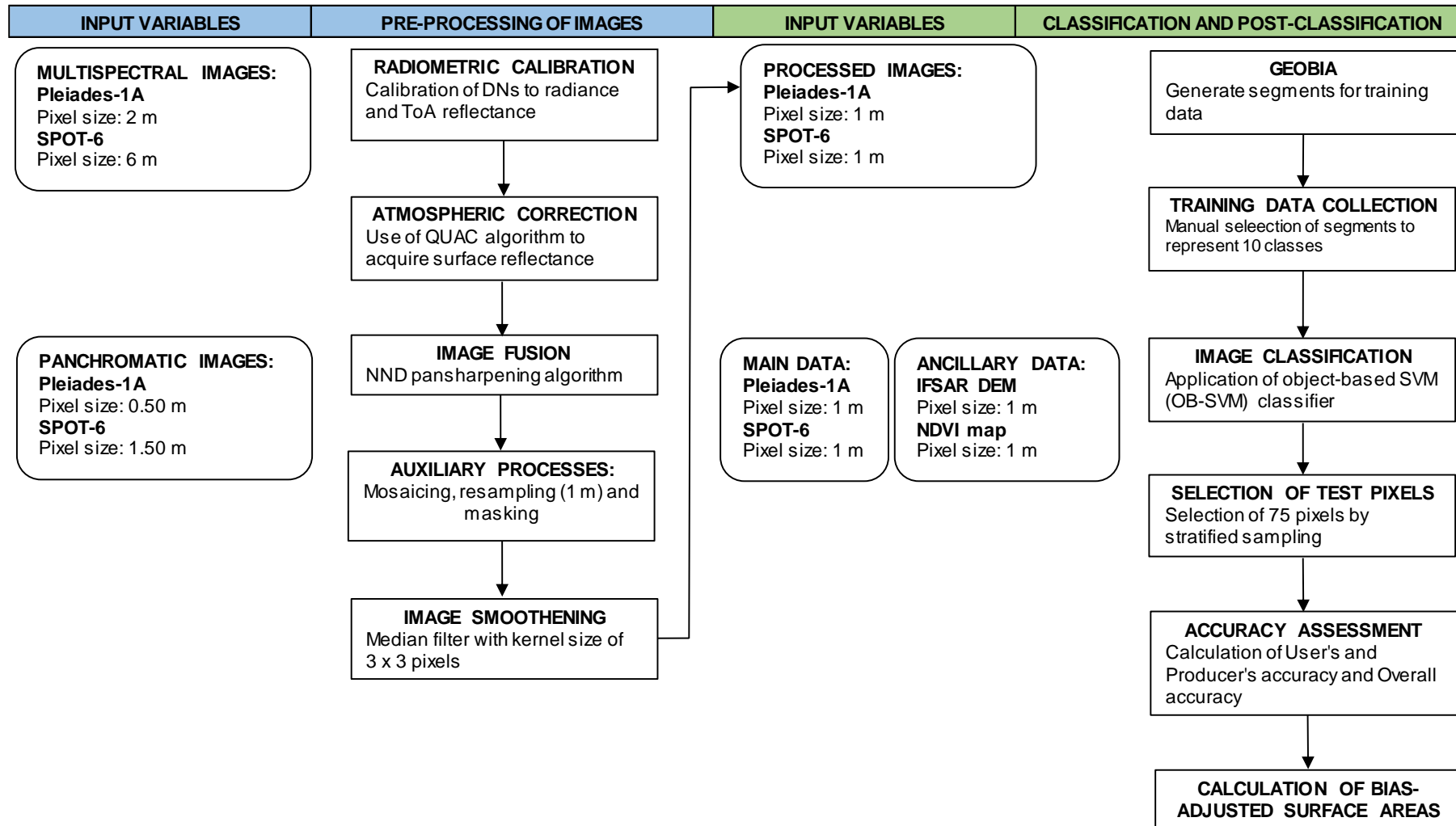
Satellite platform	Image acquisition	Ground survey
Pleiades-1A	20 March 2013	February 2013
Pleiades-1A	05 May 2014	April 2014
SPOT-6	06 January 2016	December 2015

Table 4-3: Descriptions of the land use classes and size of training data in each image

Classes	Training data (no. of segments)			Description
	2013	2014	2016	
Forest	1131	1156	491	Includes all types of trees in the catchment
Grassland	463	267	252	Vegetated areas that do not contain any trees or shrubs
Cultivated area	228	224	212	Agricultural lands
Open land	186	382	214	Mixture of trees, shrubs, and newly burned/ cut forest timbers
Large-scale mine	399	813	188	Open-pit mine and other natural mine components such as haulage roads, stockpile areas and motor pool open wash bays
Tailings Storage Facility	13	40	25	Mine tailings dam
Small-scale mine (SSM)	108	405	47	Includes all possible active mine sites in use for hydraulic mining, gold panning, and underground mining and improvised rough roads within the SSM
Road system/ Vacant lot	412	822	293	Includes the municipal road, access areas and vacant lots surrounding each house in the local community, access to mine facilities and camp site
Built-up	171	229	214	House, buildings, and mineral processing facilities
Stream network	226	157	69	Clear water, highly turbid water and riverbanks

Afterwards, a 5-meter Interferometric Synthetic Aperture Radar (IFSAR) Digital Elevation Model (DEM) was resampled to 1 m. The IFSAR DEM of the catchment was acquired between March and July 2013. It was used to form a composite image with the four spectral channels of each image of Pleiades-1A and SPOT-6 and their respective NDVI maps through image stacking. These multiple spatial data were used as inputs for the calculation of the spatial, spectral and textural attributes of training data prior the application of the classifier (Appendix F). Next, the selected classifier, which is the object-based Support Vector Machine (OB-SVM), was configured. To assist the OB-SVM in searching the optimum boundaries among the classes, a kernel was used. For this research, a nonlinear radial basis function (RBF) kernel of gamma (γ) = 0.01 was used for Pleiades-1A image in 2013. Values of γ from 0.1 to 1 were tested previously, and γ = 0.1 gave the optimum boundaries among classes with less misclassification rate (Huang et al., 2002) whereas γ = 0.01 was used by Lin et al. (2015) in classifying 10 land use features. However, a gamma (γ) of 0.05 was selected for the 2014 Pleiades-1A and 2016 SPOT-6 as it was verified to have the best result for these images. The workflow that was performed from pre-processing of the images to classification and post-classification processes is illustrated in Figure 4-5.

Figure 4-5: Flowchart of image pre-processing and image analysis (classification and post-classification)



4.1.5 Accuracy assessment

The classification results were assessed relative to the ground-truthed data. Seventy-five test pixels for each land use class were sampled from the map of classification results. Stratified sampling was used, as implemented in the ENVI software. This sample size meets the guidelines provided from previous studies (Congalton, 1991; Jensen, 1996). The training data pixels were excluded during sampling of test pixels. The 75 pixels of each class from the classified map were visually evaluated if they essentially represent their classes based on the vegetation cover map from the ecological assessment of Didipio Project, supplementary GIS data of ground truths of small-scale mines and manual photo interpretation of the images (general knowledge of the catchment). Afterwards, the class label of each misclassified pixel was corrected. The corrected pixels were assigned as ground-truthed points, which were used as basis in generating a confusion matrix for each image (Ting, 2010). The confusion matrix evaluates accuracy using a two-dimensional matrix. The values across a row labeled ‘X’ represent the number of test pixels classified as land cover ‘X’; while the values down a column labeled ‘Y’ represent the number of test pixels ground-truthed as ‘Y’ (Al-Fares, 2013). Therefore, the values on the matrix diagonal are the number of test pixels correctly classified for each land use class. These correctly classified test pixels were divided by the total number of test pixels (N) available from each land use class to acquire the overall accuracy of classification of each image (Eq. 4.1.5). To provide information on the nature of errors, the Producer’s Accuracy (error of omission; Eq. 4.1.6) and User’s Accuracy (error of commission; Eq. 4.1.7) were also determined for each class (Story & Congalton, 1986).

$$OA = \frac{\sum_{i=1}^n R_i}{\sum_{i=1}^n N_i} \quad (4.1.5)$$

$$PA_i = \frac{R_i}{M_i} \quad (4.1.6)$$

$$UA_i = \frac{R_i}{N_i} \quad (4.1.7)$$

Where OA = Overall accuracy; PA= producer’s accuracy; UA = User’s accuracy; n = Number of classes; R_i = Number of correctly classified test pixels in class i; N_i = Number of test pixels that are classified to be in class i (=75); M_i = Number of test pixels that are ground-truthed to lie in class i

In conducting an accuracy assessment, misclassified test pixels of land cover ‘X’ impose several biases to estimation of area coverage of each class; therefore, the contribution of misclassified test pixels multiplied by the weight of the class in which they were classified are considered in deriving the actual estimates of surface areas (Eq. 4.1.8 and 4.1.9) (Olofsson et al., 2013). The separate standard errors of the bias-adjusted surface areas were determined (Eq. 4.1.10) to approximate the margin of error of each class at 95% confidence interval (Eq. 4.1.11).

$$P_{ij} = W_i \cdot \frac{t_{ij}}{t_i} \quad (4.1.8)$$

$$A_j = A_{\text{Total}} \sum_i P_{ij} \quad (4.1.9)$$

$$S(P_j) = \sqrt{\sum_{i=1}^n W_i^2 \frac{\frac{n_{ij}}{n_i} (1 - \frac{n_{ij}}{n_i})}{n_i - 1}} \quad (4.1.10)$$

$$A_j \pm 2 \cdot S(P_j) \cdot A_{\text{Total}} \quad (4.1.11)$$

Where P_{ij} = Weight of misclassified test pixels in each row; W_i = ratio of the calculated class area and total area; A_j = Bias-adjusted surface area; $S(P_j)$ = Standard error

4.2 Results and discussion

4.2.1 Comparison of spectral signatures across land use classes

Comparing the spectral signatures for the training data (Figure 4-6) gives some insight into the challenge of classification. Unlike the vegetated areas (e.g. forest, grassland, cultivated area), which have distinct reflectance values in the near infrared channel (825 nm), several classes (Figure 4-6 Plot 1B, 2B, 3B) in which soil is exposed have similar reflectance across all spectral channels. This plot of spectral signatures illustrates how surface reflectance responds inversely with soil layer. The open land, which involves stripping and burning of vegetated covers only, has the lowest surface reflectance among the forms of bare soil. In contrast, small-scale mines expose a different soil layer that is found in deeper ground level, and has higher reflectance compared with open land. However, road system and vacant lots have slightly higher reflectance than SSM class despite of the absence of deep ground excavation activities in these class. In the Philippines, constructed roads in rural regions, particularly those situated in mountains, are composed of sand and gravel in small fraction. Instead, they are covered with compacted soil sitting over hard rocks. The smooth texture of a compacted soil on roads decreases the scattering of light (e.g. higher reflectance is transmitted back to satellite sensor). The scattering of light is potentially observed in small-scale mines. Furthermore, smooth texture of pit benches coupled with exposure of bedrocks make the large-scale mine to have the highest overall surface reflectance relative to abovementioned classes. In the visible spectrum, open land, small-scale mines, and road system display the highest surface reflectance in the red channel. In contrast, the large-scale mine has almost similar surface reflectance values in all visible bands as its surface exposes both soil (developing phase mine sections) and compacted bedrocks. On the other hand, the variation of reflectance in near infrared region provide information on the potential presence of patches of vegetation on these forms of bare soil in some areas of the catchment. For instance, the

open land in the 2013 image, despite of having the lowest overall reflectance in the visible spectrum, has the highest surface reflectance in the near infrared channel. This is explained by the open land's textural property, which incorporates minor patches of shrubs. Moreover, stream network in this study comprises of clear water, highly turbid water and riverbanks, and resulted to a spectral signature similar with the forms of bare soil.

Based on this discussion, it presents that spectral attribute is not sufficient to separate the small-scale mines from other land use classes that strip soil. This illustrates the importance of GEOBIA, which also considers the spatial and textural properties of image objects. The supplementary application of NDVI maps helped separate vegetated areas from bare soil, but was unhelpful for identifying small-scale mines from other forms of bare soil such as the road system. The high mean NDVI of forest (greater than 0.81) makes it separable from grassland and cultivated areas, while the NDVI value of small-scale mines is similar with road system. The mean NDVI of SSM and road system classes across the three years were 0.35 and 0.33, respectively (see Appendix G).

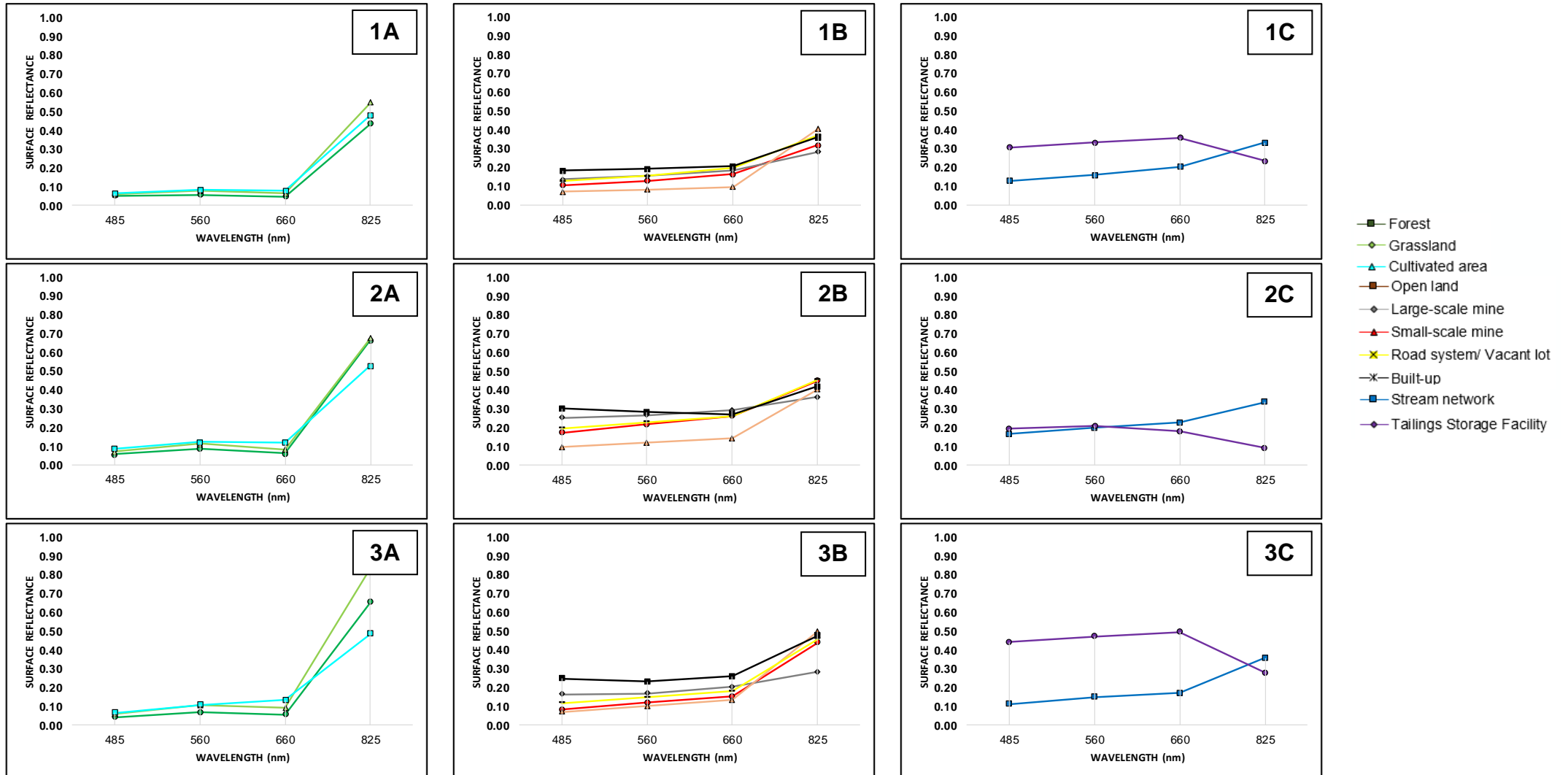


Figure 4-6: Plots of spectral signatures of land use subclasses using mean values of reflectance across all training data

(a) 20 March 2013 Pleiades-1A; (b) 05 May 2014 Pleiades-1A; (c) 06 January 2016 SPOT-6

4.2.2 Accuracy assessment of classification for Pleiades-1A and SPOT-6 images

The Producer's Accuracy (PA) values for the SSM class were 90%, 93% and 96% for the 2013, 2014 and 2016 images (Table 4-4). The high PA values illustrate that almost all of the small-scale mines were correctly classified. However, lower values of User's Accuracy (UA) were obtained for the SSM class: 76%, 69% and 69% for the 2013, 2014 and 2016 images (Table 4-4). The lower UA values illustrate that a significant number of pixels were misclassified as SSM.

The misclassification of other land uses as SSM may be attributed to several factors. Firstly, Table 4-4 shows that there are 3 to 10 test pixels in the 2013, 2014 and 2016 images that were actually large-scale mining but were misclassified as SSM. This is likely to be due to spectral and textural similarities of the SSM class with the construction of the in-pit ramps and benches between 2013 and 2016. The application of the IFSAR DEM as ancillary data during image classification only contributed in discriminating the sections of large-scale mine that were already present during the acquisition of the IFSAR DEM. The IFSAR DEM provided the information on the ground depression difference between the large-scale mine and the small-scale mines as well as their distribution throughout the catchment. The large-scale open pit mine was also among the well-classified land uses, with UA values of 95%, 97% and 100%. Its size, unique shape and textural consistency generated distinguishable segments that were easily recognised by the OB-SVM classifier. Secondly, in the 2013, 2014 and 2016 images, 6, 11 and 7 test pixels that were actually part of the road system and/or vacant house lots were misclassified as SSM. This may be because the textural properties of the segments from these two classes could not be reliably distinguished.

Moreover, in the 2013 and 2016 image, 6 separate pixels of cultivated area were misclassified as SSM. In small-scale mining, stripping of ground cover is selective, and difficult-to-access ore bodies are left partially stripped and less undisturbed (see Appendix D for the images). On several occasions, the extraction of only a single section of the ore was observed over an extended period. Therefore, although deeper soil layers are exposed, these areas are often small compared to the superficial disturbance that is easily misclassified as cultivated area or open land. In addition, both small-scale mines and open land have irregularly shape segments. This kind of misclassification was also encountered in 2014 image, but with lower frequency. This is likely to be because the higher spatial resolution of this image allowed the textural features of small-scale mines to be better distinguished.

Table 4-4: Generated Confusion Matrix for each image data a) 2013 Pleiades-1A b) 2014 Pleiades-1A c) 2016 SPOT-6

(F: Forest, GL: Grassland, CA: Cultivated area, OL: Open land, LSM: Large-scale mine, TSF: Tailings Storage Facility, SSM: Small-scale mine, RS: Road system/Vacant lot, BU: Built-up, SN: Stream network, PA: Producer's accuracy, UA: User's accuracy)

(a)	GROUND TRUTH CLASSIFICATION										TOTAL	UA (%)
	F	GL	CA	OL	LSM	TSF	SSM	RS	BU	SN		
OB-SVM CLASSIFICATION	F	75	0	0	0	0	0	0	0	0	75	100
	GL	4	68	3	0	0	0	0	0	0	75	91
	CA	4	14	55	2	0	0	0	0	0	75	73
	OL	1	0	2	72	0	0	0	0	0	75	96
	LSM	0	0	1	0	71	0	0	3	0	75	95
	TSF	0	0	0	0	0	75	0	0	0	75	100
	SSM	0	1	6	2	3	0	57	6	0	75	76
	RS	0	0	0	0	6	0	5	59	0	75	79
	BU	0	0	0	0	0	0	0	73	2	75	97
	SN	0	0	4	0	0	0	1	11	0	59	75
TOTAL		84	83	71	76	80	75	63	79	73	66	750
PA (%)		89	82	77	95	89	100	90	75	100	89	

(b)	GROUND TRUTH CLASSIFICATION										TOTAL	UA (%)
	F	GL	CA	OL	LSM	TSF	SSM	RS	BU	SN		
OB-SVM CLASSIFICATION	F	74	1	0	0	0	0	0	0	0	75	99
	GL	2	71	2	0	0	0	0	0	0	75	95
	CA	0	16	52	5	0	0	0	2	0	75	69
	OL	1	1	4	66	2	0	0	1	0	75	88
	LSM	0	0	0	0	73	0	1	1	0	75	97
	TSF	0	0	0	0	6	69	0	0	0	75	92
	SSM	0	0	2	5	5	0	52	11	0	75	69
	RS	0	0	2	1	9	0	3	60	0	75	80
	BU	0	0	0	0	1	0	0	0	74	0	75
	SN	2	0	4	7	0	0	0	4	0	58	77
TOTAL		79	89	66	84	96	69	56	79	74	58	750
PA (%)		94	80	79	79	76	100	93	76	100	100	

(c)	GROUND TRUTH CLASSIFICATION										TOTAL	UA (%)
	F	GL	CA	OL	LSM	TSF	SSM	RS	BU	SN		
OB-SVM CLASSIFICATION	F	75	0	0	0	0	0	0	0	0	75	100
	GL	5	70	0	0	0	0	0	0	0	75	93
	CA	2	2	57	9	0	0	1	4	0	75	76
	OL	0	1	2	66	2	0	0	4	0	75	88
	LSM	0	0	0	0	75	0	0	0	0	75	100
	TSF	0	0	0	0	2	73	0	0	0	75	97
	SSM	0	0	6	0	10	0	52	7	0	75	69
	RS	0	0	1	1	10	0	1	59	0	75	79
	BU	0	0	0	0	2	0	0	0	73	0	75
	SN	0	0	0	0	0	0	0	4	0	71	95
TOTAL		82	73	66	76	101	73	54	78	73	74	750
PA (%)		91	96	86	87	74	100	96	76	100	96	

The application of Pleiades-1A and SPOT-6 images and OB-SVM classifier to locate small-scale mines had acceptable performance. Although the PA values for small-scale mining were high, the UA values show that as little as 69% of the pixels classified as SSM were irregular segments of vacant house lots, large-scale mining, cultivated areas and open land. Still, the overall accuracy of the OB-SVM classifier applied to these images can be considered satisfactory, with OA values of 89%, 87% and 89% for the 2013, 2014 and 2016 images. The resulting UA for the SSM class may be improved if sufficient cloud-free images could be obtained to capture the growing season, when cultivated areas and open lands have minimal stripping activities and therefore are less likely to be misclassified as SSM. The efficacy of the OB-SVM classifier may be examined on other catchments less affected by cloud cover. In addition, the catchment of Didipio imposed several complexities due to presence of several techniques of small-scale mining at limited coverage. They affect the amount of segments available for each small-scale mining technique.

4.2.3 Coverage and spatial distribution of areas classed as SSM relative to other land use classes

The spatial distribution of the ten land use classes is presented in Figure 4-7 with areas listed in Table 4-5. Due to the misclassifications among the classes (Table 4-3), there are biases in these surface areas. If it is assumed that biases identified for the test pixels represent the whole catchment, these classified areas can be normalised with given margin of errors (Table 4-5). The areas referred to below are the bias-adjusted values. Forest is the dominant natural landscape and, according to OB-SVM classifier, it occupies 60% of the total catchment on average over the three years, mostly in the outer, higher altitude regions of the catchment. Meanwhile, grasslands are classified as being the next most dominant, representing an average of 23% of the area, concentrated at lower altitudes surrounding the large-scale mine. For stripped areas, the dominant land uses according to classifier were open land, large-scale mining and the road system/ vacant lots, with average areas of 1.94, 1.95 and 0.68 km². The area classified as SSM was on average 98,000 m² representing only 0.25% of the total catchment area, the smallest land use footprint among the ten land use classes. However, the small-scale mining activity may involve, as well as the mines themselves, land uses included under open land, road system/ vacant lot.

Over the three years, there were significant changes in the mining activity. The areas classified as large-scale mine and the Tailings Storage Facility (TSF) increased by 0.77 km² and 0.36 km², respectively. The area classified as SSM increased slightly from 91,000 to 121,000 m² between the 2013 and 2014 images. However, there was a decrease in 2016 by 39,000 m². Based on result, the

possible area coverage of small-scale mines at maximum for each year are 91,000 m², 121,000 m² and 82,000 m² for 2013, 2014 and 2016 images. The decline in small-scale mining in the 2016 image is counter-intuitive if it is considered that all abandoned mines should be classed as SSM. However, abandoned mines that have revegetated were not included in the ground truth surveys, and if they were included in the training data, they will be recognised under other classes. Among these images, an increase from 0.09 to 0.12 km² only can be observed at 100% UA and PA. However, uncertainty on temporal change in SSM coverage can still be observed based on the acquired margin of errors for SSM class (Table 4-5). This temporal change in SSM class coverage can be said to be significant at local scale only.

Table 4-5: Classified areas and Bias-adjusted areas of each land use class

Land use features	2013			2014			2015		
	Classified area (km ²)	Biased-adjusted area (km ²)	Margin of Error (+km ²)	Classified area (km ²)	Biased-adjusted area (km ²)	Margin of Error (+km ²)	Classified area (km ²)	Biased-adjusted area (km ²)	Margin of Error (+km ²)
Forest	24.29	24.91	0.53	22.33	22.31	0.69	23.13	23.80	0.56
Grassland	10.13	9.40	0.69	8.82	8.95	0.77	9.54	8.96	0.56
Cultivated area	1.12	1.29	0.48	1.23	1.30	0.40	1.26	1.02	0.07
Open land	1.13	1.12	0.07	3.31	3.03	0.26	1.70	1.65	0.13
Large-scale mine	1.49	1.46	0.09	2.01	2.17	0.16	2.06	2.23	0.09
Tailings Storage Facility	0.07	0.07	0	0.26	0.24	0.02	0.45	0.43	0.02
Small-scale mine	0.07	0.09	0.03	0.09	0.12	0.07	0.08	0.08	0.02
Road system/Vacant lot	0.58	0.55	0.09	0.80	0.77	0.14	0.70	0.72	0.11
Built-up	0.17	0.17	0.01	0.18	0.18	0.01	0.18	0.18	0.01
Stream network	0.20	0.20	0.04	0.22	0.17	0.02	0.15	0.17	0.03
TOTAL	39.25	39.25		39.25	39.25		39.25	39.25	

The generated thematic maps, apart from evaluating the SSM coverage, show how sediment pits and panning areas are more likely to develop once active whereas underground mines have more static footprints. In addition, these maps also permit judgment about the type of small-scale mining, and how it varies throughout the catchment. For instance, the proximity to a river of areas classed as SSM as well as the presence of small ponds within these areas indicate sediment pits (Figure 4-4). From this, it is inferred that the small-scale mines neighboring the Camgat River, and those situated north of Camgat-Surong River besides the mine facilities/ camp site are mostly sediment pits. This is supported by the ground surveys, where pumps and pipes were observed in these areas. Areas in the upper and lower Didipio River that were classified as SSM were identified in the ground surveys as well as in the images as scoured river banks associated with panning. In contrast, areas classed as SSM to the south of the upper Didipio River (Figure 4-5), which were ground-truthed as tunnels, are

almost 800 m away from the nearest river, and a decreasing surface area was observed within three years. It may be concluded that high resolution satellite images may be useful, not only for identifying areas that are likely to be small-scale mines, but also for distinguishing between the main types of small-scale mine.

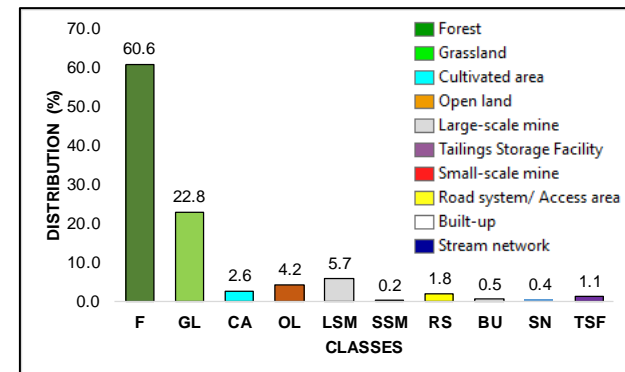
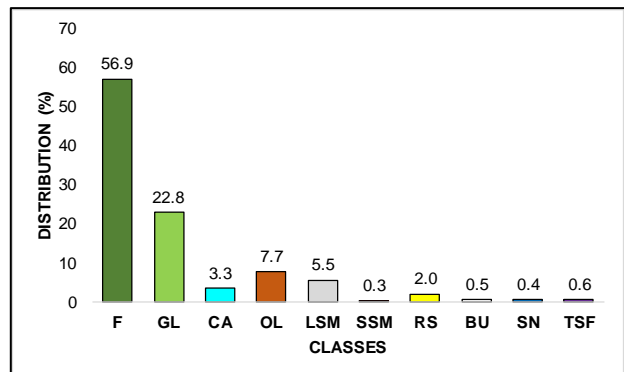
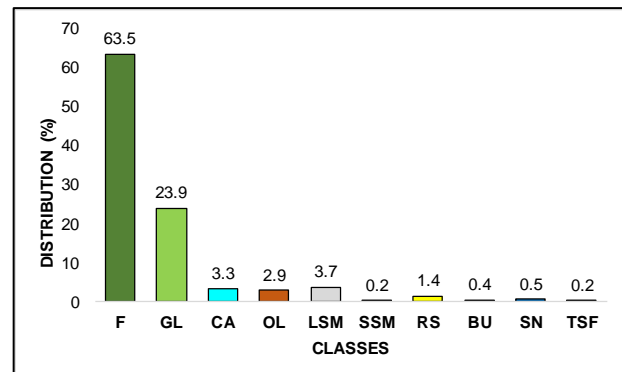
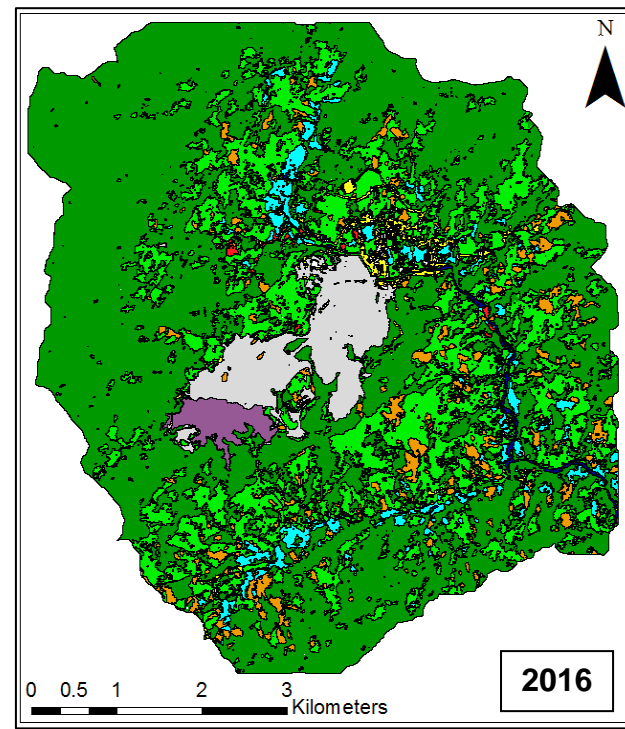
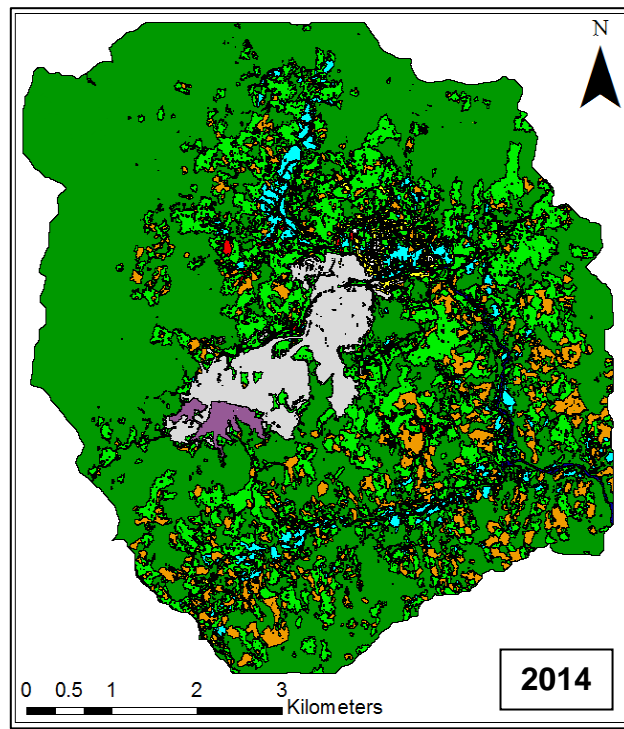
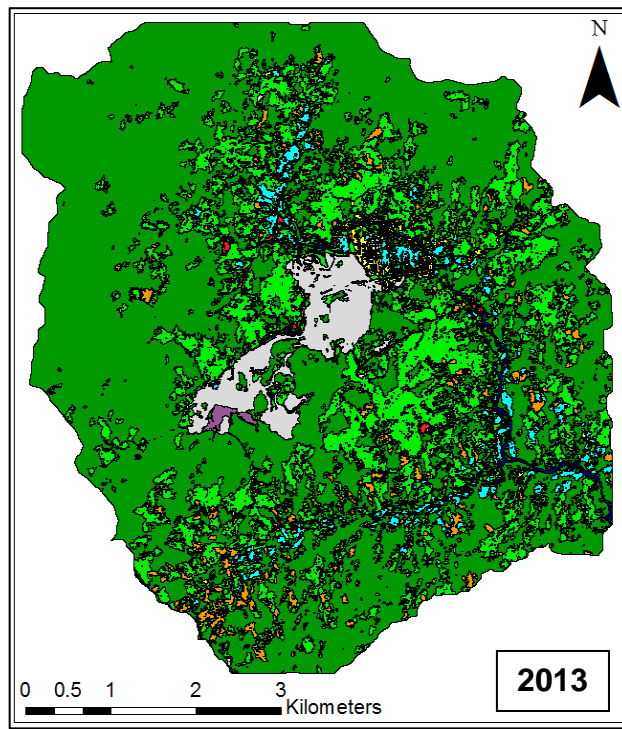


Figure 4-7: Output thematic maps and the corresponding land use class coverage distributions
 (a) 20 March 2013 Pleiades-1A; (b) 05 May 2014 Pleiades-1A; (c) 06 January 2016 SPOT-6

4.3 Summary

Small-scale mining often occurs in remote regions, and may occupy smaller areas and be more transient than other economic land uses. It is therefore often challenging to identify and regulate effectively. The increasing availability of high resolution satellite images is potentially applicable to automatic mapping of small-scale mining development. However, the availability of cloud-free images, and the presence of different types of land use that involve stripping vegetation and soil, may create challenges, especially in wet tropical regions. This paper has explored these challenges through applying high resolution images to mapping small-scale mining over three years in the Dipidio catchment in north-east Philippines.

The application of the OB-SVM to selected Pleiades-1A and SPOT-6 images produced thematic land use maps with an overall accuracy between 87% and 89%. The small-scale mining class was one of the least reliably identified, with user accuracy values from 69% to 76% and producer accuracy values from 90% to 96%. The common misclassification of other land use classes as small-scale mining arose from the spatial, spectral and textural similarities of various forms of bare soil. In contrast, the more unique shape and topographical features of the large-scale mine meant that it was more reliably classified, with user and producer accuracy values ranging from 95% to 100% and 74% to 89%, respectively. Including the textural attributes was essential in determining the footprints of small-scale mines, for which high-resolution images of at least 1.5 m are probably essential.

Qualitative inspection of the thematic maps produced by the high-resolution images also indicated that it may be possible to automatically estimate the type of small-scale mine. The primary limitation of this research was the low availability of suitable satellite images due to the regular cloud-cover over the catchment. Increasing frequency of images may in future permit large training data sets and further improvements in reliably tracking development of small-scale mines.

Chapter 5 Quantifying suspended solids in small rivers using satellite data

Remote sensing has often been employed to assess water quality in marine and coastal contexts (Wu et al., 2014). Its application to inland surface water is generally more difficult. Firstly, the concentrations of suspended and organic materials vary over short distances and time periods (Garbuзов et al., 1993). Secondly, high spatial resolution images are required for extraction of spectral information from narrow rivers (Wu et al., 2014). Lastly, shallow waters expose the river bottom, which may interfere with readings of surface reflectance.

The assessment of water quality using remote sensing may be categorised into (Morel & Prieur, 1977): Class I, which focuses on waterbodies that are dominated by phytoplankton; and Class II, which concentrates on inorganic matters and suspended sediments. Other authors add Case III, which deals with extreme volumes of suspended solids, but is not yet well investigated (Stumpf & Pennock, 1991). In this paper, the Didipio catchment was classified as Case II scenario based on the dataset available for analysis.

The application of satellites to water quality assessment relies on relating solar radiation reflected from the water body, as measured by a sensor on the satellite, to a water quality parameter. Several researchers have focused on remote sensing of total suspended solids (TSS), or water turbidity as surrogate of TSS. In general, turbidity and TSS have an almost linear relationship with TSS:turbidity ratios in the range from 1 to $2.5 \text{ mgL}^{-1}\text{-NTU}^{-1}$ (Rugner et al., 2013). A nonlinear relationship has been observed when TSS and turbidity values are greater than 800 mgL^{-1} and 600 NTU, respectively (Wu et al., 2014), although the former value may be as low as 600 mgL^{-1} (Han & Rundquist, 1996). While various indices of radiation are used, surface reflectance is usually applied as it already incorporates corrections for the magnitude of solar radiation, and the sun zenith angle.

Several researchers have demonstrated the strong correlation between certain channels of the reflectance spectrum and TSS or turbidity using satellite images. For measurements ranging from 4 to 40 NTU, turbidity has been found to be significantly correlated with the green (520 nm) and red channels (652 nm) of ALOS AVNIR-2 (Syahreza et al., 2012) while TSS concentrations between 74 and 600 mgL^{-1} were observed to have positive relationship with surface reflectance of MODIS Band 2 (841-876 nm) (Wang & Lu, 2010). On the other hand, other studies have determined the correlation between TSS and in-situ measurements of surface reflectance using a spectroradiometer. With the use of such equipment, turbidity values ranging from 10 to 600 NTU were observed to consistently increase with surface reflectance in all visible and near-infrared channels particularly between 580

nm and 900 nm (Wu et al., 2014). TSS concentrations between 0 and 500 mgL⁻¹ were found to be well correlated with surface reflectance in the near-infrared channel (Harrington Jr et al., 1992). Moreover, TSS was observed to have a high affinity to surface reflectance at a mean wavelength of 656 nm or the red channel in the Tapajos River Basin of Brazilian Amazon (Lobo et al., 2016). In contrast, nonlinear relationship between surface reflectance and turbidity or TSS values can be encountered at their higher ranges, and the nature of the nonlinearity is influenced by the sediments particle size, shape and color (Baker et al., 1984). The nonlinear relationship between TSS and surface reflectance is often expressed as exponential model (Harrington Jr et al., 1992), power model (Wang J.-J et al., 2012) or a second-order polynomial model (Lodhi et al., 1997).

In general, the spectral signature of water has a peak surface reflectance between the green and red channels at lower TSS concentrations while the peak shifts towards the near-infrared channel or longer wavelength at higher TSS concentration. (Syahreza et al., 2012). From the other study (Liew et al., 2003), the spectral signatures of TSS measurement levels between 16 mgL⁻¹ and 1,338 mgL⁻¹ were observed to have two separate peaks in 700 nm and 800 nm, respectively. At higher TSS concentration, these peaks are merged and moves towards the near-infrared channel. This spectral signature is specifically observable for extreme TSS values on inland waters. In addition, saturation of surface reflectance can be detected at extreme TSS values typically higher than 7,450 mgL⁻¹ (Wang J.-J et al., 2012; Liew et al., 2003).

In the absence of suspended solids, the clear water highly absorbs radiation in near infrared channel (e.g. 740 to 900 nm). However, the strength of correlation between reflectance and TSS or turbidity may be affected by the reflectance of river bottom in shallow waters particularly in mountain rivers. Han and Rundquist (1996) discuss the separate impacts of bright and dark river bottoms on surface reflectance readings. Their experiment was performed in a tank with 80 cm depth of water. It was observed that the brightness of the bottom has minimal effect on the surface reflectance readings of the visible spectrum if the TSS concentration is more than 100 mgL⁻¹; and surface reflectance readings are purely attributed to TSS in the near-infrared region, irrespective of the depth of the river bottom. In contrast, at lower TSS, surface reflectance can increase in the blue and green channels (between 495 and 559 nm), due to influence of dark bottom. In conclusion, it was suggested that for shallow rivers, the near-infrared channel (between 740 and 900 nm) should be used to measure surface reflectance. This is supported by Han and Rundquist (1994) and Wu et al. (2014) who propose that surface reflectance is optimally related to TSS between 700 and 900 nm.

Based on the previous studies, the application of satellite images in remote acquisition of TSS and turbidity values were focused on rivers with widths that extend from 1 to 15 km. For instance, Tapajos River in Brazil has downstream width between 10 and 15 km (Lobo et al., 2016). It was recommended to use high spatial resolution imageries between 2 m and 10 m for narrow inland waters (Dekker & Hestir, 2012).

There are three objectives in this chapter. Firstly, the chapter will test the hypothesis that TSS variations can be detected by remote sensing for the stream widths between 4 and 10 m. Secondly, the chapter will determine which type of satellite product allows detection under these conditions. Lastly, the chapter will look at the empirical relationship between surface reflectance at each spectral channel and ground-based measurements of TSS, and then develop and evaluate an empirical regression model to estimate the spatially continuous TSS concentrations from the satellite images.

5.1 Research approach

5.1.1 Selection of monitoring stations

The Didipio catchment is heavily impacted by the activities from small-scale mines. Among its rivers, the Dinauyan, Camgat-Surong and Didipio are the major tributaries with noticeable suspended sediments. Based on a four-year water quality data (2014-2016), Camgat-Surong has higher concentration of suspended solids than Dinauyan and Didipio. In addition to existing panning activities in Camgat-Surong River, the small-scale mines from its upstream, the Camgat River, contribute to its high TSS measurement level. Whereas the Dinauyan River is being least utilised by small-scale mines among these rivers and mostly residential houses are found on its upstream. Moreover, the Didipio River receives the collective impacts of small-scale mining from both Dinauyan and Camgat-Surong rivers.

Table 5-1: Physical attributes and locations of the monitoring stations

River	Station	Coordinates		Width (m)	Average Depth (cm)
		Northing	Easting		
Dumulag property upstream	DP-UP	333,933	1,805,408	4	25
Dumulag property downstream	DP-DOWN	334,270	1,805,607	4	25
Dinauyan downstream	SWS-12	335,038	1,806,039	5	25
Camgat-Surong	SWS-13	335,041	1,806,099	8	31
Didipio River	SWS-14	335,072	1,806,049	9	33

These rivers, being located on higher ground elevation, have noticeable narrow top-widths and shallow depths (Table 5-1). The Camgat-Surong and Didipio rivers are wider compared with the Dinauyan River. The acquisition of samples on these sites is scheduled between 9:00 am and 11:00 am. For this study, the selected monitoring stations are the only ones that have TSS data during the time the nominated satellite images of the catchment were captured. For the selected stations as shown in Figure 5-1, DP-UP monitors the TSS level of Dinauyan River upstream while its downstream water passes through DP-DOWN and SWS-12 stations. On the other hand, the TSS level at the discharge outlet of Camgat-Surong River is monitored through SWS-13, and TSS level in Didipio River is being observed separately at SWS-14 station.

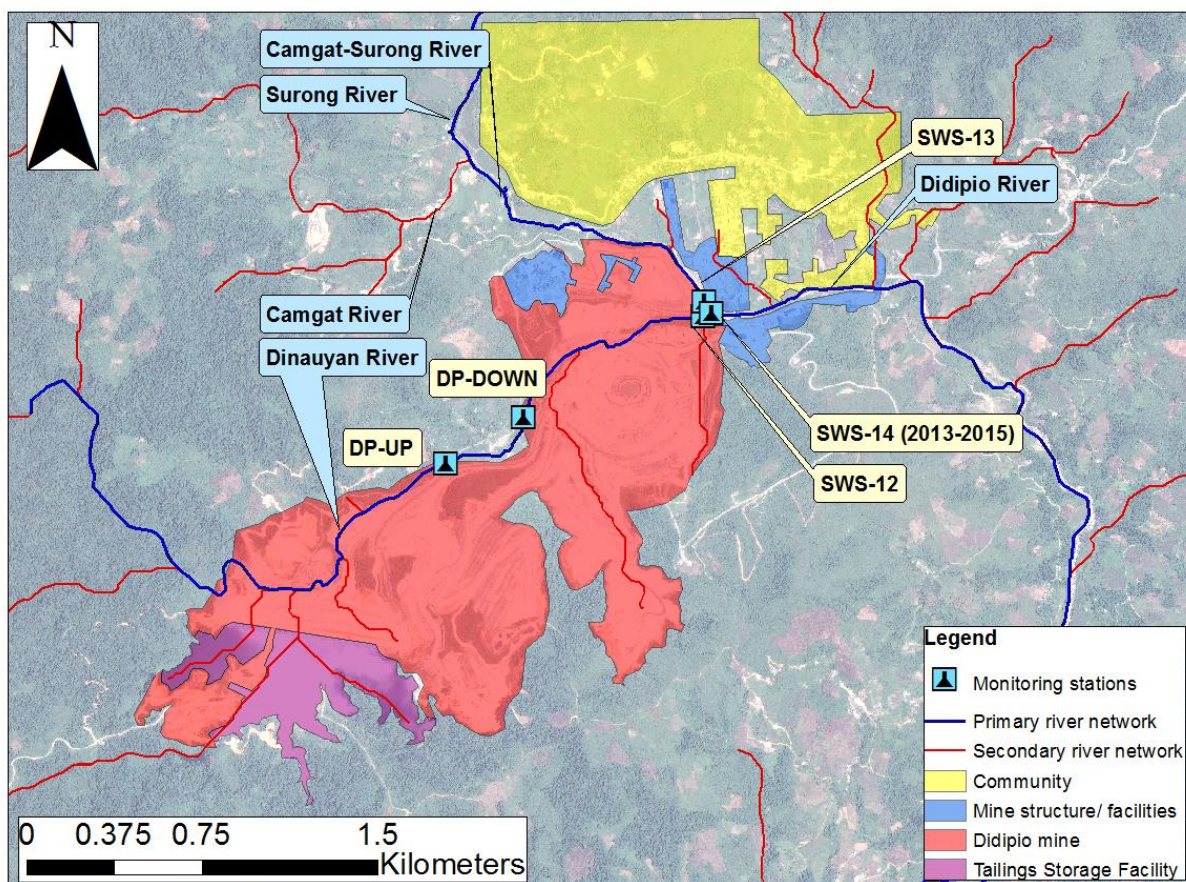


Figure 5-1: Locations of selected monitoring stations
Pleiades: © CNES (2013), Distribution Airbus DS / Spot Image

5.1.2 Selection of satellite products

The selection of satellite products was concentrated on the image spatial resolution and acquisition time. For the spatial resolution, securing at least one pixel that is completely within the river top-width is preferred. An image with 2 m x 2 m wide pixels can satisfy this criterion while a 6 m x 6 m is likely to overlap the riverbank. Moreover, the image acquisition time should agree with the in-situ

sample acquisition period. Supplementary considerations include the sensor incident angle from nadir and the percentage of cloud coverage, with more accurate images being produced when they are at minimum values. A lower deviation of the incident angle from nadir can reduce geometric errors during image orthorectification (Canada, Geometric Distortion in Imagery, 2015).

In addition, the absence of clouds (e.g. cirrus and cumulus) can increase the credibility of the spectral readings of the pixels. An image object or pixel, although not covered by clouds, increases in surface reflectance as it gets near the edge of the cloud. Whereas the cloud shadow can reduce the reflectance value of a pixel below it (Wen et al., 2006).

Table 5-2: Technical specifications of selected satellite images

Imagery	Launch date	Acquisition		Spatial resolution (m)		Sensor angle degrees	Cloud cover (%)
		Date	Time	MS	PAN		
Pleiades-1A	16 Dec. 2011	20 Mar. 2013 5-May-14	10:45:53 AM 10:35:14 AM	2 2	0.5 0.5	23.74 4.89	1.2 1

Two Pleiades-1A satellite images, one in 2013 and one in 2014 were used (Table 5-2). These images were selected as other available images either have lower spatial resolution or have high levels of cloud coverage, which selectively expose the monitoring stations within the scope of the study. The selected Pleiades-1A satellite images have all the stations apparently visible. This satellite passes directly over the case study area at 10:30:00 a.m. every day; however, the time of the image (see Table 5-2) is when the satellite can capture the best possible image including consideration of cloud cover.

For this research, the image analysis was restricted to using the initial spatial resolution of the images. This is because pansharpening, which fuses the panchromatic band with the multispectral image in order to refine the initial resolution of the latter, may distort the reflectance values (Zhang & Roy, 2016).

5.1.3 Water quality data against the test pixels

There were six adjacent test pixels assigned for each monitoring station (Figure 5-2). These pixels were used to examine the local scale variability of surface reflectance that may occur due to variations in properties such as river depth and river bottom brightness. Each set of test pixels was placed within the top-width of the river sections being monitored.

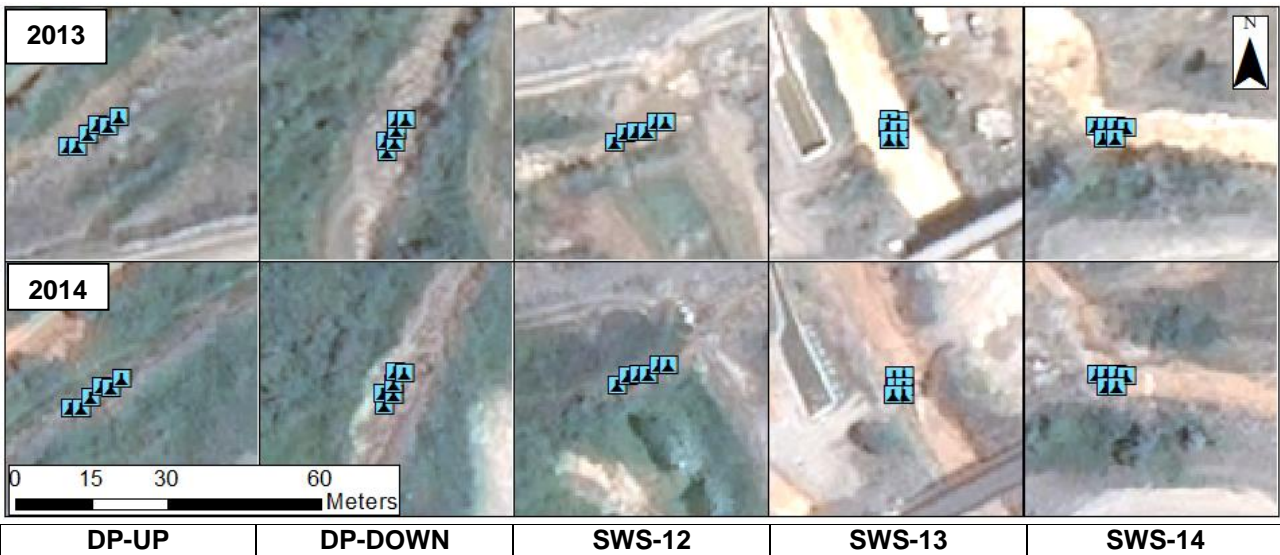


Figure 5-2: Locations of six test pixels for each monitoring station

(Note that pansharpened images were used in this figure for presentation)

Pleiades: © CNES (2013,2014), Distribution Airbus DS / Spot Image

5.1.4 Calibration of images

The calibration of satellite images for this analysis adapted the sequential phases of image pre-processing as discussed in Chapter 4, from Sections 4.1.3.1 to 4.1.3.2.

5.1.5 Variation in turbidity through time

Hourly turbidity measurements were made at three monitoring stations as shown in Figure 5-3, one each from the upstream, middle stream and downstream sectors of the case study. This was carried out during the fieldwork in July 2016, with July being the initial month of the wet season in Didipio, with the purpose of quantifying short-term variations in TSS. With the assistance of OceanaGold's Environmental Technical Team, the time variation of turbidity was analysed, to determine if environmental and anthropogenic factors (e.g. rainfall rate, intensity of small-scale mining activity) are evident. This analysis can also provide information on the potential effect of the satellite image acquisition time deviating from the period of TSS/turbidity sample acquisition.

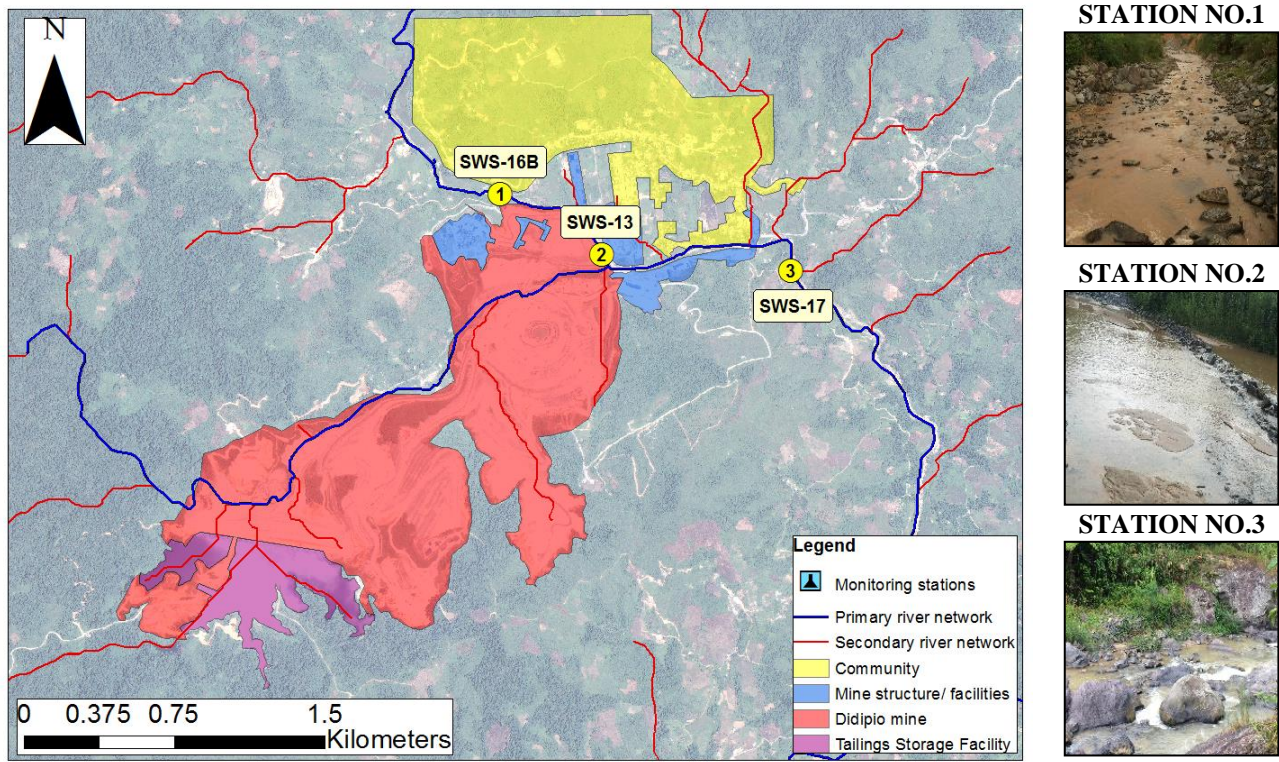


Figure 5-3: Assigned stations for the analysis of river turbidity variation

Pleiades: © CNES (2013), Distribution Airbus DS / Spot Image

A multi-parameter meter (Horiba U-5000) was used to acquire in-situ turbidity measurements. The intensity of rainfall was recorded as being either light or heavy, to assist in interpreting any observed changes in turbidity. These data were incorporated into the hourly plot of turbidity readings to determine their potential contribution to turbidity variation. High rainfall may disturb fine sediments that have settled on the river bottom (Atherholt et al., 1998). These fine sediments contribute to water turbidity for a short period. Moreover, rainfall can induce the erosion of loose soil and movement of sediment bars.

5.1.6 Univariate analysis of surface reflectance and total suspended solids

TSS measurements were compared with the corresponding surface reflectance data. The spectral signature (surface reflectance profile across the four spectral bands) was plotted for each station and for each image date, including all six test pixels representing the station. This allows visual analysis of the effect of TSS on the spectral signature, as well as the local-scale variation. Linear regression was used to model the relationship between TSS and reflectance (Satapathy et al., 2010) (Eq. 5.3.1). This was done using the reflectance data for each spectral band.

$$TSS = A_0 + \sum_{i=1}^n A_i S_i \quad (5.3.1)$$

Where:

- TSS = Modeled value of total suspended solids (mgL^{-1})
- A_0 = y-intercept (constant) (mgL^{-1})
- A_i = slope coefficient for the i th explanatory variable
- S_i = surface reflectance for i th band (e.g blue, red, green, near-infrared bands)
- n = number of explanatory variables considered

The model errors were examined by plotting the reflectance data against TSS measurements for each band. The relevance of each spectral band in the model was presented through the coefficient of determination (R^2) (Eq. 5.3.2). The values of R^2 were determined for the plot of TSS against each spectral band. Furthermore, the root mean square error (RMSE) was used to determine the deviation of the modeled value of TSS from the actual measurement.

$$\text{RMSE}^2 = \frac{1}{n} \sum_{i=1}^n (y_i - M_{TSSi})^2 \quad (5.3.2)$$

Where:

- n = number of data points included in the model
- y_i = observed TSS (mgL^{-1})
- M_{TSSi} = modeled TSS (mgL^{-1})

5.2 Results and discussion

5.2.1 Collective effect of rainfall and ASM to increasing concentration of suspended sediments

The influences of rainfall and ASM on river turbidity are presented separately, based on collective observations from three different monitoring stations that represent the upstream, middlestream and downstream of the case study (Figure 5-4). In Figure 5-4, each line on a graph represents a set of observations collected within a single day, and multiple lines on one graph are results from multiple days. Where a day has evident mining activity near upstream of the monitoring site (SWS-16B and SWS-17), this is isolated in individual plots (B, C and F). An observation was done during the afternoon over three to five consecutive hours.

Based on the acquired data, the impact of light rain over one hour on the turbidity of the upstream river (SWS-16B) can reach 180 NTU (Figure 5-4A). In contrast, evident activity from a hydraulic mining site nearby upstream produced almost twice that increase in turbidity (Figure 5-4B red line;

between 1st and 2nd hour). The coupling effects of heavy rainfall with ASM can further reach 650 NTU for just a single hour (Figure 5-4C purple line; between 1st and 2nd hour).

Similarly, observations at the SWS-13 station along the junction of Camgat-Surong and Didipio Rivers, heavy rain added 300 NTU during one hour (Figure 5-4D). The impact of rain seems reasonably consistent between the three monitoring stations, taking into account both the light and heavy rain periods (Figure 5-4E). Figure 5-4F shows relatively little variation in turbidity at a site near downstream of gold panning. Overall, the analysis shows that there is some time-variations of turbidity associated with mining activity without rainfall, this variation was small compared to the effects of rainfall, and one observation implied the greatest time variation was due to rainfall coinciding with mining activity.

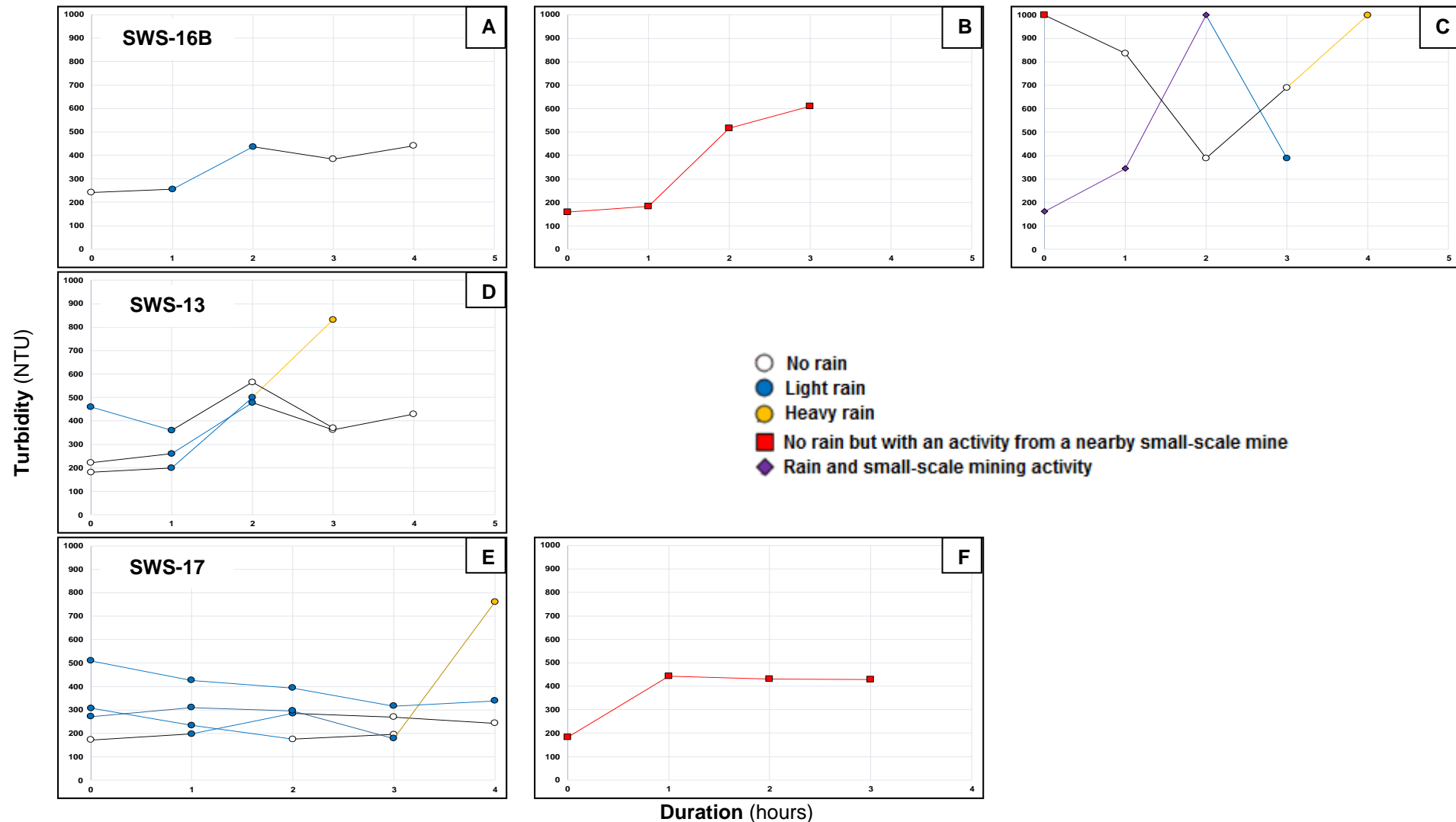
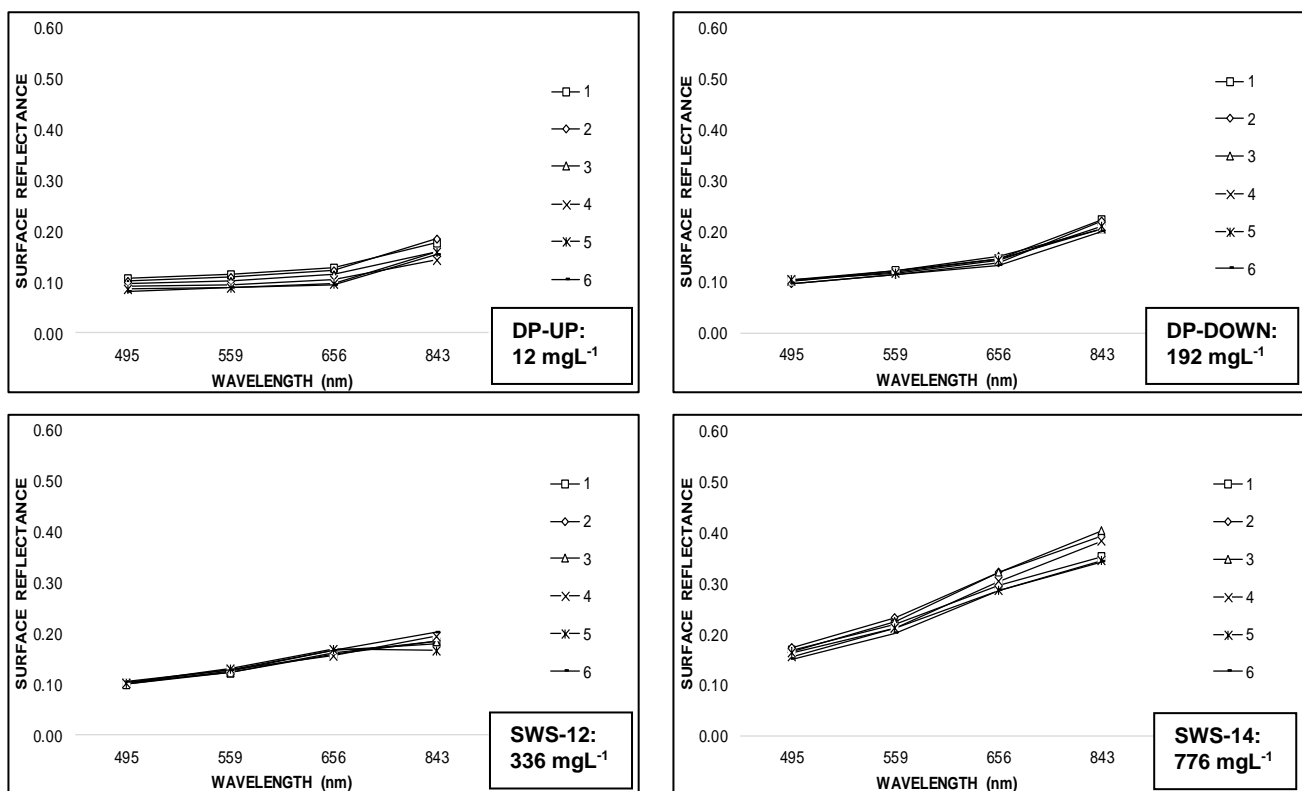


Figure 5-4: Plot of hourly monitoring of river turbidity during the early phase of the wet season in the Didipio case study
 (Note that each line corresponds to a set of observations collected within a single day)

5.2.2 Relationship between TSS and surface reflectance

Figure 5-5 shows that the magnitude of surface reflectance is similar over the six test pixels at each station (Table 5-3). The obtained spectral signatures for lower TSS concentration (e.g. from 12 mgL^{-1} of 2013 DP-UP to 25 mgL^{-1} of 2014 SWS-12) have minor reflectance variation in the visible bands whereas high surface reflectance values in the near-infrared band is observable (Figure 5-5). The spectral signature of moderately clear water on these sections of the river were compared with the spectral signature of pure clear water from deep rivers in the catchment. Based on the observation, the surface reflectance of clear water has the lowest reflectance in the near-infrared band. Whereas the inclusion of river stones within a pixel, which are visible in the image, increases the detected surface reflectance in the near-infrared band. Therefore, the noticeable higher reflectance in near-infrared band of DP-UP and SWS-12 in 2013 and 2014 images, correspondingly, are attributed to objects such as rocks that protrude from the river's surface. In the images, minimum water flow is noticeable on these monitoring stations thus affect their water level. In contrast, the surface reflectance for TSS values from 192 mgL^{-1} to $3,580 \text{ mgL}^{-1}$ have observable increase in magnitude from visible bands to near-infrared band.



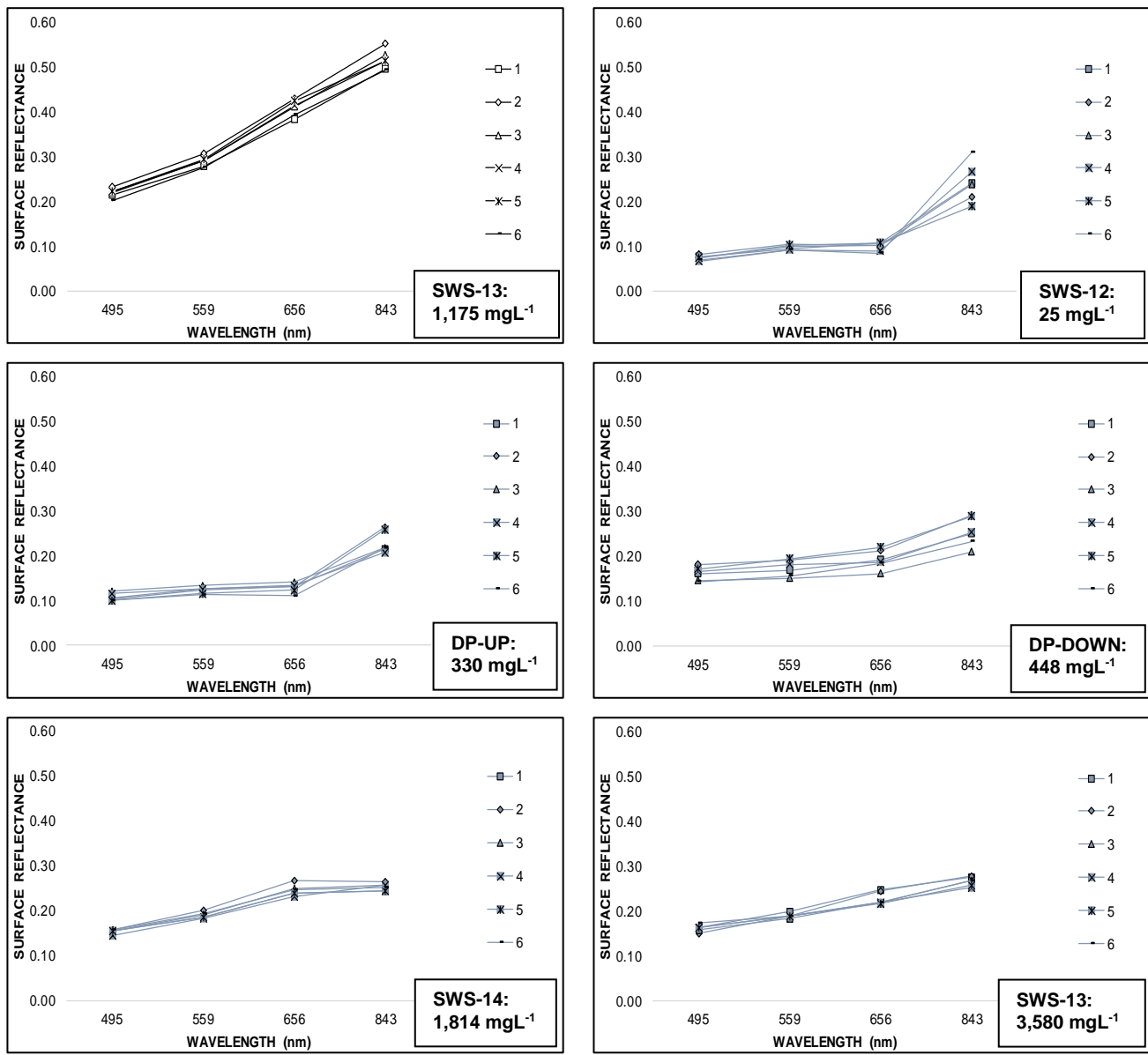


Figure 5-5: Plot of surface reflectance from the 6 adjacent pixels of each monitoring station
(a) 2013 image: black lines; (b) 2014 image: blue lines

Table 5-3: Surface reflectance values for each set of six test pixels

Stations	TSS	Surface Reflectance				TSS	Surface Reflectance				
		mgL ⁻¹	Blue band	Green band	Red band		mgL ⁻¹	Blue band	Green band	Red band	Near-infrared band
DP-UP	12	0.1084	0.1165	0.1299	0.1795	330	0.1073	0.1275	0.1325	0.2174	
		0.1022	0.1109	0.1242	0.1852		0.1042	0.1231	0.1314	0.265	
		0.0976	0.1026	0.1151	0.161		0.1216	0.133	0.1429	0.2179	
		0.0932	0.096	0.1059	0.1437		0.1154	0.1275	0.1354	0.2083	
		0.0872	0.0897	0.0965	0.1606		0.1002	0.1152	0.1247	0.2608	
		0.0826	0.0897	0.0948	0.155		0.1005	0.1127	0.1105	0.2177	
DP-DOWN	192	0.1043	0.1223	0.1468	0.224	448	0.1605	0.1679	0.1917	0.25	
		0.0973	0.1135	0.1385	0.221		0.1814	0.1916	0.2123	0.2917	
		0.1025	0.1213	0.151	0.204		0.1447	0.151	0.1595	0.2097	
		0.1022	0.1191	0.1456	0.204		0.1652	0.1805	0.1868	0.252	
		0.1043	0.1178	0.1436	0.2104		0.1692	0.1941	0.2192	0.288	
		0.0978	0.1147	0.1339	0.1999		0.1428	0.1537	0.1839	0.2316	
SWS-12	336	0.1043	0.1241	0.1602	0.1859	25	0.0762	0.0936	0.106	0.2401	
		0.1007	0.1279	0.1665	0.1795		0.0809	0.1046	0.1017	0.2089	
		0.1001	0.1254	0.1613	0.1859		0.0744	0.0977	0.102	0.237	
		0.1032	0.1284	0.1570	0.1953		0.0669	0.0904	0.0889	0.2653	
		0.1038	0.131	0.1699	0.1686		0.0737	0.1005	0.1068	0.1881	
		0.1053	0.1297	0.1665	0.2044		0.0675	0.0909	0.0838	0.3102	
SWS-13	1175	0.2152	0.2786	0.3834	0.4963	3580	0.1618	0.199	0.2479	0.2753	
		0.2312	0.3055	0.4283	0.5517		0.1496	0.1876	0.2455	0.2781	
		0.2186	0.2921	0.412	0.5279		0.1584	0.1843	0.2181	0.2685	
		0.2227	0.2903	0.4131	0.514		0.1618	0.1873	0.2203	0.2534	
		0.2207	0.2931	0.4243	0.5129		0.1627	0.1884	0.2168	0.2568	
		0.2013	0.2756	0.3923	0.4929		0.1733	0.1895	0.2187	0.2679	
SWS-14	776	0.169	0.2209	0.2961	0.3518	1814	0.1549	0.1843	0.238	0.2443	
		0.174	0.2333	0.3228	0.3929		0.1565	0.1996	0.2669	0.2648	
		0.1657	0.2249	0.3229	0.4035		0.1537	0.1914	0.2495	0.2577	
		0.1564	0.2113	0.3052	0.3843		0.145	0.184	0.2305	0.2562	
		0.1623	0.2118	0.2875	0.3450		0.1549	0.1843	0.238	0.2443	
		0.1505	0.2031	0.2869	0.3435		0.1562	0.1933	0.2479	0.2511	

The standard deviations of each set of six pixels are presented in Table 5-4. In the 2013 image, the standard deviation in blue and green bands ranges from 0.002 to 0.01 and from 0.005 to 0.02 for the red band. In contrast, higher standard deviations were observed in the near-infrared band, which ranges from 0.01 to 0.03 with which, the highest variation occurred in the SWS-14 station. Similar trend was observed in SWS-12, DP-DOWN and DP-UP stations of the 2014 image (0.01 to 0.04). However, the inter-station and inter-year variability in standard deviation can be said to be minimal.

Table 5-4: Mean surface reflectance for each corresponding value of total suspended solids/Turbidity: 30 March 2013 Pleiades-1A image, 5 May 2014 Pleiades-1A image

Stations	Blue band		Green band		Red band		NIR band		TSS mgL^{-1}
	495 nm	Ref σ	559 nm	Ref σ	656 nm	Ref σ	843 nm	Ref σ	
Year: 2013									
DP-UP	0.0952	0.01	0.1009	0.01	0.1111	0.01	0.1642	0.02	12
DP-DOWN	0.1014	0.003	0.1181	0.004	0.1432	0.01	0.2106	0.01	192
SWS-12	0.1029	0.002	0.1278	0.003	0.1636	0.005	0.1866	0.01	336
SWS-13	0.2183	0.01	0.2892	0.01	0.4089	0.02	0.5160	0.02	1,175
SWS-14	0.1630	0.01	0.2176	0.01	0.3036	0.02	0.3702	0.03	776
Year: 2014									
DP-UP	0.1082	0.01	0.1232	0.01	0.1296	0.01	0.2312	0.02	330
DP-DOWN	0.1606	0.01	0.1731	0.02	0.1922	0.02	0.2538	0.03	448
SWS-12	0.0733	0.01	0.0963	0.01	0.0982	0.01	0.2416	0.04	25
SWS-13	0.1613	0.01	0.1894	0.01	0.2279	0.01	0.2667	0.01	3,580
SWS-14	0.1535	0.004	0.1895	0.01	0.2451	0.01	0.2531	0.01	1,814

The separate mean surface reflectance from each spectral band in 2013 and 2014 were plotted against the datasets of TSS. Although nonlinear relationships between surface reflectance and TSS at higher ranges of TSS are likely, the limited dataset available did not allow this to be explored. Based on the separate plots, mean surface reflectance values for each set satisfactory follow increasing trend as TSS increases (Figure 5-6). A satisfactory R^2 for the case study validates the adequacy of the generated regression model to represent TSS measurement variation at all field conditions using either single or multiple satellite images. In addition, satisfactory R^2 maintains the least possible disagreement between the observed and predicted values of TSS measurements (Ryan, 2007). The aim of the study is to capture all the possible range of TSS measurement levels in the catchment given the available data. The separate linear equations between TSS and surface reflectance in each band from the two separate images were determined and are listed in Table 5-5. Based on these equations, coefficient of determination (R^2) in the 2013 image is highest in the red band and followed by the green band. However, it can be concluded that blue band and near-infrared band also have satisfactory R^2 . On the other hand, red and near-infrared bands have the highest R^2 in the 2014 image at 58% and 67%, respectively.

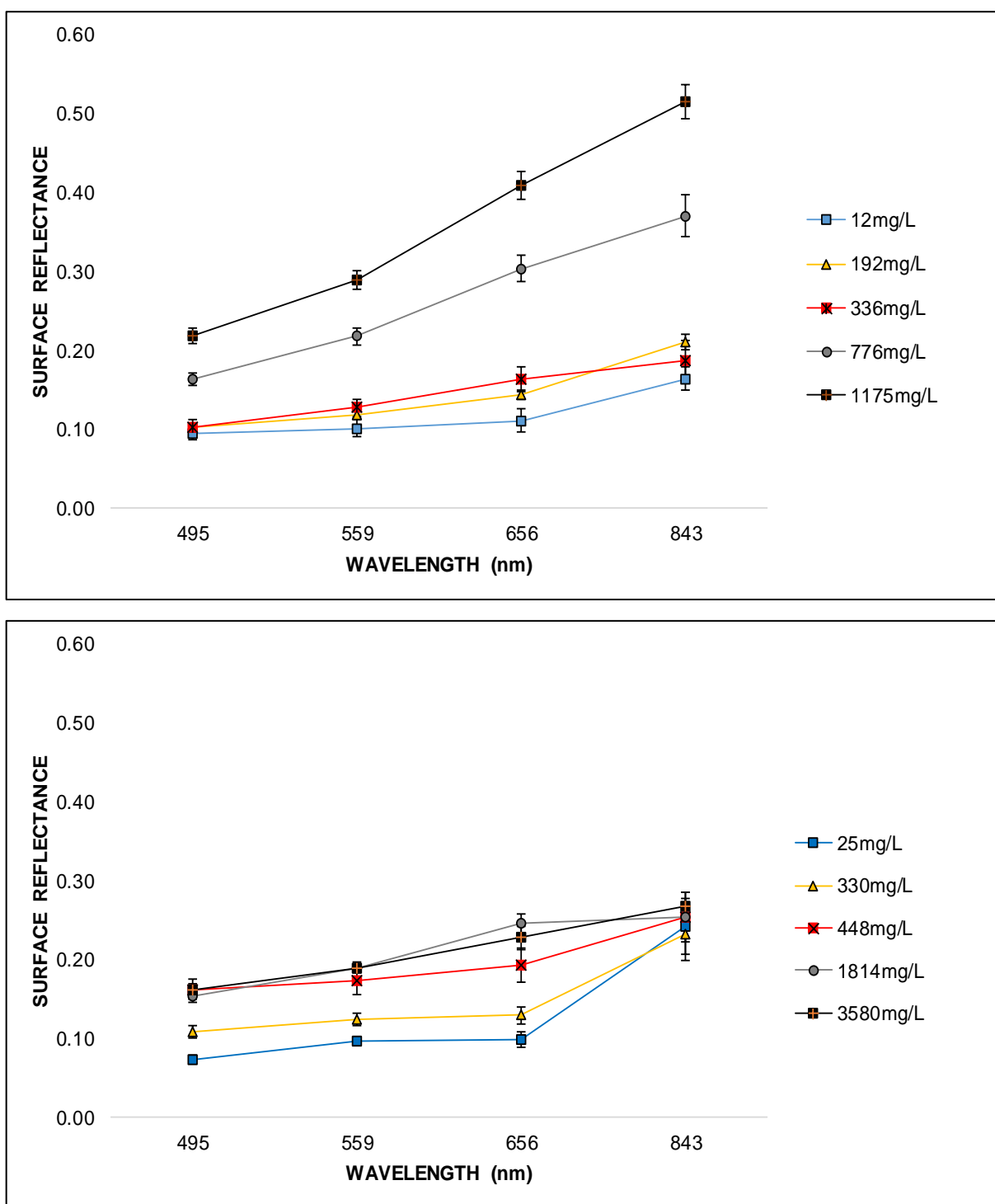


Figure 5-6: Spectral signatures of water with suspended solids (a) 2013; (b) 2014
 (Note that error bars correspond to standard deviations of mean surface reflectance in each spectral band)

Table 5-5: Linear equations generated for TSS and surface reflectance relationship in each band

Year	Band	Equation			Coefficient of Determination (R^2)	RMSE
		m	b	%		
2013	495	Blue	8,641	-678	96	85
	559	Green	5,841	-499	98	53
	656	Red	3,732	-345	99	41
	843	NIR	3,072	-391	96	89
2014	495	Blue	24,566	-1,988	43	1,002
	559	Green	26,008	-2,773	55	883
	656	Red	17,915	-1,960	58	852
	843	NIR	89,870	-21,162	67	760

The separate plots of mean surface reflectance values in Figure 5-6 were combined in Figure 5-7 to determine the overall trend between TSS and surface reflectance values. Based on the result, TSS at higher concentration level, which include SWS-13 ($1,814 \text{ mgL}^{-1}$) and SWS-14 ($3,580 \text{ mgL}^{-1}$) as measured from the 2014 image, has lower surface reflectance in all spectral bands when compared with their counterpart readings (1175 mgL^{-1} and 776 mgL^{-1}) in the 2013 image (highlighted in red boxes). The difference in the TSS-reflectance relationship, and the difference in the spectral signature between the two years may be explained by changes in the sources of sediments. When the Pleiades-1A images were visually evaluated, a brightness difference in high TSS rivers can be perceived. The turbid water in 2014 image is muddy (darker) in all stations compared with the turbid water in 2013 image. Normally, sediments that are generated from soil types at deeper layers appear brighter than those generated from in or near the topsoil due to smaller particle size (e.g. clay, loose sands). It was concluded that sediments with larger particle size have lower surface reflectance when evaluated against fine particles with similar magnitude of TSS (Bhargava & Mariam, 1991). Based on the image classification in Chapter 4, Section 4.4.3, there was an increase of $30,000 \text{ m}^2$ in the overall coverage of ASM in the catchment from 2013 to 2014. In addition, there were developments of small-scale mines and foot roads in the regions of Camgat River and south of upper Didipio River in the 2014 image; therefore, topsoil of coarser particle size can be the main source of sediments. Moreover, other interference may due to surface reflectance values that represent the pixel scale properties, whereas the samples of TSS are from points in the river; therefore, the disparity in scale may create some noise.

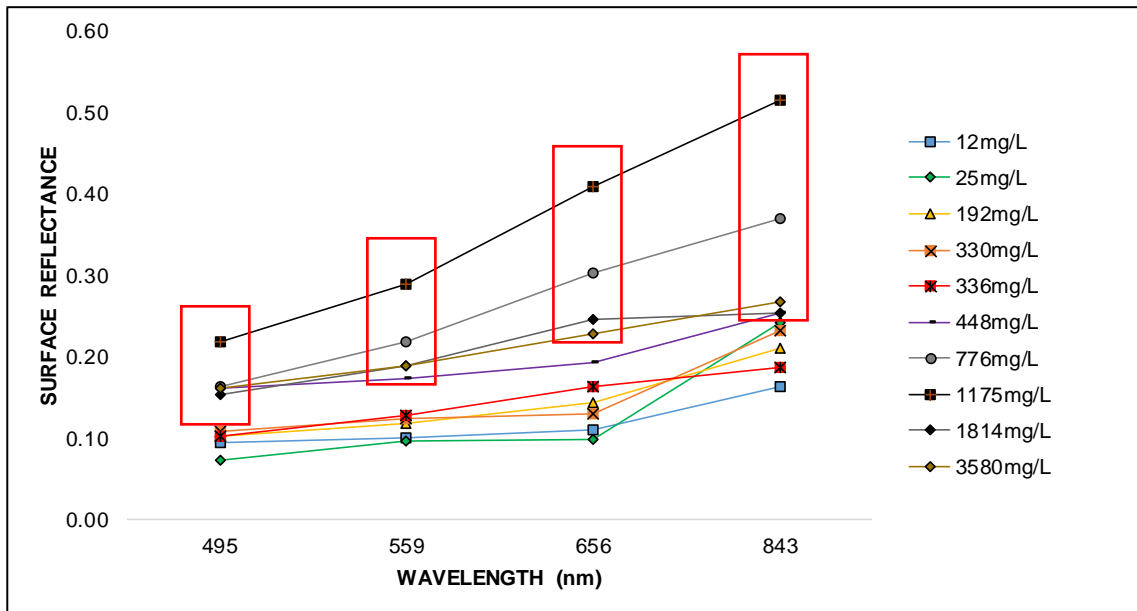


Figure 5-7: Spectral signatures corresponding to different measured TSS concentrations
(The red boxes show the irregularities in surface reflectance for TSS values from 776 mgL^{-1} to $3,580 \text{ mgL}^{-1}$)

Although the sediments are thought to largely come from the same land use feature (ASM), but with different soil sources, their combined behavior still must be captured by a single hydrological model. If the rivers of the catchment sit over dark river bottoms, it can be concluded that surface reflectance in the red band can be purely attributed to TSS as the river bottom can have higher reflectance than TSS in blue and green bands only. In addition, the use of the near-infrared band in the model is not quite applicable due to interference from river constituents such as protruding rocks when running water is minimal; therefore, it can be concluded that the use of the near-infrared band in shallow rivers with depth below 30 cm is only effective at higher TSS measurement levels (e.g. 100 mgL^{-1} and above). Through the application of a linear model, the resulting coefficient of determination in the red band is 20% only (Figure 5-8). The computed RMSE is 937 mgL^{-1} for the combined results of 2013 and 2014 images. Steep trend lines were obtained for the blue and green bands; therefore, a minimal increase in surface reflectance can be observed for every unit increase in TSS in these bands. On the other hand, gentle trend lines were produced for the red and near-infrared bands.

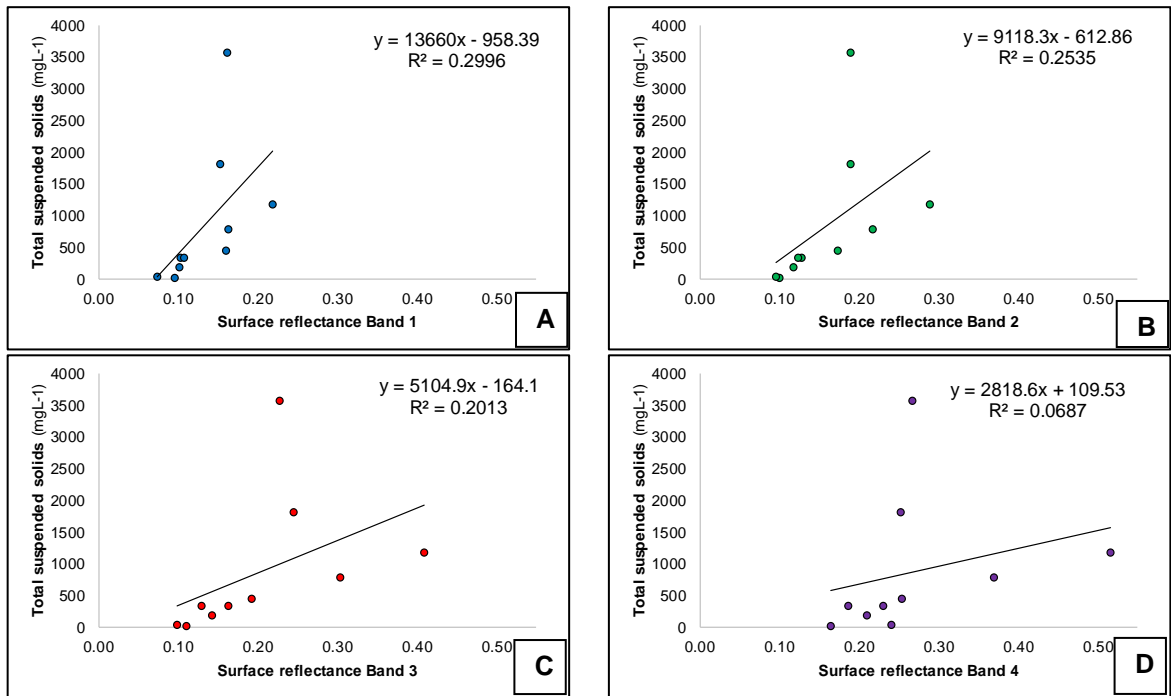
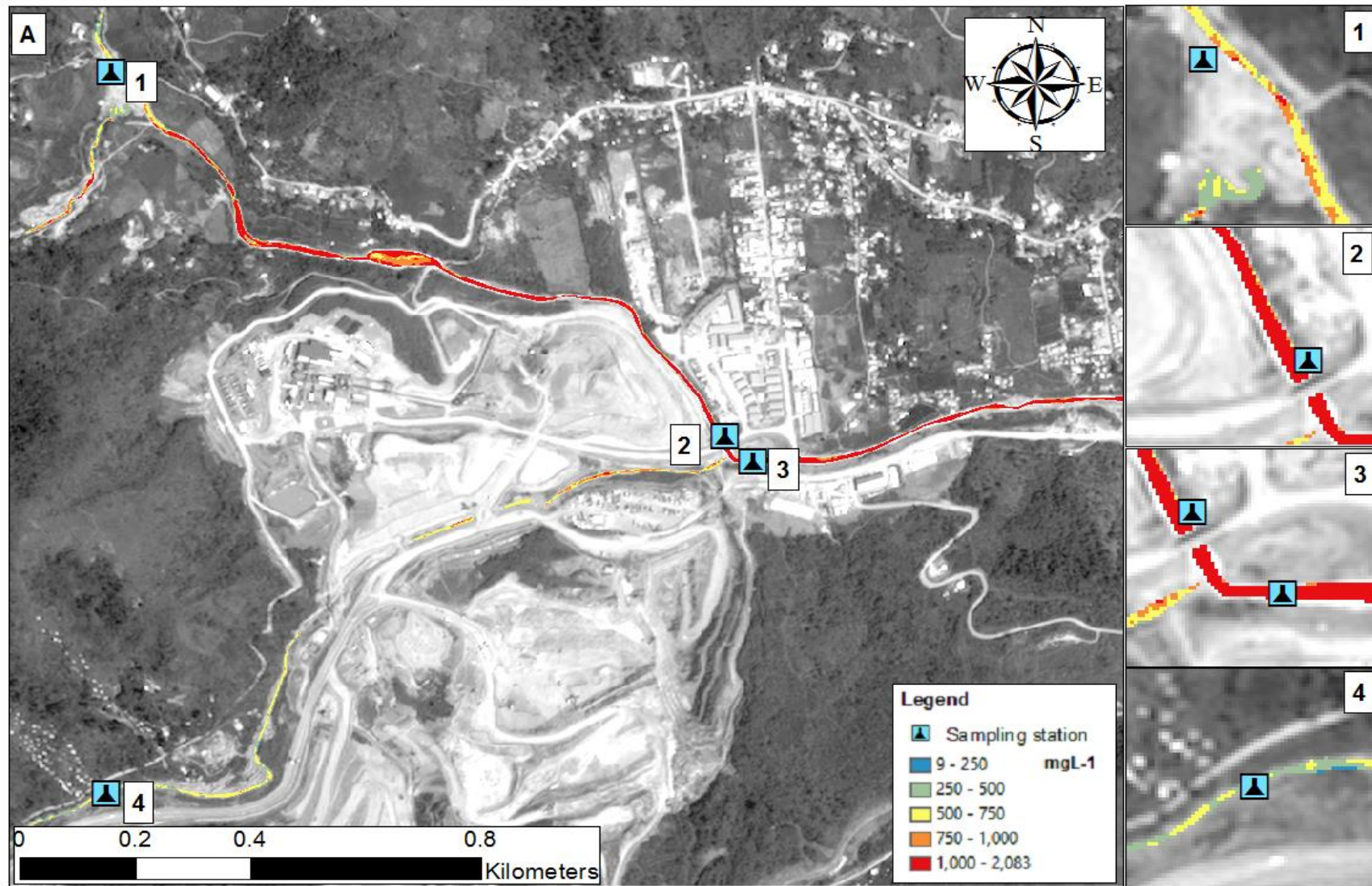


Figure 5-8: Graphs of total suspended solids against band reflectance for 2013 Pleiades-1A images:
(a) Blue band; (b) Green band; (c) Red band; and (d) Near-infrared band

$$\text{TSS}_{2013,2014} = 5,105R_{\text{BAND}3} - 164 \quad ; R^2 = 0.20 \quad (5.4.1)$$

The univariate equation that include the red band does not have the highest R^2 if data from the 2013 and 2014 images are merged however, it has high R^2 at 96% if the TSS-reflectance point values of SWS-13 and SWS-14 from the 2014 image are excluded in the equation. Provided the high TSS values of the rivers in Didipio catchment, the surface reflectance variation in the red band can be attributed only to addition of suspended sediments into the river. Equation 5.4.1 represents ASM both during development phase (e.g. stripping of vegetated areas and topsoil are the dominant activities) and normal operation. The option to improve Eq. 5.4.1 depends on securing additional observations, in particular to incorporate TSS measurements higher than $3,600 \text{ mgL}^{-1}$ to determine the actual data relationship other than being linearly related at lower TSS values. For the available datasets, there are only three samples with TSS values of greater than $1,000 \text{ mgL}^{-1}$. The model equation was utilised to calibrate the available Pleiades-1A images separately, and thematic maps that show the ranges of TSS measurements in each section of the catchment were produced (Figure 5-9).



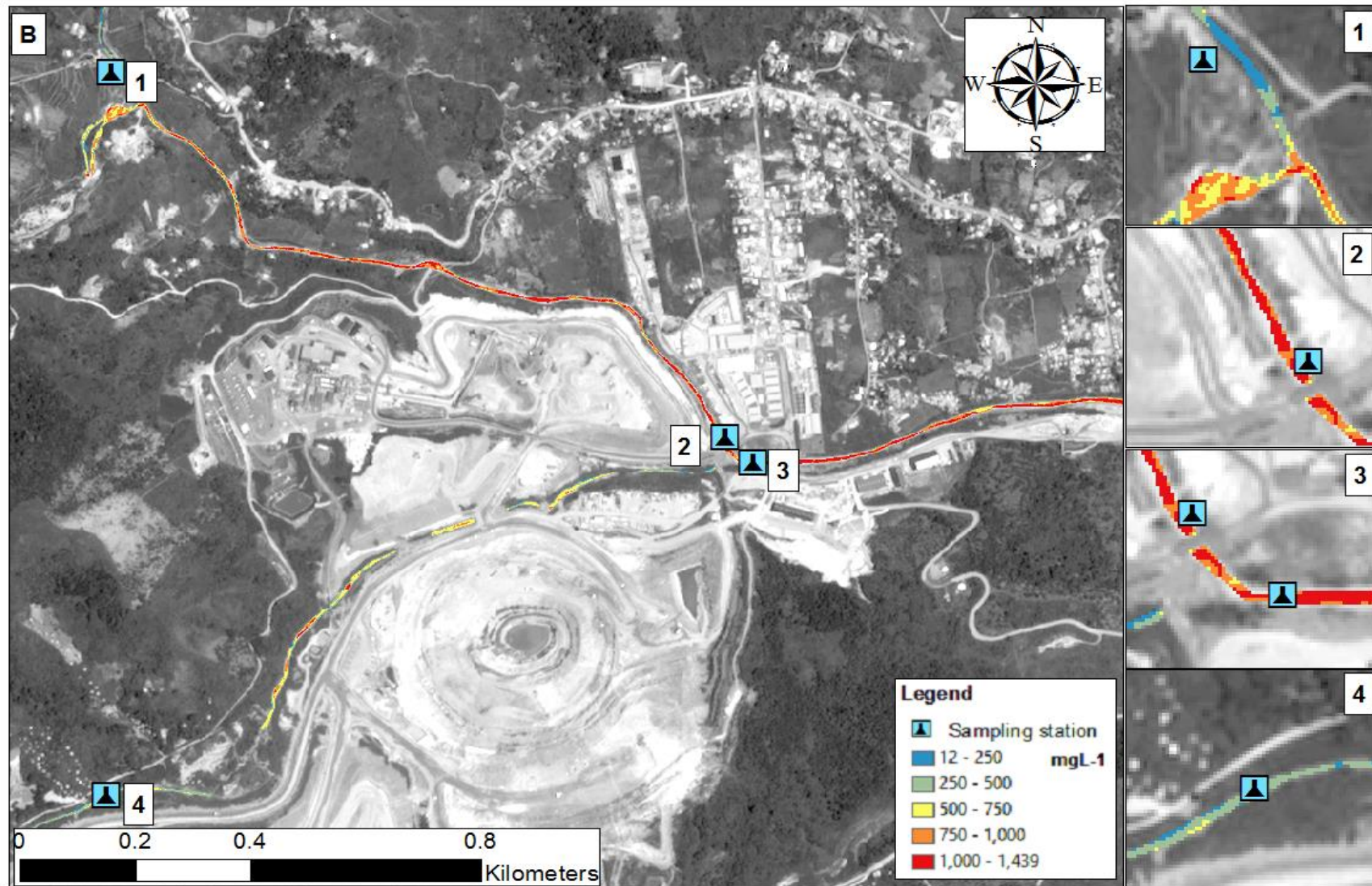


Figure 5-9: Calibrated thematic maps of surface reflectance with corresponding measurement level of TSS
 (a) 2013 Pleiades-1A; (b) 2014 Pleiades-1A

The mapping of modeled TSS values is divided into intervals of 250 mgL^{-1} (Figure 5-9). In 2013 and 2014 thematic maps, the upper Dinauyan is presented mostly in blue and green pixels, which correspond to the lower range of TSS measurement levels. This is most likely because Dinauyan upstream is only surrounded by sites for gold panning that seldom operate, and the other segments of the river are completely surrounded by grassland. In contrast, a hydraulic small-scale mine operates at Dinauyan downstream, and may deliver a higher level of TSS to DP-DOWN and SWS-12 monitoring stations, which are shown in mix of yellow, orange and red pixels in 2013 thematic map; and a mix of mostly green to yellow pixels in the 2014 thematic map. Moreover, Surong has an observable high TSS in the 2013 thematic map as shown in yellow pixels. These yellow pixels reflect the impact of the sediment pit beside the river's discharge. In the 2014 thematic map, a clear water is apparent coming from Surong water (blue pixels). In contrast, Camgat-Surong and Didipio rivers consistently exhibit moderate level (yellow pixels) to high level (red pixels) of TSS for two years, which may be triggered by gold panning from the upstream and downstream of the river and by an underground mine at the middle stream. Camgat portrays better water quality in 2013 (green pixels), but moderate TSS values (yellow and orange pixels) are noticeable in the 2014 thematic map. In general, Camgat, Didipio and Camgat-Surong seem to be the rivers most impacted by ASM in the catchment. It can be said that such thematic maps of TSS can be useful at regional scale of analysis. Likewise, they may be suitable for examining potential TSS concentrations away from the monitoring stations, and understand the fate and transport of sediments towards the downstream of the catchment.

For this model of Didipio catchment, it can be said that it may be used to estimate TSS concentrations up to a certain limit only (12 mgL^{-1} to $3,580 \text{ mgL}^{-1}$). However, small-scale mines in the catchment were documented to produce TSS as high as $32,060 \text{ mgL}^{-1}$. The analysis was restricted by the information that was provided by the cloud-free images with corresponding TSS measurements.

5.3 Summary

With the application of a linear regression model, Pleiades-1A satellite images were calibrated into thematic maps that present measured TSS throughout the selected rivers of the Didipio catchment. For this study, TSS, turbidity and surface reflectance are all linearly related. TSS has high coefficient of determination at 626 nm (the red band) for the separate models of the 2013 and 2014 images, but for the model that was used, the R^2 is 20% only. The generated R^2 for each plot of TSS and surface reflectance in each spectral band (combined 2013 and 2014 datasets) is comparable for all spectral bands except for the lower R^2 in the near-infrared band. The co-linearity of surface reflectance between the visible bands meant that it is enough to choose a single spectral band that gives the

highest R^2 value, but which is free from the potential influence of the dark bottom of the river, as the model input.

The model can assist in spatial analysis of the effect of land use features on river water quality, including those features that are distant from water quality monitoring stations. However, the model is restricted by the underlying measurement ranges and soil sources that produced the linear relationships of TSS with surface reflectance in the red band. Other dominant sources of sediments may lead to a different linear relationship, and other ranges of TSS may require a different mathematical equation (e.g. exponential, second-degree polynomial). It may be more accurate to determine the relationship between TSS and surface reflectance for a greater range of dominant land use features as well as wider TSS ranges.

Chapter 6 Conclusions and recommendations

6.1 Conclusions

6.1.1 Environmental importance of Didipio catchment

The Didipio catchment offers several ecosystem services to its communities. Firstly, an average of 1.20 km² of perennial crops utilise selected rivers for irrigation. Secondly, there is a potential growth of different species of plants and trees within the 24 km² of forest. Lastly, the catchment rests over an extended mineralised land within which mining activities are found. The six main rivers of the catchment, which are included in this study, not to mention downstream rivers such as the Alimit, were classified as Class D rivers by the Department of Environment and Natural Resources (DENR). Class D rivers are principally used for industrial purposes. Although high concentrations of total suspended solids can be observed on these rivers, they still have other water qualities that are within the standard limit, which make these rivers appropriate to support existing land uses in Didipio.

6.1.2 The applicability of remote sensing to identifying artisanal and small-scale mining land footprints in the context of wet tropical regions

The application of remote sensing supports the analysis of both the spatial and temporal dimensions of ASM. Pleiades-1A and SPOT-6 have their respective identical satellites (e.g. Pleiades-1B and SPOT-7) that revolve in the same orbital plane. Each satellite pair can produce coherent image products with similar data resolutions; therefore, decreasing the image acquisition period between 1 to 2 days. This structure is advantageous to wet tropical regions as it increases the probability to secure cloud-free images. With the application of an object-based approach in image classification, mining features at a certain spatial scale are detectable, and their classification attributes are potentially well represented by analysis of several segments, which are sets of homogeneous pixels of comparable spatial, spectral and textural attributes. For the case study of Didipio, the overall coverage (less than a square kilometre) of ASM can still be considered underdeveloped if it is compared with other ASM regions, which extend to square kilometres in size such as those found in Tapajos River Basin in Brazilian Amazon (Lobo et al., 2016), Democratic Republic of Congo and (Luethje et al., 2014), Upper Mazaruni, Guyana (Mengisteab et al., 2015). In this research, the efficacy of Pleiades-1A and SPOT-6 satellites on the classification of land use features in Didipio was demonstrated, and supported by the obtained overall accuracy (89% for SPOT-6 while 87-89%

for Pleiades-1A). It is anticipated that Pleiades-1A and SPOT-6 can better classify ASM regions at larger scale from the other catchments.

6.1.3 The applicability of remote sensing to identifying variations in water quality in the context of wet tropical regions

Remote sensing can provide a model of total suspended solids (TSS) concentrations in the Didipio catchment. The red channel reflectance alone can accurately estimate the TSS concentration of each river, within the range of concentrations used to develop the model. However, the obtained root mean square error for the combined dataset in 2013 and 2014 images was 937 mgL^{-1} due to constructions of additional small-scale mines in the catchment that produces different soil type as source of suspended sediments. Aside from the near infrared region, the red channel is a spectral channel where dark river bottom has no influence on surface reflectance. The reliability of the model can be improved through the addition of more pairs of reflectance-TSS measurements within the TSS range of the previously applied dataset. Moreover, the applicability of the model can be improved if reflectance-TSS measurements outside this TSS range are incorporated in the equation.

6.2 Recommendations

Future works should focus on other ASM regions with lower cloud cover, which would permit more exploration of seasonal changes, and suitability of satellite products. It is worthwhile to test if a database can be produced on the possible spatial and spectral attributes of small-scale mines from different regions. The value of this effort can determine whether if these attributes are highly dependent on the mineralisation and local geology of a mining area and the phase of mining. For this research, the generated spatial and spectral attributes are constrained within the context of small-scale mining in non-sulfuric gold ore deposit as discussed in Section 2.3.2. In contrast, small-scale mines in regions with sulfuric gold ore deposits can instigate acid mine drainage due to high weathering rate of sulfide-bearing minerals, which may produce different spectral features.

At this moment, there are several initiatives to improve both data resolution of satellite products as well as developing the existing image analysis techniques. Recently, Sentinel-2 has become accessible for public use. Sentinel-2 is composed of 13 spectral bands within which the four principal spectral regions (e.g. blue, green, red, and near-infrared) have a spatial resolution of 10 m (Drusch, et al., 2012). It would be valuable to explore what reliability could be obtained from this product for different scales of mining. In addition, it may also be valuable to examine the contribution of the

thermal bands provided by other satellites in increasing the classification accuracy of land use features (Sun & Schulz, 2015). Landsat-8 offers spectral bands in the thermal region, but its spatial resolution (15 m) may preclude applicability to the scale of ASM found in the case study.

For the current case study and imageries, supplementary analyses can be performed on the following aspects;

- Continued sampling to build up the database and improve reliability and applicability of the model.
- Evaluation of potential influence of particle size from the sediment yields of various land use features to surface reflectance at different levels of total suspended solids.
- A statistical database on the contribution of various land use features to water turbidity.

List of References

- Adler-Golden, S. M., Bernstein, L. S., Gregor, B., & Jin, X. (2012). Quick atmospheric correction code: algorithm description and recent upgrades. *Optical Engineering*, 51(11), 111719-1-111719-11. doi:10.1117/1.OE.51.11.111719
- Adler-Golden, S. M., Bernstein, L. S., Matthew, M. W., Sundberg, R. L., & Ratkowski, A. J. (2007). Atmospheric compensation of extreme off-nadir hyperspectral imagery from Hyperion. *SPIE Proceeding, Algorithms and Technologies for Multispectral, Hyperspectral and Ultraspectral Imagery XIII*, 6565. doi:10.1117/12.721769
- AECOM Philippines Incorporated. (2013). *Ecological Assessment for Didipio Gold-Copper Project*. AECOM Philippines Incorporated, Ecology Team.
- Al-Fares, W. (2013). *Historical Land Use/Land Cover Classification Using Remote Sensing: A Case Study of the Euphrates River Basin in Syria*. New York: Springer.
- Amro, I., Mateos, J., Vega, M., Molina, R., & Katsaggelos, A. (2011). A survey of classical methods and new trends in pansharpening of multispectral images. *EURASIP Journal on Advances in Signal Processing*, 79, 1-22.
- Appleton, J. D., Williams, T. M., Breward, N., Apostol, A., Miguel, J., & Miranda, C. (1999). Mercury contamination associated with artisanal gold mining on the island of Mindanao, Philippines. *The Science of the Total Environment*, 228, 95-109. doi:10.1016/S0048-9697(99)00016-9
- Astrium. (2012). *Pleiades Imagery User Guide*.
- Astrium. (2013). *SPOT 6 & SPOT 7 Imagery User Guide*.
- Astronomical Applications Department of the U.S. Naval Observatory. (2016). *Julian Data Converter*. Retrieved from Astronomical Applications Department of the U.S. Naval Observatory: <http://aa.usno.navy.mil/data/docs/JulianDate.php>
- Atherholt, T. B., LeChevallier, M. W., Norton, W. D., & Rosen, J. S. (1998). Effect of rainfall on Giardia and crypto. *American Water Works Association*, 90(9), 66. Retrieved from <http://search.proquest.com/openview/c6751a5ec62d71a65395ba393dfde172/1?pq-origsite=gscholar&cbl=25142>
- Baker, E. T., William, & J, L. (1984). The effect of particle size on the light attenuation coefficient of natural suspensions. *Journal of Geophysical Research*, 89(C5), 8197-8203. doi:10.1029/JC089iC05p08197
- Bansuan, A. M., Goater, S. E., Danoucaras, A. N., & Hearne, D. (2012). Integrated Sustainable Water Management in Mining for Development in the Philippines. *International Mine Management Conference*, (pp. 1-22). Melbourne.
- Barrett, E. C., & Curtis, L. F. (1999). *Introduction to Environmental Remote Sensing* (4th ed.). New York, United States of America: Taylor & Francis Group. Retrieved December 30, 2016
- Bayram, A., & Kenanoglu, M. (2016). Variation of total suspended solids versus turbidity and Secchi disk depth in the Borcka Dam Reservoir, Coruh River Basin, Turkey. *Lake and reservoir*

management, 32(3), 209-224. Retrieved from
<http://dx.doi.org/10.1080/10402381.2016.1160168>

Benedini, M., & Tsakiris, G. (2013). Basic Notions. In M. Benedini, & G. Tsakiris, *Water Quality Modelling for Rivers and Streams* (Vol. 70, pp. 11-26). New York, United States: Springer. doi:10.1007/978-94-007-5509-3_2

Bernstein, L. S., Jin, X., Gregor, B., & Adler-Golden, S. M. (2012). Quick atmospheric correction code: algorithm description and recent upgrades. *Optical Engineering*, 51(11), 111719-1-111719-11. doi:10.1117/1.OE.51.11.111719

Bhargava, D. S., & Mariam, D. W. (1991). Light penetration depth, turbidity and reflectance related relationships and models. *Journal of Photogrammetry and Remote Sensing*, 46, 217-230.

Blaschke, T. (2010). Object based image analysis for remote sensing. *ISPRS Journal of Photogrammetry and Remote Sensing*, 65(1), 2-16. doi:doi:10.1016/j.isprsjprs.2009.06.004

Bugnosen, E. M. (2001). *Country Case Study on Artisanal and Small-scale Mining: Philippines*. International Institute for Environment and Development (IIED), World Business Council for Sustainable Development, London, England. Retrieved March 6, 2017, from <http://pubs.iied.org/pdfs/G00732.pdf>

Butt, A., Shabbir, R., Ahmad, S. S., & Aziz, N. (2015). Land use change mapping and analysis using Remote Sensing and GIS: A case study of Simly watershed, Islamabad, Pakistan. *The Egyptian Journal of Remote Sensing and Space Sciences*, 18(2), 251-259. Retrieved from <http://dx.doi.org/10.1016/j.ejrs.2015.07.003>

Campbell, J. B., & Wynne, R. H. (2011). *Introduction to Remote Sensing* (5th ed.). New York, United States: The Guilford Press.

Canada, N. R. (2015). *Geometric Distortion in Imagery*. Retrieved from Natural Resources Canada: <http://www.nrcan.gc.ca/node/9401>

Canada, N. R. (no date). *Fundamentals of Remote Sensing*. Retrieved from Natural Resources Canada:

https://www.nrcan.gc.ca/sites/www.nrcan.gc.ca/files/earthsciences/pdf/resource/tutor/fundam/pdf/fundamentals_e.pdf

Chander, G., Markham, B. L., & Helder, D. L. (2009). Summary of current radiometric calibration coefficients for Landsat MSS, TM, ETM+, and EO-1 ALI sensors. *Remote Sensing of Environment*, 113(5), 893-903. Retrieved from <https://doi.org/10.1016/j.rse.2009.01.007>

Chin, L. S. (2001). *Interpreting Optical Remote Sensing Images*. (National University of Singapore) Retrieved January 29, 2016, from Centre for Remote Imaging, Sensing & Processing (CRISP): http://www.crisp.nus.edu.sg/~research/tutorial/opt_int.htm

Cihlar, J. (2000). Land cover mapping of large areas from satellites: Status and research priorities. *International Journal of Remote Sensing*, 21(6-7), 1093-1114. doi:10.1080/014311600210092

Colditz, R. R., Wehrmann, T., Bachmann, M., Steinnocher, K., Schmidt, M., Strunz, G., & Dech, S. (2006). Influence of image fusion approaches on classification accuracy: a case study. *International Journal of Remote Sensing*, 27(15), 3311-3335. doi:10.1080/01431160600649254

- Congalton, R. G. (1991). A Review of Assessing the Accuracy of Classifications of Remotely Sensed Data. *Remote Sensing of Environment*, 37, 35-46.
- Cordy, P., Veiga, M. M., Salih, I., Al-Saadi, S., Console, S., Garcia, O., . . . Roeser, M. (2011). Mercury contamination from artisanal gold mining in Antioquia, Colombia: The world's highest per capita mercury pollution. *Science of the Total Environment*, 410-411, 154-160. Retrieved from <http://dx.doi.org/10.1016/j.scitotenv.2011.09.006>
- Crippen, R. E. (2007). The regression intersection method of adjusting image data for band rationing. *International Journal of Remote Sensing*, 8(2), 137-155. doi:10.1080/01431168708948622
- Davis, A. P., & McCuen, R. H. (2005). Water Quality Parameters. In A. P. Davis, & R. H. McCuen, *Stormwater Management for Smart Growth*. Springer US. doi:10.1007/0-387-27593-2
- Dekker, A. G., & Hestir, E. L. (2012). *Evaluating the Feasibility of Systematic Inland Water Quality Monitoring with Satellite Remote Sensing*. CSIRO: Water for a Healthy Country National Research Flagship.
- Dekker, A. G., Vos, R. J., & Peters, S. W. (2001). Comparison of remote sensing data, model results and in situ data for total suspended matter (TSM) in the southern Frisian lakes. *The Science of the Total Environment*, 268, 197-214.
- Department of Environment and Natural Resources. (2011). *Formulation of Integrated Cagayan River Basin Management and Development Master Plan*. Executive Summary, River Basin Control Office, Department of Environment and Natural Resources (DENR), Cagayan, Philippines. Retrieved January 25, 2017
- Dikshit, O., & Roy, D. P. (1996). An Empirical Investigation of Image Resampling Effects Upon the Spectral and Textural Supervised Classification of a High Spatial Resolution Multispectral Image. *Photogrammetric Engineering and Remote Sensing*, 62(9), 1085-1092. doi:0099-1112/96/6209-1085
- Dorigo, W. A., Zurita-Milla, R., de Wit, A., Brazile, J., Singh, R., & Schaepman, M. (2007). A review on reflective remote sensing and data assimilation techniques for enhanced agroecosystem modelling. *International Journal of Applied Earth Observation and Geoinformation*, 9(2), 165-193. Retrieved from <https://doi.org/10.1016/j.jag.2006.05.003>
- Dorji, P., Fearn, P., & Broomhall, M. (2016). A Semi-Analytic Model for Estimating Total Suspended Sediment Concentration in Turbid Coastal Waters of Northern Western Australia Using MODIS-Aqua 250 m Data. *Remote sensing*, 8(556), 1-23. doi:10.3390/rs8070556
- Drusch, M., Del Bello, U., Carlier, S., Colin, O., Fernandez, Z., Gascon, F., . . . Bargellini, P. (2012). Sentinel-2: ESA's Optical High-Resolution Mission for GMES Operational Services. *Remote Sensing of Environment*, 25-36.
- Duro, D. C., Franklin, S. E., & Dube, M. G. (2012). A comparison of pixel-based and object-based image analysis with selected machine learning algorithms for the classification of agricultural landscapes using SPOT-5 HRG imagery. *Remote Sensing of Environment*, 118, 259-272. doi:10.1016/j.rse.2011.11.020
- Eneji, I. S., Onuche, A. P., & Sha'Ato, R. (2012, July 25). Spatial and Temporal Variation in Water Quality of River Benue, Nigeria. *Journal of Environmental Protection*, 3, 915-921. Retrieved from <http://dx.doi.org/10.4236/jep.2012.328106>

Fondriest. (2016). *Turbidity, Total Suspended Solids & Water Clarity*. Retrieved from Fundamentals of Environmental Measurements: <http://www.fondriest.com/environmental-measurements/parameters/water-quality/turbidity-total-suspended-solids-water-clarity/#Turbid1>

Fong-Sam, Y. (2012). *The Mineral Industry of the Philippines*. United States Geological Survey (USGS), United States Department of the Interior. Retrieved March 30, 2017, from <https://minerals.usgs.gov/minerals/pubs/country/2010/myb3-2010-rp.pdf>

Gebreslasie, M. T., Ahmed, F. B., & van Aardt, J. A. (2010). Image-based reflectance conversion of ASTER and IKONOS imagery as precursor to structural assessment of plantation forests in KwaZulu-Natal, South Africa. *Southern Forests*, 71(4), 259-265. doi:10.2989/SF.2009.71.4.2.1029

George, D. G. (1997). The airborne remote sensing of phytoplankton chlorophyll in the lakes and tarns of the English Lake District. *International Journal of Remote Sensing*, 18(9), 1961-1975. doi:<http://dx.doi.org/10.1080/014311697217972>

Giri, C. P. (2012). Brief Overview of Remote Sensing of Land Cover. In C. P. Giri, *Remote sensing of Land Use and Land Cover* (pp. 3-12).

Gitelson, A., Garbuзов, G., Szilagyi, F., Mittenzwey, K.-H., Karnieli, A., & Kaiser, A. (1993). Quantitative remote sensing methods for real-time monitoring of inland waters quality. *International Journal of Remote Sensing*, 14(7), 1269-1295. doi:10.1080/01431169308953956

Goward, S. N., Masek, J. G., Williams, D. L., Irons, J. R., & Thompson, R. J. (2001). The Landsat 7 mission Terrestrial research and applications for the 21st century. *Remote Sensing of Environment*, 78(1-2), 3-12.

Halder, A., Ghosh, A., & Ghosh, S. (2011). Supervised and unsupervised landuse map generation from remotely sensed images using and based systems. *Applied Soft Computing*.

Han, D., Chan, L., & Zhu, N. (2007). Flood forecasting using support vector machine. *Journal of hydroinformatics*, 267-276. doi:10.2166/hydro.2007.027

Han, L., & Rundquist, D. (1996). Spectral characterization of suspended sediments generated from two texture classes of clay soil. *International Journal of Remote Sensing*, 17(3), 643-649. doi:10.1080/01431169608949034

Haralick, R. M., & Shapiro, L. (1985). Survey: Image segmentation techniques. *Computer Vision Graphics, and Image Processing*, 100-132.

Harrington Jr, J. A., Schiebe, F. R., & Nix, J. F. (1992). Remote sensing of Lake Chicot, Arkansas: Monitoring suspended sediments, turbidity, and Secchi depth withLandsat MSS data. *Remote Sensing of Environment*, 39(1), 15-27. Retrieved from [https://doi.org/10.1016/0034-4257\(92\)90137-9](https://doi.org/10.1016/0034-4257(92)90137-9)

Hentschel, T., Hruschka, F., & Priester, M. (2002). *Global Report on Artisanal & Small-scale Mining*. International Institute for Environment and Development (IIED), Mining, Minerals and Sustainable Development.

Hilson, G. M. (2005). *The Socio-Economic Impacts of Artisanal and Small-scale Mining in Developing Countries*. Netherlands: Taylor & Francis e-Library. Retrieved October 10, 2015,

from
https://books.google.com.au/books?id=7QNRVmjq5RsC&pg=PA525&lpg=PA525&dq=borax+use+to+remove+amalgam+impurities&source=bl&ots=wxJ_K68S_r&sig=1O-IRrg5c_41QP_4caw5vXDEgyQ&hl=en&sa=X#v=onepage&q=borax%20use%20to%20remove%20amalgam%20impurities&f=false

Hirons, M. (2014). Decentralising natural resource governance in Ghana: Critical reflections on the artisanal and small-scale mining sector. *Futures*, 62, 21-31.

Hopwood, D. (2013). *Status of Astrium GEO-Information Services' EO Satellite Constellation*. Retrieved February 13, 2017, from United States Geological Survey (USGS) Remote Sensing Technologies: <https://calval.cr.usgs.gov/wordpress/wp-content/uploads/Astrium-Constellation-Status.pdf>

Horiba, ltd. (2009). *Multi Water Quality Checker U-50 Series Instruction Manual*. Retrieved from <https://www.johnmorrisgroup.com/Content/Attachments/114441/99600-xx.pdf>

Horning, N., Robinson, J. A., & Sterling, E. A. (2010). *Remote Sensing for Ecology and Conservation: A Handbook of Techniques*. New York: Oxford University Press. Retrieved from https://books.google.com.au/books?id=0Z0UDAAAQBAJ&dq=why+only+three+bands+can+be+displayed+in+remote+sensing%3F&source=gbs_navlinks_s

Huang, C., Davis, L. S., & Townshend, J. R. (2002). An assessment of support vector machine for land cover classification. *International Journal of Remote sensing*, 23(4), 725-749. doi:10.1080/01431160110040323

Huang, W., Niu, Z., Tang, Q., & Wu, C. (2008, March 8). Estimating chlorophyll content from hyperspectral vegetation indices: Modeling and validation. *Agricultural and forest meteorology*, 148, 1230-1241.

Hughes, G. F. (1968). On the mean accuracy of statistical pattern recognition. *IEEE Transactions on Information Theory*, 14, 55-63. doi:10.1109/TIT.1968.1054102

Human Rights Watch. (2015, September 29). *Hazardous Child Labor in Small-Scale Gold Mining in the Philippines*. Human Rights Watch, New York, United States. Retrieved April 9, 2017, from Philippines: Children Risk Death to Dig and Dive for Gold: <https://www.hrw.org/report/2015/09/29/what-if-something-went-wrong/hazardous-child-labor-small-scale-gold-mining>

Hussain, M., Chen, D., Cheng, A., Wei, H., & Stanley, D. (2013). Change detection from remotely sensed images: From pixel-based to object-based approaches. *ISPRS Journal of Photogrammetry and Remote Sensing*, 80, 91-106. Retrieved February 13, 2017

Jensen, J. R. (1996). Thematic Information Extraction: Image Classification . In J. R. Jensen, *Introductory Digital Image Processing: A Remote Sensing Perspective (2nd Edition)* (pp. 197-256). Upper Saddle River, United States: Prentice Hall.

Johnson, B. (2014). Effects of Pansharpening on Vegetation Indices. *International Journal of Geo-Information*, 3, 507-522. doi:doi:10.3390/ijgi3020507

Kalkan, K., Bayram, B., Maktav, D., & Sunar, F. (2013). Comparison of support vector machine and object-based classification methods for coastline detection. *International Archives of the*

- Khorram, S., Nelson, S. A., Koch, F. H., & van der Wiele, C. F. (2012). *Remote Sensing*. New York, United States of America: Springer. doi:10.1007/978-1-4614-3103-9
- Koetz, B., Morsdorf, F., van der Linden, S., Curt, T., & Allgower, B. (2008). Multi-source land cover classification for forest fire. *Forest Ecological and Management*, 256(3), 263-271. doi:<https://doi.org/10.1016/j.foreco.2008.04.025>
- Kpalma, K., El-Mezouar, M. C., & Taleb, N. (2014). Recent Trends in Satellite Image Pan-sharpening Techniques. *HAL archives*. Retrieved from <https://hal.archives-ouvertes.fr/hal-01075703/document>
- Labonne, B. (2002). Commentary: Harnessing mining for poverty reduction, especially in Africa. *Natural Resources Forum*, 26(1), 69-73. doi:10.1111/1477-8947.00007
- Landsat Missions*. (no date). Retrieved April 18, 2017, from United States Geological Survey (USGS): <https://landsat.usgs.gov/what-are-band-designations-landsat-satellites>
- Liew, S.-C., Lu, X.-X., Chen, P., & Zhou, Y. (2003). Remote Sensing of Suspended Sediment Concentrations in Highly Turbid Inland River Waters: An Example from the Lower Jinsha Tributary, Yunnan, China. doi:<https://courses.nus.edu.sg/course/geoluxx/notes/Liew%20et%20al%20rs%20of%20SSC.pdf>
- Lin, C., Wu, C.-C., Tsogt, K., Ouyang, Y.-C., & Chang, C.-I. (2015). Effects of Atmospheric correction and pansharpening on LULC classification accuracy using WorldView-2 imagery. *Information Processing in Agriculture* 2, 2(1), 25-36. Retrieved from <http://dx.doi.org/10.1016/j.inpa.2015.01.003>
- Liu, Y., Islam, M. A., & Jay, G. (2003). Quantification of shallow water quality parameters by means of remote sensing. *Progress in Physical Geography*, 27(1), 24-43.
- Lobo, F. L., Costa, M. P., & Novo, E. M. (2015). Time-series analysis of Landsat-MSS/TM/OLI images over Amazonian waters impacted by gold mining activities. *Remote Sensing of Environment*, 157, 170-184. doi:10.1016/j.rse.2014.04.030
- Lobo, F. L., Costa, M., Novo, E. M., & Telmer, K. (2016). Distribution of Artisanal and Small-Scale Gold Mining in the Tapajos River Basin (Brazilian Amazon) over the Past 40 Years and Relationship with Water Siltation. *Remote Sensing*, 8(579). doi:doi:10.3390/rs8070579
- Lodhi, M. A., Rundquist, D. C., Han, L., & Kuzila, M. S. (1997). The potential for remote sensing of loess soils suspended in surface waters. *Journal of the American Water Resources Association*, 33(1), 111-117. doi:10.1111/j.1752-1688.1997.tb04087.x
- Lubowski, R. N., Vesterby, M., Bucholtz, S., Baez, A., & Roberts, M. J. (2006). *Major Uses of Land in the United States, 2002*. Economic Research Service, United States Department of Agriculture. Retrieved March 30, 2017, from <http://purl.umn.edu/7203>
- Luethje, F., Kranz, O., & Schoepfer, E. (2014). Geographic Object-Based Image Analysis Using Optical Satellite Imagery and GIS Data for the Detection of Mining Sites in the Democratic Republic of Congo. *Remote Sensing*, 6(7), 6636-6661. doi:10.3390/rs6076636

- Mark, D. M. (1975). Geomorphometric Parameters: A Review and Evaluation. *Geografiska Annaler. Series A, Physical Geography*, 57(3-4), 165-177. doi:10.2307/520612
- McIntyre, J., Moore, J., & Wyche, J. (2010). *Technical Report for the Didipio Gold-copper Project*. Technical Report, OceanaGold Corporation, Melbourne, Victoria.
- McIntyre, N., Bulovic, N., Cane, I., & McKenna, P. (2016). A multi-disciplinary approach to understanding the impacts of mines on traditional uses of water in Northern Mongolia. *Science of The Total Environment*, 557-558, 404-414. Retrieved from <http://doi.org.ezproxy.library.uq.edu.au/10.1016/j.scitotenv.2016.03.092>
- Mengisteab, B. S., Blesius, L., Liu, X. H., & Hennessy, L. (2015). *Classification of artisanal small-scale gold mining sites in upper Mazaruni, Guyana 1986-2011*. MS Thesis, San Francisco State University, Department of Geography & Environment, San Francisco. Retrieved from https://geog.sfsu.edu/sites/default/files/thesis/BiniamMengisteab_Thesis_FinalVersion.pdf
- Mineral Statistics*. (n.d.). Retrieved from Mines and Geosciences Bureau (MGB): <http://www.mgb.gov.ph/2015-05-13-01-44-56/2015-05-13-01-47-51#mineral-industry-statistics>
- Morel, A., & Prieur, L. (1977). Analysis of variations in ocean color 1. *Limnology and Oceanography*, 22(4), 709-722. doi:10.4319/lo.1977.22.4.0709
- Moses, W. J., Gitelson, A. A., Perk, R. L., Gurlin, D., Rundquist, D. C., Leavitt, B. C., . . . Brakhage, P. (2012). Estimation of chlorophyll-a concentration in turbid productive waters using airborne hyperspectral data. *Water Research*, 46(4), 993-1004. doi:<https://doi.org/10.1016/j.watres.2011.11.068>
- Mountrakis, Giorgos, Im, J., & Ogole, C. (2011). Support vector machines in remote sensing: A review. *66(3)*, 247-259. Retrieved from <https://doi.org/10.1016/j.isprsjprs.2010.11.001>
- Myint, S. W., Gober, P., Brazel, A., Grossman-Clarke, S., & Weng, Q. (2011). Per-pixel vs. object-based classification of urban land cover extraction using high spatial resolution imagery. *Remote Sensing of Environment*, 115, 1145-1161.
- NASA OceanColor. (no date). Retrieved from Inherent Optical Properties (IOP): <https://oceancolor.gsfc.nasa.gov/atbd/giop/>
- Navalgund, R. (2002, January). Remote Sensing: 2. Sensors and Platforms. *Resonance*, 7(1), 37-46. doi:DOI: 10.1007/BF02836169
- Navalgund, R. R. (2001). Remote Sensing: 1. Basics and Applications. *Resonance*, 6(12), 51-60. doi:10.1007/BF02913767
- Newcastle University. (no date). *Radiometric correction of satellite images: when and why radiometric correction is necessary*. Retrieved March 7, 2017, from Newcastle University, United Kingdom: <http://www.ncl.ac.uk/tcmweb/bilko/module7/lesson3.pdf>
- Oh, H.-J., & Lee, S. (2011). Landslide susceptibility mapping on Panaon Island, Philippines using a geographic information system. *Environmental Earth Science*, 935-951. doi:10.1007/s12665-010-0579-2
- Oldeland, J., Dorigo, W., Lieckfeld, L., Lucieer, A., & Jurgens, N. (2010). Combining vegetation indices, constrained ordination and fuzzy classification for mapping semi-natural vegetation

- units for hyperspectral imagery. *Remote sensing of Environment*, 114, 1155-1166. doi:10.1016/j.rse.2010.01.003
- Olofsson, P., Foody, G. M., Stehman, S. V., & Woodcock, C. E. (2013). Making better use of accuracy data in land change studies: Estimate accuracy and area and quantifying uncertainty using stratified estimation. *Remote Sensing of Environment*, 122-131. doi:<http://dx.doi.org/10.1016/j.rse.2012.10.031>
- Oommen, T., Misra, D., Twarakavi, N., Prakash, A., Sahoo, B., & Bandopadhyay, S. (2008). An Objective Analysis of Support Vector Machine Based Classification for Remote Sensing. *Mathematical Geosciences*, 40, 409-424. doi:10.1007/s11004-008-9156-6
- Oxford Business Group. (2016). *Efforts to bring small-scale mining in the Philippines back into the formal sector are under way*. Progress Report. Retrieved April 5, 2017, from Oxford Business Group: <https://www.oxfordbusinessgroup.com/analysis/book-efforts-bring-small-scale-mining-back-formal-sector-are-under-way>
- Parker, D. C., & Wolff, M. F. (1965). Remote Sensing. *International Science and Technology*, 43, 20-31.
- People Small-scale Mining Act*. (1991). Retrieved September 7, 2016, from Mines and Geosciences Bureau (MGB): <http://www.mgb.gov.ph/Files/Policies/RA%207076.pdf>
- Perez-Pena, J. V., Azanon, J. M., Booth-Rea, G., Azor, A., & Delgado, J. (2009). Differentiating geology and tectonics using a spatial autocorrelation technique for the hypsometric integral. *Journal of Geophysical Research*, 114, 1-15. doi:10.1029/2008JF001092
- Philippine Institute for Development Studies. (2005, July). Basics on Philippine climatology. *Economic Issue of the Day*, V(2). Retrieved from Economic Issue of the Day: <http://dirp4.pids.gov.ph/ris/eid/pidsei0502.pdf>
- (2009). *Philippines National Demographic and Health Survey 2008*. Calverton, Maryland: National Statistics Office and ICF Macro. Retrieved April 18, 2017, from The Demographic and Health Surveys: <https://dhsprogram.com/pubs/pdf/FR224/FR224.pdf>
- Pike, R. J., & Wilson, S. E. (1971). Elevation-relief ratio, hypsometric integral, and geomorphic area-altitude analysis. *Bulletin of the Geological Society of America*, 82(4), 1079-1084. doi:10.1130/0016-7606(1971)82[1079:ERHIAG]2.0.CO;2
- Platt, R. V., & Rapoza, L. (2008). An Evaluation of an Object-Oriented Paradigm for Land Use/Land Cover Classification. *The Professional Geographer*, 60(1), 87-100. doi:10.1080/00330120701724152
- Postelniak, A. (2014). Geometric potential of Pleiade-1A satellite imagery. *De Gruyter*, LX(3), 19-27. doi:0.2478/gse-2014-0014
- Price, J. C. (1987, February). Calibration of Satellite Radiometers and the Comparison of Vegetation Indices. *Remote Sensing of Environment*, 21, 15-27. doi:[http://dx.doi.org/10.1016/0034-4257\(87\)90003-4](http://dx.doi.org/10.1016/0034-4257(87)90003-4)
- Principle, J. A. (2012). Exploring climate change effects on watershed sediment yield and land cover-based mitigation measures using SWAT model, RS and GIS: Case of Cagayan River Basin, Philippines. *International Archives of the Photogrammetry, Remote Sensing and Spatial Information Sciences*, XXXIX-B8, 193-198. Retrieved April 18, 2017, from <http://www.int>

arch-photogramm-remote-sens-spatial-inf-sci.net/XXXIX-B8/193/2012/isprsarchives-XXXIX-B8-193-2012.pdf

Radiometric resolution. (2016, May 11). Retrieved from Natural Resources Canada: <http://www.nrcan.gc.ca/node/9379>

Rao, D. P. (2000). Role of Remote Sensing and Geographic Information System in Sustainable Development. *International Archives of Photogrammetry and Remote Sensing, XXXIII*, 1231-1251. Retrieved from http://www.isprs.org/proceedings/XXXIII/congress/part7/1231_XXXIII-part7.pdf

Rawat, J. S., & Kumar, M. (2015). Monitoring land use/cover change using remote sensing and GIS techniques: A case study of Hawalbagh block, district Almora, Uttarakhand, India. *The Egyptian Journal of Remote Sensing and Space Sciences, 18*, 77-84. Retrieved from <http://dx.doi.org/10.1016/j.ejrs.2015.02.002>

Richards, J. A. (2013). *Remote Sensing Digital Image Analysis (Fifth Edition)*. New York: Springer-Verlag Berlin Heidelberg.

Ritchie, J. C., Cooper, C. M., & Yongqing, J. (1987). Using Landsat Multispectral Scanner Data to Estimate Suspended Sediments in Moon Lake, Mississippi. *Remote sensing of Environment, 23*, 65-81.

Robert, E., Grippa, M., Kergoat, L., Pinet, S., Gal, L., Cochonneau, G., & Martinez, J.-M. (2016). Monitoring water turbidity and surface suspended sediment concentration of the Bagre Reservoir (Burkina Faso) using MODIS and field reflectance data. *International Journal of Applied Earth Observation and geoinformation, 52*, 243-251.

Robinson, D. J., Redding, N. J., & J, C. D. (2002). *Implementation of a Fast Algorithm for Segmenting SAR Imagery*. Defense Science and Technology Organization. DSTO Electronics and Surveillance Research Laboratory.

Rugner, H., Schwientek, M., Beckingham, B., Kuch, B., & Grathwohl, P. (2013, February 17). Turbidity as a proxy for total suspended solids (TSS) and particle facilitated pollutant transport in catchments. *Environmental Earth Science, 373-380*. doi:DOI 10.1007/s12665-013-2307-1

Russian Global Lab Project. (2008). *Water Carries: Suspensions and Turbidity*. Retrieved from Global Lab Studies: https://staff.concord.org/~btinker/GL/web/water/suspensions_turbidity.html

Ryan, T. P. (2007). Simple Linear Regression, Correlation, and Calibration. In T. P. Ryan, *Modern Engineering Statistics* (pp. 232-275). Hoboken, New Jersey, United States of America: John Wiley & Sons, Inc.

Satapathy, D. R., Vijay, R., Kamble, S. R., & Sohony, R. A. (2010). Remote Sensing of Turbidity and Phosphate in Creeks and Coast of Mumbai: An Effect of Organic Matter. *Transactions in GIS, 14(6)*, 811-832.

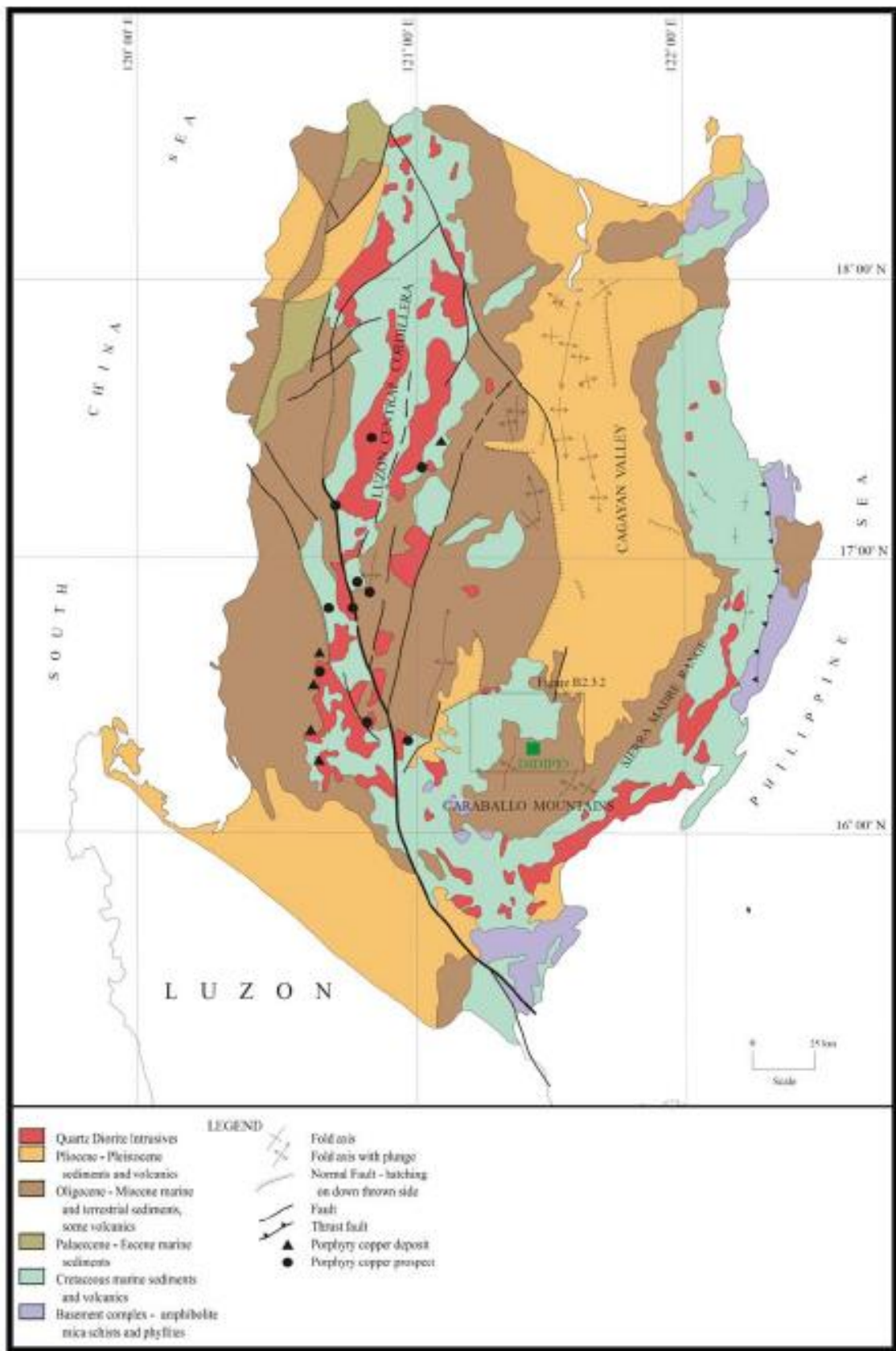
Schmugge, T. J., Kustas, W. P., Ritchie, J. C., Jackson, T. J., & Rango, A. (2002). Remote Sensing in hydrology. *Advances in Water Resources, 25*, 1367-1385.

- Shahzad, F., & Gloaguen, R. (2011). TecDEM: A MATLAB based toolbox for tectonic geomorphology, Part 2: Surface dynamics. *and basin analysis*, 37(2), 261-271. doi:10.1016/j.cageo.2010.06.009
- Shrestha, S., & Kazama, F. (2007). Assessment of surface water quality using multivariate statistical techniques: A case study of the Fuji river basin, Japan. *Environmental Modelling & Software*, 464-475. Retrieved from <http://doi.org/10.1016/j.envsoft.2006.02.001>
- Singh, A. K. (2016). *Applicability of Nighttime Remote Sensing Data to Analyse Urban Dynamics: The Indian Scenario*. Raleigh, North Carolina, United States: Lulu Publication. Retrieved from https://books.google.com.au/books?id=JTbuDQAAQBAJ&pg=PA36&lpg=PA36&dq=remote+sensing+was+associated+in+securing+analog+black+and+white+aerial+photographs&source=bl&ots=QphJf8twoK&sig=xuNLC_37Izj_Zdi7H79zcetYWfA&hl=en&sa=X&ved=0ahUKEwiP2cmYl_vSAhXLgFQKHb_2
- Smith, S. A. (1989). Sedimentation in a meandering gravel-bed river: the River Tywi, South Wales. *Geological Journal*, 24, 193-204. doi:0072-1OSO/89/030193-125
- Sosiak, A. (2001). *Predictive equations for suspended solids and dissolved oxygen in the highwood river*. Environment. Retrieved from <https://open.alberta.ca/publications/0778519031>
- Sousa, R. N., Veiga, M. M., Meech, J., Jokinen, J., & Sousa, A. J. (2011). A simplified matrix of environmental impacts to support an intervention program in a small-scale mining site. *Journal of Cleaner Production*, 19, 580-587.
- Stone, D., Palmer, D., Hamilton, B., Cooney, C., & Mosley, L. (2016). *Coorong, Lower Lakes and Murray Mouth water quality monitoring program 2009-2016*. Australian Government, Department of Environment, Water and Natural Resources. Retrieved April 6, 2017, from http://www.epa.sa.gov.au/data_and_publications/water_quality_monitoring
- Story, M., & Congalton, R. G. (1986). Accuracy Assessment: A User's Perspective. *Photogrammetric Engineering and Remote Sensing*, 52, 397-399.
- Strahler, A. N. (1952). Hypsometric (Area-Latitude) Analysis of Erosional Topography. *Geological Society of America Bulletin*, 63, 1117-1142. doi:10.1130/0016-7606(1952)63[1117:HAAOET]2.0.CO;2
- Stumpf, R. P., & Pennock, J. R. (1991). Remote Estimation of the Diffuse Attenuation Coefficient in a Moderately Turbid Estuary. *Remote Sensing of Environment*, 38, 183-191. doi:[https://doi.org/10.1016/0034-4257\(91\)90088-N](https://doi.org/10.1016/0034-4257(91)90088-N)
- Sun, L., & Schulz, K. (2015). The Improvement of Land Cover Classification by Thermal Remtoe Sensing. *Remote Sensing*, 7(7), 8368-8390. doi:10.3390/rs70708368
- Sun, W., Chen, B., & Messinger, D. W. (2014). Nearest-neighbor diffusion-based pan-sharpening algorithm for spectral images. *Optical Engineering*, 53(1), 1-11. doi:10.1117/1.OE.53.1.013107
- Syahreza, S., MatJafri, M. Z., Lim, H. S., & Mustapha, M. R. (2012). Water Quality Assessment in Kelantan Delta using Remote Sensing Technique. *Electro-Optical Remote Sensing, Photonic Technologies, and Applications VI*, 85420X. doi:10.1117/12.978931

- Taati, A., Sarmadian, F., Mousavi, A., Pour, C. T., & Shahir, A. H. (2014). Land Use Classification using Support Vector Machine and Maximum Likelihood Algorithms. *Walailak Journal of Science and Technology*, 12(8), 681-687. doi:10.14456/WJST.2015.33
- Tamene, L., Park, S. J., Dikau, R., & Vlek, P. L. (2006). Analysis of factors determining sediment yield variability in the highlands of northern Ethiopia. *Geomorphology*, 76-91. Retrieved May 2, 2017, from <https://www.geographie.uni-bonn.de/research/research-group-prof.-dikau/pdfs/Tamene%20et%20al.%202006.pdf>
- Telmer, K., & Stapper, D. (2007). *Evaluating and Monitoring Small Scale Gold Mining and Mercury Use: Building a Knowledge-base with Satellite Imagery and Field Work*. Terminal Report, University of Victoria, Canada, School of Earth and Ocean Sciences, Aqueous Geochemistry Laboratory. Retrieved from <http://www.ais.unwater.org/ais/aiscm/getprojectdoc.php?docid=405>
- The USGS Water Science School. (2016). Retrieved March 3, 2017, from United States Geological Survey (USGS): <https://water.usgs.gov/edu/runoff.html>
- Tindall, J. A., & Kunkel, J. R. (2009). Physical Properties and Characteristics of Soils. In J. A. Tindall, & J. R. Kunkel, *Unsaturated Zone Hydrology*. Prentice Hall.
- Ting, K. M. (2010). Confusion Matrix. In K. M. Ting, *Encyclopedia of Machine Learning* (p. 209). doi:10.1007/978-0-387-30164-8_157
- Tzotsos, A., & Argialas, D. (2008). Support Vector Machine classification for Object-Based Image Analysis. In T. Blaschke, S. Lang, & G. J. Hay, *Object-Based Image Analysis* (pp. 663-677). Heidelberg: Springer Berlin . doi:10.1007/978-3-540-77058-9
- United Nations. (1996). Recent developments in small-scale mining. Natural Resources Forum. A *United Nations Sustainable Development Journal*, 20(3), 215-225. doi:10.1111/j.1477-8947.1996.tb00655.x
- Vapnik, V. (1998). *Statistical Learning Theory*; New York, USA: Wiley.
- Vega, M., Pardo, R., Barrado, E., & Deban, L. (1998, March). Assessment of seasonal and polluting effects on the quality of river water by exploratory data analysis. *Water Reserve*, 32(12), 3581-3592. doi:10.1016/S0043-1354(98)00138-9
- Verstraeten, G., & Poesen, J. (2001). Factors controlling sediment yield from small intensively cultivated catchments in a temperate humid climate. *Geomorphology*, 40(1-2), 123-144.
- Vibhute, A. D., Kale, K. V., Dhumal, R. K., & Mehrotra, S. C. (2016). Hyperspectral imaging data atmospheric correction challenges and solutions using QUAC and FLAASH algorithms. *2015 International Conference on Man and Machine Interfacing (MAMI)*. IEEE. doi:10.1109/MAMI.2015.7456604
- Wang, C., Pavlowsky, R. T., Huang, Q., & Chang, C. (2016). Channel bar feature extraction for a mining-contaminated river using high-spatial multispectral remote-sensing imagery. *GIScience & Remote Sensing*, 53(3), 283-302. doi:10.1080/15481603.2016.1148229
- Wang, J. J., & Lu, X. X. (2010). Estimation of suspended sediment concentrations using Terra MODIS: An example from the lower Yangtze River, China. *Science of the Total Environment*, 408, 1131-1138. doi:<https://doi.org/10.1016/j.scitotenv.2009.11.057>

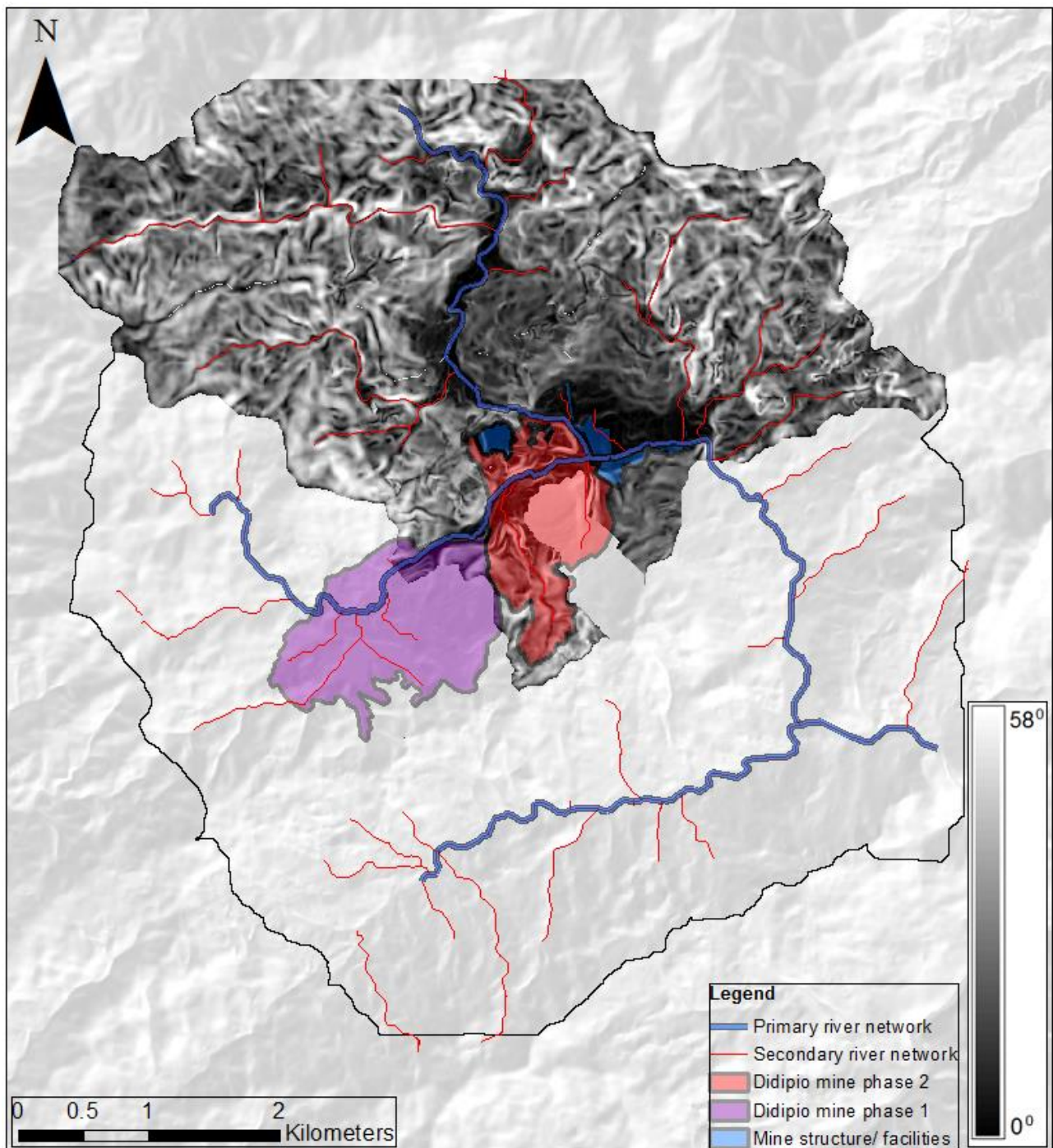
- Wang, J.-J., Lu, X.-X., Zhou, Y., & Liew, S.-C. (2012). Suspended sediment concentrations estimate in highly turbid rivers: a field spectral survey. *Remote Sensing Letters*, 409-417. doi:<http://dx.doi.org/10.1080/2150704X.2012.743689>
- Warner, T. A., & Nerry, F. (2009). Does single broadband or multispectral thermal data add information for classification of visible, near- and shortwave infrared imagery of urban areas? *International Journal of Remote Sensing*, 2155-2171. doi:10.1080/01431160802549286
- Wen, G., Marshak, A., & Cahalan, R. F. (2006). Impact of 3-D Clouds on Clear-Sky Reflectance and Aerosol Retrieval in a Biomass Burning Region of Brazil. *IEEE Geoscience and remote sensing letters*, 3(1), 169-172.
- Wu, J. (2008). Land Use Changes: Economic, Social, and Environmental Impacts. *Choices: The magazine of food, farm, and resource issues*, 23(4), pp. 6-10. Retrieved from <http://www.farmdoc.illinois.edu/policy/choices/20084/theme1/2008-4-02.pdf>
- Wu, J.-L., Ho, C.-R., Huang, C.-C., Srivastav, A. L., Tzeng, J.-H., & Lin, Y.-T. (2014, November 28). Hyperspectral Sensing for Turbid Water Quality Monitoring in Freshwater Rivers: Empirical Relationship between Reflectance and Turbidity and Total Solids. *Sensors*, 14, 22670-22688. doi:10.3390/s141222670
- Xiaoying, J. (2009). Segmentation-based image processing system. Retrieved from <https://www.google.com/patents/US20090123070#backward-citations>
- Yengoh, G. T., Dent, D., Olsson, L., Tengberg, A. E., & Tucker III, C. J. (2016). Use of the Normalized Difference Vegetation Index (NDVI) to Assess Land Degradation at Multiple Scales. In *Springer Briefs in Environmental Science* (pp. 1-81). New York. doi:10.1007/978-3-319-24112-8
- Yong, R. N., Nakano, M., & Pusch, R. (2012). Origin and Function of Soils. In R. N. Yong, M. Nakano, & R. Pusch, *Environmental Soil Properties and Behaviour* (pp. 1-24). Boca Raton: Taylor & Francis Group.
- Yousefi, S., Mirzaee, S., Tazeh, M., Pourghasemi, H., & H, K. (2015). Comparison of different algorithms for land use mapping in dry climate using satellite images: a case study of the Central regions of Iran. *Desert*, 20(1), 1-10. Retrieved from https://jdesert.ut.ac.ir/article_54077_a03ba2904e5acfaea28503c6a535198d.pdf
- Yuill, B. T., Gaweesh, A., Allison, M. A., & Meselhe, E. A. (2015). Morphodynamic evolution of a lower Mississippi River channel bar after sand mining. *Earth Surface Processes and Landforms*, 41(4), 526-542. doi:10.1002/esp.3846
- Zhang, H. K., & Roy, D. P. (2016). Computationally Inexpensive Landsat 8 Operational Land Imgaer (OLI) Pansharpening. *Remote sensing*, 8(3), 190. doi:10.3390/rs8030180
- Zhang, Y., Pulliainen, J. T., Koponen, S. S., & Hallikainen, M. T. (2003). Water Quality Retrievals from combined Landsat TM Data and ERS-2 SAR Data in the Gulf of Finland. *Transactions on Geoscience and Remote sensing*, 41(3), 622-629. doi:10.1109/TGRS.2003.808906
- Zinnert, C, J., Shiflett, S. A., Via, S., Bissett, S., Dows, B., . . . Young, D. R. (2016). Spatial-Temporal Dynamics in Barrier Island Upland Vegetation: The Overlooked Coastal Landscape. *Ecosystems*, 19, 685-697. doi:10.1007/s10021-016-9961-6

Appendix A - Regional geology of Northern Luzon

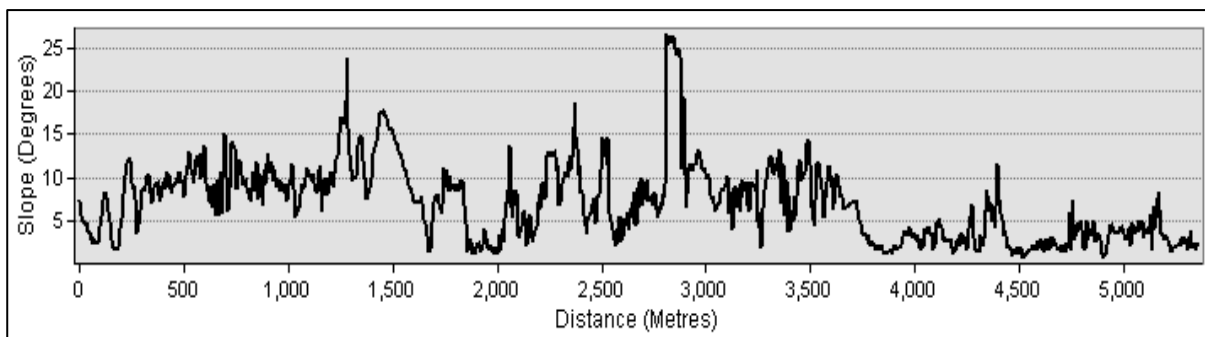
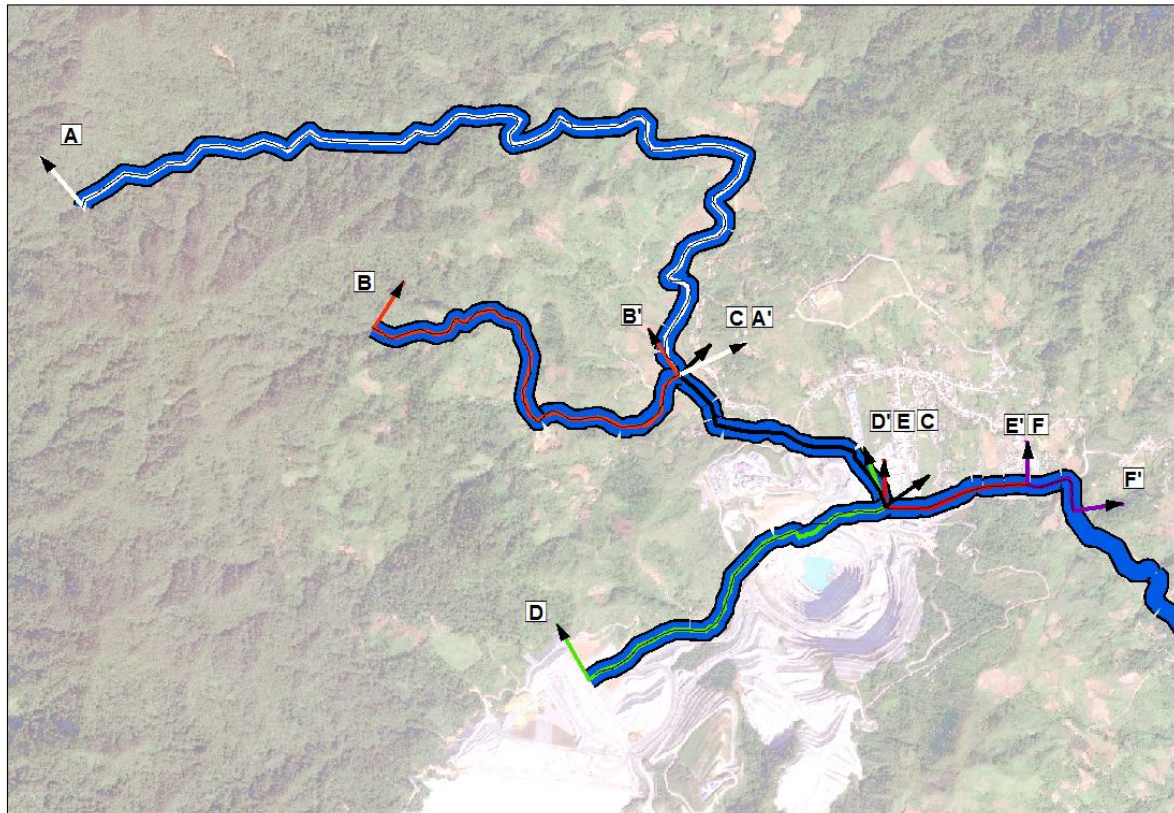


Adapted from *Technical Report for the Didipio Gold-copper Project* (p. 30), by J. McIntyre, J. Moore and J. Wyche, 2010.

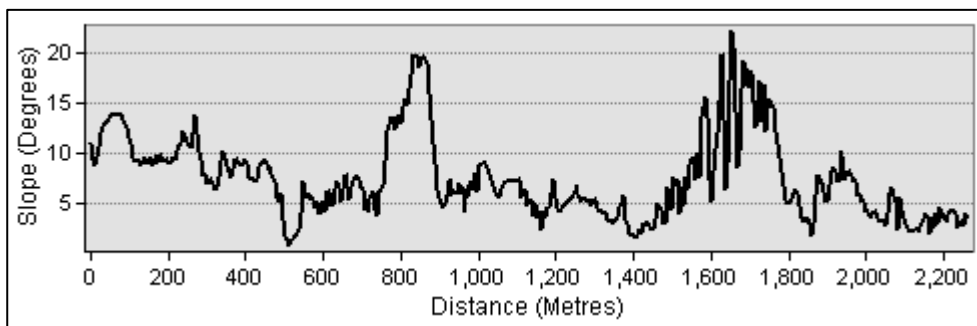
Appendix B - Slope map of selected sub-drainage basins of Didipio catchment



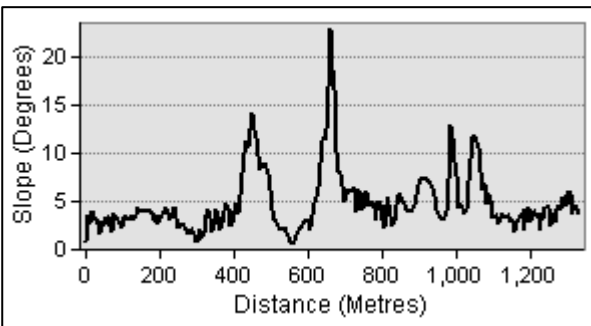
Appendix C - Channel slopes



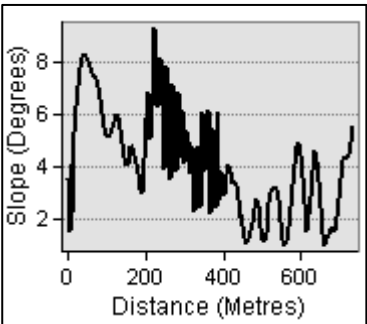
Surong River



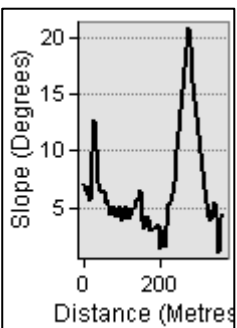
Camgat River



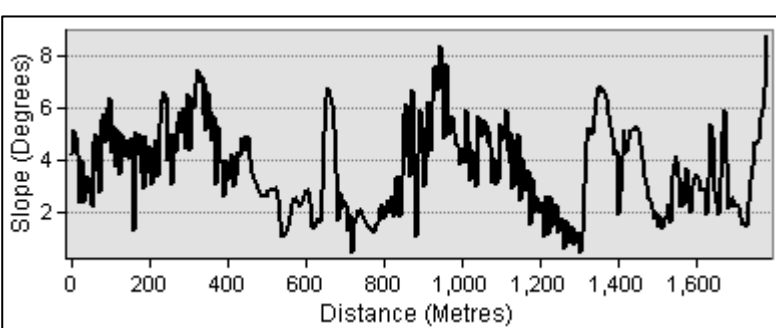
Camgat-Surong River



Didipio River



Dupit River



Dinauyan River

Appendix D - Photographs of artisanal and small-scale mining practices in Didipio catchment

SITE NO. 1	SITE NO. 2
Lat: 16.335047 ⁰ Long: 121.446426 ⁰	Lat: 16.333311 ⁰ Long: 121.440083 ⁰
	
Some small-scale miners along Camgat-Surong River were spotted while using highly pressurised water to disintegrate ground sediments. These sediments had been transferred using wheelbarrow, and packed into sacks.	A completely stripped side of a mountain is the largest small-scale mine that can be found in Didipio.
SITE NO. 3	SITE NO. 4
Lat: 16.325780 ⁰ Long: 121.447276 ⁰	Lat: 16.333806 ⁰ Long: 121.444716 ⁰
	
Hydraulic pipes were also observed in a small-scale mine north of the Dinauyan River.	A suspected stockpile of sacks that contain ore sediments was found beside site no.1.

SITE NO. 5	SITE NO. 6
Lat: 16.333439 ⁰ Long: 121.448081 ⁰	Lat: 16.331124 ⁰ Long: 121.455231 ⁰
 11.28.2015 10:19	 11.28.2015 10:46
The traditional panning with the assistance of excavator for higher production yield	An inactive ASM tunnel at the north of Mine phase 2

SITE NO. 7
Lat: 16.334247 ⁰ Long: 121.453869 ⁰
 11.28.2015 11:34
A small-scale mine that is situated along the boundary between the local community and the OceanaGold's campsite.

Appendix E - Parameters for radiometric calibration

Product ID	Band	Gain	Bias	ESUN	Sun Elevation	Earth-Sun Distance
		W·m ⁻² ·sr ⁻¹ ·μm	W·m ⁻² ·sr ⁻¹ ·μm	W·m ⁻² ·sr ⁻¹ ·μm	degrees	degrees
20130320 Pleiades-1A	1 Blue	9.22	0	1915	65.01452400	0.9953689068
	2 Green	9.40	0	1830		
	3 Red	10.36	0	1594		
	4 Near Infrared	15.63	0	1060		
	5 PAN	11.74	0	1548		
20140505 Pleiades-1A Swathe 1- WEST	1 Blue	9.15	0	1915	71.74992600	1.0081716820
	2 Green	9.30	0	1830		
	3 Red	10.34	0	1594		
	4 Near Infrared	15.61	0	1060		
	5 PAN	11.65	0	1548		
20140505 Pleiades-1A Swathe 2- EAST	1 Blue	9.15	0	1915	71.80360379	1.008171682
	2 Green	9.30	0	1830		
	3 Red	10.34	0	1594		
	4 Near Infrared	15.61	0	1060		
	5 PAN	11.65	0	1548		
20160106 SPOT-6	1 Blue	8.01	0	1983	42.7707610000	0.9832898942
	2 Green	9.35	0	1826		
	3 Red	10.34	0	1540		
	4 Near Infrared	13.88	0	1095		
	5 PAN	10.32	0	1707		

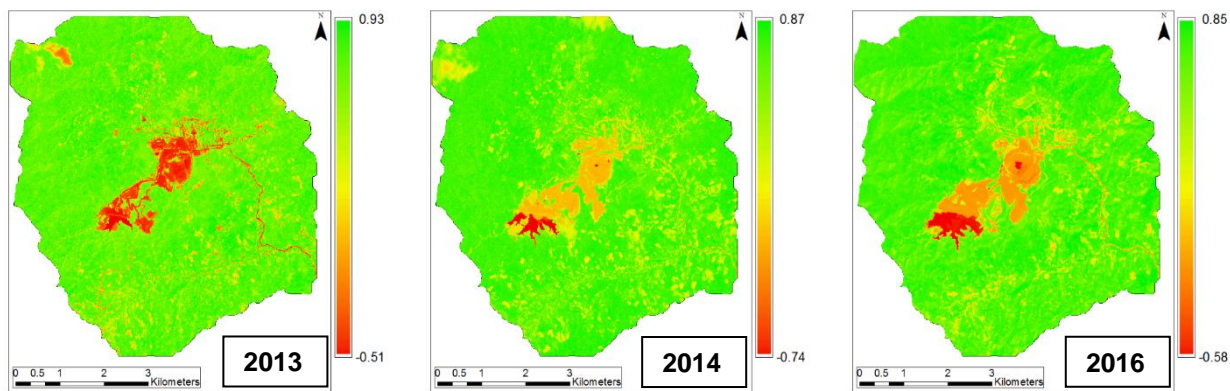
Pleiades: © CNES (2013, 2014), Distribution Airbus DS / Spot Image; SPOT: © AIRBUS DS (2016)

Appendix F- Parameters and attributes for segmentation

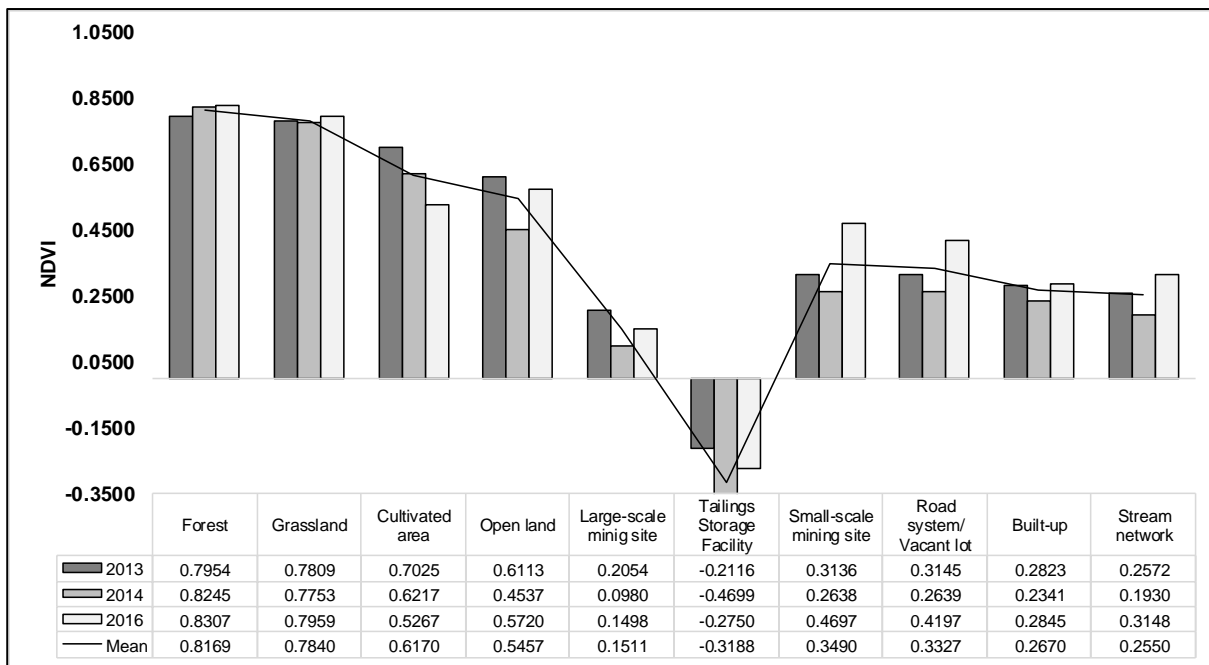
Settings	Algorithm	Years		
		2013	2014	2016
Segment size	Edge	15	10	10
Merge size	Full Lambda Schedule	95	93	97
Kernel size		19	19	19

Feature	Attribute	Description
Spectral	Spectral_Mean	Mean value of pixels per spectral band
	Spectral_Max	Maximum value of pixels per spectral band
	Spectral_Min	Minimum value of pixels per spectral band
	Spectral_STD	Standard deviation value of pixels per spectral band
Spatial	Compactness	It is defined by the equation: $\text{Sqrt} (4 * \text{Area}/\pi)/\text{outer contour length}$
	Roundness	It is defined by the equation: $4 * (\text{Area}) / (\pi * \text{Major_Length}^2)$
	Form factor	Circle = 1 Square = $\pi/4$
	Rectangular fit	This attribute measures the closeness of an object to rectangle. A rectangle has a value of 1 while a non-rectangular object is less than 1.
	Main direction	90 degrees represents North and South while 0 and 180 degrees are west and east respectively
Texture	Texture-Range	Average range of pixels inside the kernel
	Texture-Mean	Mean value of pixels inside the kernel
	Texture-Variance	Average variance of pixels inside the kernel

Appendix G- NDVI maps



Generated NDVI maps used as ancillary data in the classification of land use features
 (a) Pleiades-1A 20 March 2013; (b) Pleiades-1A 05 May 2014; (c) SPOT-6 06 January 2016



Normalised difference vegetation index (NDVI) of training data from the images in 2014, 2015 and 2016
 (a) Pleiades-1A 20 March 2013; (b) Pleiades-1A 05 May 2014; (c) SPOT-6 06 January 2016